



TECHNISCHE UNIVERSITÄT MÜNCHEN

Lehrstuhl für Theoretische Chemie

First-Principles Statistical Mechanics Study of  
Functionalization of Doped Silicon Clusters:  
from Simple Building Blocks to Functionalized Materials

Dennis Palagin

Vollständiger Abdruck der von der Fakultät für Chemie der Technischen Universität München zur Erlangung der akademischen Grades eines

Doktors der Naturwissenschaften

genehmigten Dissertation.

Vorsitzender: Univ.-Prof. Dr. Mathias Nest

Prüfer der Dissertation:

1. Univ.-Prof. Dr. Karsten Reuter
2. Univ.-Prof. Dr. Ulrich Heiz

Die Dissertation wurde am 11.07.2013 bei der Technischen Universität München eingereicht und durch die Fakultät für Chemie am 07.10.2013 angenommen.

Diese Arbeit wurde in der Zeit von August 2010 bis Juli 2013 unter der Aufsicht von Prof. Dr. Karsten Reuter am Lehrstuhl für Theoretische Chemie der Technischen Universität München durchgeführt.

Erster Gutachter (Betreuer): Univ.-Prof. Dr. Karsten Reuter

Zweiter Gutachter: Univ.-Prof. Dr. Ulrich Heiz

Prüfungstermin: 25.10.2013

## Abstract

Assembly at the molecular level is one of the most fundamental approaches in chemistry for obtaining new materials with desired novel properties, for instance relevant for the growing area of molecular electronics. For such nano-assembly, the use of endohedrally doped clusters as building blocks proved to be fruitful due to their suitable cage-like geometries, high stability and easily tunable electronic and optical properties. The prevalence of silicon in the semiconductor industry has sparked great interest in such silicon-based nanostructures that could act as building blocks for new easy-to-integrate and engineered materials.

The present thesis systematically assesses the feasibility of using endohedrally doped silicon clusters to design novel cluster-assembled materials using state-of-the-art first-principles statistical mechanics methodology. Starting with a rigorous analysis of the nature of chemical bonding within endohedrally doped  $MSi_{16}^+$  ( $M = \text{Ti, V, Cr}$ ) clusters, the diminished role of shell closure for the structure stabilization is traced back to the adaptive capability of the metal-Si bonding, which is more the result of a complex hybridization than the originally proposed mere formal charge transfer. The resulting strong interaction with the encapsulated dopant atom unfortunately goes hand in hand with a quenching of the dopant spin moment. This drawback is suggested to be overcome by saturation of the  $sp^3$ -caused Si dangling bonds, for example through hydrogen termination. Density functional theory based global geometry optimization finds the smallest  $Si_{16}H_{16}$  endohedral cage generally too small to encapsulate  $3d$  metal dopant atoms. For the next larger fullerene-like cage, however, perfectly symmetric  $MSi_{20}H_{20}$  ( $M = \text{Co, Ti, V, and Cr}$ ) cage structures are identified as ground states. These structures conserve the high spin moment of the dopant atom and therewith underscore the potential of this Si nanoform for novel cluster-based materials with unique magnetic properties.

Intriguingly, reducing the degree of hydrogenation may be used to control the number of reactive sites to which other cages can be attached, while still preserving the structural integrity of the building block itself. For the prototypical  $CrSi_{20}H_{20}$  cluster, this leads to a toolbox of  $CrSi_{20}H_{20-2n}$  monomers with different number of double “docking sites”, that allows building network architectures of any morphology. For  $(CrSi_{20}H_{18})_2$  dimer and  $[CrSi_{20}H_{16}](CrSi_{20}H_{18})_2$  trimer structures we illustrate that such aggregates conserve the high spin moments of the dopant atoms and are therefore most attractive candidates for cluster-assembled magnetic materials. The study suggests that the structural completion of the individual endohedral cages within the doubly bridge bonded structures and the high thermodynamic stability of the obtained aggregates are crucial for potential synthetic polymerization routes *via* controlled dehydrogenation.

Adding several different dopant atoms to each building block opens another configurational dimension and can yield unique properties unavailable for singly-doped clusters, such as large dipole or magnetic moments. While  $M_2\text{Si}_{18}$  has been experimentally identified as smallest Si structure capable of encapsulating transition metal dimers, we find that even at the minimized dopant-cage interaction of hydrogenated  $M_2\text{Si}_{18}\text{H}_{12}$  the spin moments of the appealing  $\text{Cr}_2^+$ ,  $\text{Mn}_2^+$  and  $\text{CrMn}^+$  magnetic dimers are completely quenched. This is again much different when going towards larger hydrogenated Si cages ( $\text{Si}_{24}\text{H}_{24}$ ,  $\text{Si}_{28}\text{H}_{28}$ ). Here, the identified ground state structures indeed correspond to multi-doped endohedral cages with magnetic moments that go beyond the single-atom dopant  $4s^13d^5$  septet limit.

As an extensive outlook, the problem of moving from the study of isolated individual Si clusters towards the properties of such clusters in a non-trivial environment, *i.e.* under the influence of other bonding partners, such as extended surfaces, is introduced for the example of mixed Si/Sb clusters formed on Si(111)-(7×7) surface. The concomitant necessity of extending the configurational sampling to a grand-canonical ensemble within the *ab initio* thermodynamics framework in order to overcome the limitations of the classical global optimization formulation is critically discussed in the last chapter.

## Zusammenfassung

Konstruktion auf molekularem Niveau ist einer der grundlegenden Ansätze in der Chemie zur Erzeugung neuer Materialien mit speziellen Eigenschaften. Molekulare Elektronik bietet einen eindrucksvollen, neuen Anwendungsbereich für solche Materialien. Die Verwendung von dotierten Clustern als Bausteine für solche molekularen Konstrukte hat sich, aufgrund ihrer käfigartigen Geometrie, hohen Stabilität und ihrer leicht abstimmbaren, elektronischen und optischen Eigenschaften, als fruchtbarer Ansatz bewiesen. Von besonderem Interesse sind Silizium-basierte Nanostrukturen, weil Silizium häufige Anwendung in der Halbleiterindustrie findet und solche Materialien einfach zu integrierende und abstimmbare Bausteine bilden könnten.

In dieser Arbeit wurde mit Hilfe moderner *ab initio* statistisch mechanischer Verfahren systematisch die Anwendbarkeit endohedral dotierter Siliziumcluster für die Konstruktion neuer Cluster-basierter Materialien studiert. Beginnend mit der gründlichen Analyse der Natur der chemischen Bindung innerhalb endohedral dotierter  $MSi_{16}^+$  ( $M = \text{Ti, V, Cr}$ ) Cluster, wird ein abgeschwächter Einfluss des Schalenabschlusses beobachtet und auf die adaptive Fähigkeit der Metall-Silizium Bindung zurückgeführt. Dieses liegt stärker an komplexer Bindungshybridisierung als, wie anfangs postuliert, an formalem Ladungstransfer. Die daraus resultierende starke Wechselwirkung des Siliziumgerüsts mit dem eingeschlossenen Dotierungsatom resultiert jedoch in einer Reduktion des Spinmoments. Dieser Effekt kann durch Wasserstoffabsättigung freier  $sp^3$ -Bindungsstellen an den Siliziumatomen rückgängig gemacht werden. Mittels Dichtefunktionaltheorie-basierter globaler Geometrieoptimierung zeigt sich, dass  $Si_{16}H_{16}$  Käfige zu klein sind, um  $3d$  Metallatome einzukapseln. Jedoch finden sich perfekt symmetrische fullerenartige Käfigstrukturen als Grundzustand der nächstgrößeren  $MSi_{20}H_{20}$  ( $M = \text{Co, Ti, V, and Cr}$ ) Cluster. Diese Strukturen erhalten das hohe Spinmoment des Dotierungsatoms und bezeugen damit das Potenzial dieser Siliziumnanostrukturen als Bausteine neuartiger Cluster-basierter Materialien mit einzigartigen magnetischen Eigenschaften.

Interessanterweise kann man den Grad der Hydrogenierung verwenden, um die Anzahl der Reaktionszentren für die Anknüpfung anderer Cluster zu kontrollieren, ohne die strukturelle Integrität des individuellen Bausteins zu zerstören. Dadurch ergibt sich ausgehend von prototypischen  $CrSi_{20}H_{20}$  Clustern eine Vielzahl möglicher  $CrSi_{20}H_{20-2n}$  Monomere mit unterschiedlicher Anzahl doppelter Andockstellen als Bausteine molekularer Netzwerkarchitekturen mit beliebiger Morphologie. Für  $(CrSi_{20}H_{18})_2$  Dimer- und  $[CrSi_{20}H_{16}](CrSi_{20}H_{18})_2$  Trimerstrukturen zeigen wir, dass solche Aggregate das hohe Spinmoment der Dotierungsatome erhalten und daher attraktive Kandidaten für magnetisch Cluster-basierte Materialien sind. Aus dieser Arbeit ergibt sich, dass der strukturelle

Abschluss individueller, symmetrischer Cluster durch die doppelte Si-Si Bindung, sowie die hohe thermodynamische Stabilität der so erhaltenen Aggregate entscheidende Faktoren für eine mögliche synthetische Polymerisation über kontrollierte Dehydrogenierung darstellen.

Das Hinzufügen mehrerer verschiedener Dotierungsatome zu jedem Baustein öffnet eine weitere Konfigurationsdimension und bringt zusätzliche, einzigartige Eigenschaften, die einzeln gedopten Clustern nicht zugänglich sind, wie zum Beispiel vergrößerte Dipol- und magnetische Momente. Experimentell wurde  $M_2Si_{18}$  als kleinste Siliziumstruktur identifiziert, die Übergangsmetalldimere umhüllen kann. Wir finden jedoch, dass in solchen Strukturen die Spinmomente von  $Cr_2^+$ ,  $Mn_2^+$  und  $CrMn^+$  Dimeren komplett gelöscht werden. Das ist ganz anders bei größeren hydrogenierten Clustern, wie z.B.  $Si_{24}H_{24}$  und  $Si_{28}H_{28}$ . Hier entsprechen die identifizierten Grundzustandsstrukturen multi-dotierten endohedralen Käfigen mit hohen magnetischen Momenten, die über das  $4s^13d^5$  Septettlimit eines einzelnen Atoms hinausgehen.

In den letzten Kapiteln dieser Arbeit werden umfangreiche Zukunftsperspektiven diskutiert. Dies umfasst den Übergang von isolierten einzelnen Siliziumclustern in Richtung solcher Cluster in nicht-trivialen Umgebungen, wie zum Beispiel ausgedehnten Oberflächen, aber auch die Notwendigkeit einer Ausdehnung der Konfigurationssuche auf das großkanonische Ensemble mithilfe der *ab initio*-Thermodynamik Methode um den Einfluss einer finiten Gasphasenumgebung zu berücksichtigen.

# Contents

|   |           |
|---|-----------|
| List of Figures   | ix        |
| List of Tables  | x         |
| Abbreviations   | xi        |
| <b>1 Introduction</b>   | <b>1</b>  |
| <b>I Theoretical Background</b>   | <b>5</b>  |
| <b>2 Describing the Energetics and Electronic Structure of Clusters</b> | <b>6</b>  |
| 2.1 Theoretical Basis of Quantum Chemistry Calculations . . . . .       | 6         |
| 2.2 Density Functional Theory . . . . .                                 | 9         |
| 2.3 Numerical Atom-Centered Basis Sets . . . . .                        | 12        |
| 2.4 Relativity with DFT . . . . .                                       | 14        |
| 2.5 Time-Dependent DFT . . . . .  | 15        |
| 2.6 Density Functional Based Tight Binding . . . . .                    | 16        |
| <b>3 Exploring the Configurational Space of Clusters</b>                | <b>18</b> |
| 3.1 Local Geometry Optimization . . . . .                               | 18        |
| 3.2 Global Geometry Optimization . . . . .                              | 20        |
| <b>4 Statistical Thermodynamics</b>                                     | <b>23</b> |
| 4.1 Partition Function . . . . .  | 23        |
| 4.2 Getting Thermodynamic Functions From Molecular Data . . . . .       | 25        |
| <b>II From Building Blocks to Functionalized Materials</b>              | <b>29</b> |
| <b>5 Stabilization Mechanism of Endohedrally Doped Si Clusters</b>      | <b>31</b> |
| 5.1 Computational Setup . . . . .                                       | 31        |
| 5.2 Cage-like Ground State Geometry . . . . .                           | 33        |
| 5.3 Spherical Potential Model . . . . .                                 | 34        |
| 5.4 Charge Transfer <i>vs.</i> Hybridization . . . . .                  | 36        |
| 5.5 Conclusions to Chapter 5 . . . . .                                  | 39        |
| <b>6 Hydrogenated Si Fullerenes as Magnetic Building Blocks</b>         | <b>41</b> |
| 6.1 $MSi_{16}H_{16}$ ( $M = 3d$ Metal) Clusters . . . . .               | 41        |
| 6.2 $MSi_{20}H_{20}$ ( $M = Co, Ti, V, Cr$ ) Clusters . . . . .         | 43        |
| 6.3 Conclusions to Chapter 6 . . . . .                                  | 48        |
| <b>7 Assembling Functionalized Materials</b>                            | <b>49</b> |
| 7.1 Building Block Monomers . . . . .                                   | 50        |
| 7.2 Dimerization and Trimerization . . . . .                            | 52        |
| 7.3 Routes to Polymerization . . . . .                                  | 55        |
| 7.4 Conclusions to Chapter 7 . . . . .                                  | 59        |

|            |   |            |
|------------|---|------------|
| <b>III</b> | <b>Beyond the Scope of Conventional Cluster Science</b>   | <b>61</b>  |
| <b>8</b>   | <b>Multi-Doped Si Cages: High Spin States Beyond the Septet Limit</b>                                     | <b>62</b>  |
| 8.1        | $M_2\text{Si}_{18}\text{H}_{12}$ Clusters . . . . .   | 63         |
| 8.2        | Electronic Structure of $\text{Cr}_2^+$ , $\text{Mn}_2^+$ , and $\text{CrMn}^+$ Magnetic Dimers . . . . . | 66         |
| 8.3        | $\text{Si}_{24}\text{H}_{24}$ Cage Doped with Magnetic Dimers . . . . .                                   | 68         |
| 8.4        | $\text{Si}_{28}\text{H}_{28}$ Cage Doped with Two $\text{CrMn}^+$ Dimers . . . . .                        | 74         |
| 8.5        | Conclusions to Chapter 8 . . . . .  | 76         |
| <b>9</b>   | <b>Towards Adsorption On Surfaces</b>   | <b>78</b>  |
| 9.1        | Theoretical STM Simulations of the $\text{Si}(111)-(7 \times 7)$ Surface . . . . .                        | 78         |
| 9.2        | Sb/Si Clusters Formation . . . . .  | 81         |
| 9.3        | Conclusions to Chapter 9 . . . . .  | 85         |
| <b>10</b>  | <b>Relative Cluster Stabilities and Beyond</b>  | <b>86</b>  |
| 10.1       | Relative Stability Problem . . . . .  | 86         |
| 10.2       | <i>Ab initio</i> Thermodynamics Approach: Basic Idea . . . . .  | 88         |
| 10.3       | Towards the True Thermodynamics . . . . .   | 90         |
| 10.4       | Conclusions to Chapter 10 . . . . .   | 92         |
| <b>11</b>  | <b>General Conclusions and Outlook</b>  | <b>93</b>  |
|            | <b>Appendix</b>   | <b>97</b>  |
| <b>A</b>   | <b>Basis Sets used in FHI-aims</b>  | <b>98</b>  |
| <b>B</b>   | <b>Low-lying Isomers of Selected Clusters</b>   | <b>99</b>  |
|            | <b>References</b>   | <b>107</b> |
|            | <b>Publications</b>   | <b>125</b> |
|            | <b>Acknowledgements</b>   | <b>126</b> |



# List of Figures

|      |  |    |
|------|--|----|
| 5.1  | Ground state structures of $\text{TiSi}_{16}^+$ , $\text{VSi}_{16}^+$ and $\text{CrSi}_{16}^+$ . . . . .                           | 33 |
| 5.2  | DOS of $\text{TiSi}_{16}^+$ , $\text{VSi}_{16}^+$ and $\text{CrSi}_{16}^+$ . . . . .   | 35 |
| 5.3  | Radial distribution of electron density difference for $\text{VSi}_{16}^+$ . . . . .   | 38 |
| 5.4  | Radial distribution of electron density difference for $\text{TiSi}_{16}^+$ and $\text{CrSi}_{16}^+$ . . . . .                     | 38 |
| 5.5  | Electron density difference $\text{VSi}_{16}^+ - \text{TiSi}_{16}^+$ and $\text{VSi}_{16}^+ - \text{CrSi}_{16}^+$ . . . . .        | 39 |
| 6.1  | Ground-state structures of $M\text{Si}_{16}\text{H}_{16}$ . . . . .  | 42 |
| 6.2  | Ground-state structures of $\text{Si}_n\text{H}_n$ , $n = 20, 24, 26, 28$ . . . . .  | 44 |
| 6.3  | Radial spin density and DOS of $\text{CrSi}_{20}\text{H}_{20}$ . . . . .   | 44 |
| 6.4  | Optical absorption spectrum of $\text{CrSi}_{20}\text{H}_{20}$ . . . . .   | 46 |
| 7.1  | Ground-state structures of $\text{CrSi}_{20}\text{H}_{20-n}$ . . . . .   | 50 |
| 7.2  | DOS of $\text{CrSi}_{20}\text{H}_{19}$ . . . . .   | 51 |
| 7.3  | Ground-state structures of $(\text{CrSi}_{20}\text{H}_{19})_2$ and $(\text{CrSi}_{20}\text{H}_{18})_2$ dimers . . . . .            | 53 |
| 7.4  | DOS and optical absorption spectrum of $(\text{CrSi}_{20}\text{H}_{18})_2$ . . . . .   | 54 |
| 7.5  | Ground-state structure of the trimer aggregate . . . . .   | 56 |
| 7.6  | Locally optimized octahedral aggregate . . . . .   | 57 |
| 7.7  | DOS of clathrate structures . . . . .  | 58 |
| 8.1  | Ground-state structures of $\text{CrSi}_{12}$ , $\text{Cr}_2\text{Si}_{18}$ and $\text{Cr}_2\text{Si}_{18}\text{H}_{12}$ . . . . . | 64 |
| 8.2  | DOS of the $\text{CrSi}_{12}$ and $\text{Cr}_2\text{Si}_{18}$ clusters . . . . .   | 64 |
| 8.3  | Ground-state structures of $\text{Fe}_2\text{Si}_{18}$ and $\text{Fe}_2\text{Si}_{18}\text{H}_{12}$ . . . . .                      | 66 |
| 8.4  | Selected cage-like structures of $\text{Cr}_2^+\text{@Si}_{24}\text{H}_{24}$ . . . . .   | 69 |
| 8.5  | $\text{Cr}_2^+\text{@Si}_{24}\text{H}_{24}$ (ground-state) DOS . . . . .   | 70 |
| 8.6  | Total and spin density difference for $\text{Cr}_2^+\text{@Si}_{24}\text{H}_{24}$ (ground-state) . . . . .                         | 71 |
| 8.7  | Spin density difference for $\text{Cr}_2^+\text{@Si}_{24}\text{H}_{24}$ (structure II) . . . . .                                   | 72 |
| 8.8  | Ground-state structures of $\text{Mn}_2^+\text{@Si}_{24}\text{H}_{24}$ and $\text{CrMn}^+\text{@}_{24}\text{H}_{24}$ . . . . .     | 72 |
| 8.9  | DOS for $\text{CrMn}^+\text{@Si}_{24}\text{H}_{24}$ and $\text{Mn}_2^+\text{@Si}_{24}\text{H}_{24}$ . . . . .                      | 73 |
| 8.10 | Spin density difference for $\text{CrMn}^+\text{@Si}_{24}\text{H}_{24}$ and $\text{Mn}_2^+\text{@Si}_{24}\text{H}_{24}$ . . . . .  | 74 |
| 8.11 | $(\text{CrMn}^+)_2\text{@Si}_{28}\text{H}_{28}$ (ground-state) DOS . . . . .   | 75 |
| 8.12 | $(\text{CrMn}^+)_2\text{@Si}_{28}\text{H}_{28}$ spin density distribution . . . . .  | 76 |
| 9.1  | $\text{Si}(111)7 \times 7$ DAS model . . . . .   | 79 |
| 9.2  | $\text{Si}(111)7 \times 7$ surface simulated STM . . . . .   | 80 |
| 9.3  | Experimental STM image of the ring-like clusters . . . . .   | 81 |
| 9.4  | Ground-state structure of the $\text{Si}_7\text{Sb}_3$ cluster . . . . .   | 82 |
| 9.5  | Simulated STM picture of the $\text{Si}_7\text{Sb}_3$ clusters . . . . .   | 82 |
| 9.6  | Locally optimized structure of the $\text{Si}_6\text{Sb}_3$ cluster . . . . .  | 83 |
| 9.7  | Simulated STM picture of the $\text{Si}_6\text{Sb}_3$ clusters . . . . .   | 84 |
| 9.8  | Global minimum and STM of the $\text{Si}_6\text{Sb}_3$ cluster . . . . .   | 84 |
| 10.1 | Relative stabilities of $\text{TiSi}_n$ clusters based on binding energies . . . . .   | 87 |
| 10.2 | Relative stabilities of $\text{TiSi}_n$ clusters based on Gibbs free energies . . . . .  | 89 |
| 10.3 | Relative stabilities of $\text{CuSi}_n^+$ clusters based on Gibbs free energies . . . . .  | 90 |

# List of Tables

|      |  |     |
|------|--|-----|
| 5.1  | $MSi_{16}^+$ ( $M = \text{Ti, V, Cr}$ ) HOMO and LUMO levels                     | 36  |
| 5.2  | $MSi_{16}^+$ frontier orbitals   | 37  |
| 6.1  | Ti, V, Cr, and Co atomic spin states   | 43  |
| 6.2  | $CrSi_{20}H_{20}$ frontier orbitals  | 45  |
| 6.3  | $MSi_nH_n$ Kohn-Sham levels and binding energies                                 | 47  |
| 7.1  | Hydrogen abstraction cost for $CrSi_{20}H_{20-2n}$ clusters                      | 52  |
| 7.2  | $CrSi_{20}H_{18}$ monomer frontier orbitals                                      | 55  |
| 7.3  | $(CrSi_{20}H_{18})_2$ dimer frontier orbitals                                    | 56  |
| 8.1  | $CrSi_{12}$ and $Cr_2Si_{18}$ frontier orbitals                                  | 65  |
| 8.2  | Relative stabilities of different $Cr_2^+$ , $Mn_2^+$ , and $CrMn^+$ spin states | 67  |
| 8.3  | Relative stabilities of different $Cr_2$ and $Mn_2$ spin states                  | 68  |
| 10.1 | Relative stabilities of $TiSi_n$ and $MSi_{16}$ clusters                         | 87  |
| 10.2 | Chemical potentials of Si atoms in $TiSi_n$ clusters                             | 91  |
| 10.3 | Chemical potentials of Si atoms in $CuSi_n^+$ clusters                           | 92  |
| A.1  | FHI-aims basis sets  | 98  |
| B.1  | $VSi_{16}^+$ low-lying isomers   | 99  |
| B.2  | $CrSi_{16}H_{16}$ low-lying isomers  | 100 |
| B.3  | $CrSi_{20}H_{20}$ low-lying isomers  | 101 |
| B.4  | $CrSi_{20}H_{18}$ monomer low-lying isomers                                      | 102 |
| B.5  | $(CrSi_{20}H_{18})_2$ dimer low-lying isomers                                    | 103 |
| B.6  | $CrMn^+@CrSi_{24}H_{24}$ low-lying isomers                                       | 104 |
| B.7  | $(CrMn^+)_2@CrSi_{28}H_{28}$ low-lying isomers                                   | 105 |

# Abbreviations

|                 |  |
|-----------------|--|
| <b>AO</b>       | <b>A</b> tomic <b>O</b> rbital   |
| <b>B3LYP</b>    | hybrid semi-empirical functional ( <b>B</b> ecke <b>3</b> -parameter <b>L</b> ee- <b>Y</b> ang- <b>P</b> arr)  |
| <b>BFGS</b>     | <b>B</b> royden- <b>F</b> letcher- <b>G</b> oldfarb- <b>S</b> hanno local optimization algorithm   |
| <b>BH</b>       | <b>B</b> asin <b>H</b> opping global optimization scheme   |
| <b>BSSE</b>     | <b>B</b> asis <b>S</b> et <b>S</b> uperposition <b>E</b> rror  |
| <b>CASSCF</b>   | <b>C</b> omplete <b>A</b> ctive <b>S</b> pace multi-configurational <b>S</b> elf- <b>C</b> onsistent <b>F</b> ield   |
| <b>CI</b>       | <b>C</b> onfigurational <b>I</b> nteraction  |
| <b>DAS</b>      | <b>D</b> imer- <b>A</b> datom <b>S</b> tacking-fault model of Si(111)-(7×7) surface  |
| <b>DFT</b>      | <b>D</b> ensity <b>F</b> unctional <b>T</b> heory  |
| <b>DFTB</b>     | <b>D</b> ensity <b>F</b> unctional based <b>T</b> ight <b>B</b> inding   |
| <b>DOS</b>      | <b>D</b> ensity <b>O</b> f <b>S</b> tates  |
| <b>FHI-aims</b> | <b>F</b> ritz- <b>H</b> aber- <b>I</b> nstitut <i>ab initio</i> molecular simulations package  |
| <b>FHUC</b>     | <b>F</b> aulted <b>H</b> alf of the <b>U</b> nit <b>C</b> ell  |
| <b>GGA</b>      | <b>G</b> eneralized <b>G</b> radient <b>A</b> pproximation   |
| <b>HF</b>       | <b>H</b> artree- <b>F</b> ock method   |
| <b>HOMO</b>     | <b>H</b> ighest <b>O</b> ccupied <b>M</b> olecular <b>O</b> rbital   |
| <b>LANL2DZ</b>  | effective core potential double-zeta type basis set ( <b>L</b> os <b>A</b> lamos <b>N</b> ational <b>L</b> aboratory <b>2</b> <b>D</b> ouble <b>Z</b> eta) |
| <b>LCAO</b>     | <b>L</b> inear <b>C</b> ombination of <b>A</b> tomic <b>O</b> rbitals  |
| <b>LDA</b>      | <b>L</b> ocal <b>D</b> ensity <b>A</b> pproximation  |
| <b>LUMO</b>     | <b>L</b> owest <b>U</b> noccupied <b>M</b> olecular <b>O</b> rbital  |
| <b>MD</b>       | <b>M</b> olecular <b>D</b> ynamics   |
| <b>MO</b>       | <b>M</b> olecular <b>O</b> rbital  |
| <b>PBE</b>      | semi-local functional due to <b>P</b> erdew, <b>B</b> urke and <b>E</b> rnzerhof   |
| <b>PBE0</b>     | <b>P</b> BE-based <b>0</b> -parameter hybrid functional by Adamo and Barone  |
| <b>PES</b>      | <b>P</b> otential <b>E</b> nergy <b>S</b> urface   |
| <b>RHF</b>      | <b>R</b> estricted <b>H</b> artree- <b>F</b> ock method  |
| <b>SCF</b>      | <b>S</b> elf- <b>C</b> onsistent <b>F</b> ield   |
| <b>STM</b>      | <b>S</b> canning <b>T</b> unneling <b>M</b> icroscopy  |
| <b>TD-DFT</b>   | <b>T</b> ime- <b>D</b> ependent <b>D</b> ensity <b>F</b> unctional <b>T</b> heory  |
| <b>UHUC</b>     | <b>U</b> nfaulted <b>H</b> alf of the <b>U</b> nit <b>C</b> ell  |
| <b>ZORA</b>     | <b>Z</b> eroth- <b>O</b> rders <b>R</b> egular <b>A</b> pproximation for relativistic effects  |

“We are reaching the stage where the problems we must solve are going to become insoluble without computers. I do not fear computers, I fear the lack of them”.

Isaac Asimov

# 1 Introduction

Clusters are relatively small (containing a countable number of particles) aggregates of atoms and therefore, in terms of size, bridge the gap between individual atoms (or small molecules) and bulk matter [1]. However, physical and chemical properties of clusters differ from those found in both individual atoms and bulk systems, and display a unique dependence on size, geometry and composition. Most intriguingly, unlike in case of bulk materials, the properties of clusters do not scale linearly with size, but rather exhibit discontinuous behavior, where “every atom matters” [2, 3]. This can be clearly illustrated by the dramatic change of electronic structure when the system is reduced to a few atoms, where the more-or-less continuous density of states is replaced by a set of discrete energy levels. Such an intricate relationship between structural and electronic properties offers a unique opportunity to tailor optical, magnetic and chemical properties through selection of size and composition, thus providing the field of nanoscale science the promising prospect of using clusters as building blocks for constructing novel materials [4]. Another exciting feature of clusters is an unusually high surface to volume ratio. A large fraction of surface atoms makes, for instance, metal clusters ideal candidates for applications in catalysis, and modeling active sites of surfaces [5].

Both the possibility of creating clusters with appealing geometries, and their potentially highly-tunable optoelectronic and catalytic properties meet in the field of nanoscale assembly [6, 7]. Construction of new materials with engineered properties using clusters as building blocks presents a “bottom up” multiscale approach in material science, focusing on systems whose properties vary dramatically with composition [8]. Obviously, building such materials presents its own new challenges, connected to describing a new set of superatomic building blocks and understanding their individual and material properties. To date the building blocks used in cluster-assembled materials range from fullerenes and small clusters to larger nanoparticles [9]. Especially interesting are, of course, functionalized materials made of endohedrally doped clusters, which appears as a remarkable avenue to tailor the intrinsic properties of clusters — idea initially suggested for carbon fullerene cages [10, 11, 12]. For instance, multi-doping of large cages is recognized as promising method of modifying physical and chemical properties through endohedral chemical functionalization [13].

The prevalence of silicon in the semiconductor industry and its wide abundance (silicon is the second most abundant element in the Earth’s crust after oxygen [14]) has sparked great interest in silicon-based nanostructures that could act as building blocks for new easy-to-integrate and engineered materials. In contrast to the compact and reactive form of pure Si clusters, determined by unsaturated dangling Si bonds due to typical preference of  $sp^3$  bonding [15], endohedral metal doping was found to produce saturated fullerene and other polyhedral cage structures that represent appealing symmetric and

## 1 Introduction

unreactive building blocks, and therewith an intriguing novel nanoform of Si with great promise for *e.g.* optoelectronic device applications [16, 17, 18, 19]. For instance, the groups of Balbás [20] and Nakajima [21] have demonstrated the theoretical possibility of building homo- and heterogeneous aggregates of  $MSi_{16}$  clusters with different metal dopants.

Of course, employing these potential functionalities implies resolving structural information on an atomic level and a comprehensive description of electronic structure. Already the first point causes a lot of complications, since there are no experimental methods available that can directly give such structural information on clusters. The size of the formed clusters can be deduced from the mass spectra [22, 23], or even the formation of clusters of certain shape (*e.g.* cages) can be inferred experimentally from reactivity [24, 25, 26, 27], photodissociation [28], physisorption [29] and X-ray absorption spectroscopy [30] studies. However, detailed geometrical information at the atomic level is not available experimentally. Obviously, there is a direct correlation between the geometric and electronic structure, which is detected by experiment. This is where theory comes into play and provides required information to assign the experimental data to the underlying structure. For instance, by comparison of calculated spectral features for a set of isomers to the experimentally observed spectrum it is possible to determine the geometry of the cluster. Such a combined experimental/theoretical approach has been widely used to assign cluster structures based on *e.g.* photoelectron spectroscopy [31] and vibrational spectroscopy, for instance far-infrared vibrational resonance enhanced multiple photon dissociation spectroscopy [32, 33, 34], as well as several other methods [35].

However, within such strategy, geometric information is needed as starting point for the computational spectroscopy investigations. A conventional approach is to try several structures, the choice of which is guided merely by chemical intuition and/or information about the structures of adjacent-sized clusters, *i.e.* with one atom less or more. Obviously, such approach may be very misleading, since clusters typically possess complex potential energy surfaces (PES) with multiple minima. Even for a three-atomic cluster one can easily suggest several different geometries: linear, equilateral triangle, isosceles triangle and a scalene triangle. The rapid growth of the number of local PES minima, or in other words metastable isomers, with increasing cluster size quickly limits approaches focusing only on local structure optimization [36]. Required instead are more systematic unbiased sampling techniques that allow a global and efficient exploration of the huge configurational space, thus providing the possibility to deal with the challenge of exponential increase of the number of local minima with system size. This steep growth is *e.g.* known as Levinthal's paradox, according to which a protein would never reach its native state within the lifetime of the universe if it had to go through all local minima randomly [37]. Among several available global geometry optimization schemes, such as the classical sim-

ulated annealing algorithm based on methods of statistical mechanics [38] or fashionable genetic algorithms that mimic Darwin’s principle of survival of the fittest [39], a Monte-Carlo minimization scheme by Wales and Doye [40] known as basin-hopping proved to be very efficient in determining both ground-state structure and low-lying isomers of a given cluster composition [41].

A further complication arises from the fact that a true predictive-quality search for optimal building blocks to be used for new materials should go beyond the micro-canonical ensemble sampling. In its classical formulation global geometry optimization samples for a fixed number of species, *i.e.* it only identifies the optimum structure for a defined composition. In reality, aggregation or decomposition with varying number of atoms can take place. In the spirit of *ab initio* thermodynamics [42] the cluster environment can be reduced to chemical potentials with which the cluster is in equilibrium. It is then possible (albeit has not yet been done in the cluster context) to sample the ground-state geometries for a wide range of compositions (*e.g.* cluster sizes  $MSi_n$ ) and compare their stabilities for any given (for instance Si) chemical potential.

Of course, structural information is not enough for studying clusters as potential building blocks for new materials. A comprehensive description of bonding in building block monomers and obtained aggregates is an important and necessary further step for a deeper understanding of possible polymerization mechanisms. To obtain this information, state-of-the-art density functional theory (DFT) [43, 44] methods need to be employed.

Altogether, these prospects and challenges motivate the present work on controlled functionalization of endohedrally doped silicon clusters as building-blocks for cluster-assembled materials. Aiming at *ab initio* predictive-quality modeling of novel engineered materials, we conduct a systematic step-by-step investigation of the prospects of bringing the unique magnetic and optical properties of transition metals to the synthetically feasible nanometer-scale aggregates. The thesis is structured as follows:

In Part I, a concise introduction to different employed methodologies and concepts to explore the configurational space and thoroughly describe the electronic structure and properties of doped silicon clusters, on which this work is based, is given. These comprise density functional theory (including its time-dependent formulation for excited states calculations (TD-DFT) [45, 46] and density functional based tight binding (DFTB) for optimizing large, computationally heavy systems [47, 48]) in Chapter 2, and methods of sampling of the potential energy surface (both locally and globally) in Chapter 3. The methods of calculating potential functions based on statistical thermodynamics are presented in Chapter 4.

Results obtained for *3d* transition metal doped  $Si_{16}$  and  $Si_{20}$  cage-like clusters are grouped in Part II, presenting a systematic study from understanding the nature of bonding within the doped Si clusters, *via* tuning the magnetic moments of such clusters, and towards building engineered functionalized cluster-assembled materials. First, the

## 1 Introduction

geometric and electronic structure of cationic  $MSi_{16}^+$  clusters with Ti, V and Cr dopant atoms is studied in Chapter 5. The analysis of the electronic manifold traces the diminished role of shell closure for the stabilization of the endohedral cage geometry back to the adaptive capability of the metal-Si bonding, which is a result of a complex hybridization. Based on these findings, in Chapter 6 the possibility of creating cage structures with minimized  $M$ -Si interaction to preserve unique atomic properties of the dopant is scrutinized. Perfectly symmetric  $MSi_{20}H_{20}$  ( $M = 3d$  metal) cages with Si dangling bonds saturated by hydrogen termination are found to conserve the atomic character of the dopants, *i.e.* high magnetic moments and optical properties. Inspired by these results, in Chapter 7 we assess the feasibility of potential synthetic polymerization routes of such highly magnetic building block clusters *via* controlled dehydrogenation. In contrast to the known clathrate-type facet sharing, a predisposition to aggregation through double Si-Si bridge bonds is found, and a toolbox of  $MSi_{20}H_{20-2n}$  monomers with different number of double “docking sites” is suggested, which allows building network architectures of any morphology.

Part III focuses on further ongoing developments that go beyond the conventional scope of cluster science studies. In Chapter 8 the possibility of multi-doping of Si clusters in order to achieve high spin states beyond the single-atom dopant septet limit is critically evaluated. For instance, we show that it is possible to conserve both the structural integrity of the host cage and the high spin state of the guest dimer dopant in case of  $M_2^+@Si_{24}H_{24}$  aggregates (with  $M = Cr_2^+$ ,  $Mn_2^+$  and  $MnCr^+$ ), thereby exceeding the magnetic moment feasible with single-atom dopants by almost a factor of two. Moreover, the possibility of further increasing the cluster spin state by encapsulating a different number of dopant atoms into a suitably sized hydrogenated Si cage is illustrated with the example of a  $(CrMn^+)_2@_{28}H_{28}$  aggregate with the total number of 18 unpaired electrons. Chapter 9 is devoted to moving from the study of isolated individual Si clusters towards the properties of such clusters in a non-trivial environment, *i.e.* under the influence of other bonding partners, such as extended surfaces. Finally, Chapter 10 introduces an important discussion of grand-canonical ensemble sampling. Within the *ab initio* thermodynamics approach we discuss the possibility of predicting relative stabilities of clusters of different size. These developments offer many potential future applications beyond the specific problem of doped Si clusters. Some of these are surveyed in a concluding outlook in Chapter 11.

A detailed discussion of current developments within the field, together with an overview of the relevant literature, is given at the beginning of each respective chapter, instead of cumulating it into a separate state-of-the-art section, which gives the possibility of continuous narration, following the logic of the research presented here.



Part I

# Theoretical Background

## 2 Describing the Energetics and Electronic Structure of Clusters

### 2.1 Theoretical Basis of Quantum Chemistry Calculations

The basic equation of quantum mechanics is the Schrödinger equation [49], that yields a wavefunction  $\psi$ , from which all physical properties of the system can be found. The time-dependent Schrödinger equation for a particle, described by the wavefunction  $\psi$  and moving in a potential  $V$ , is a second-order differential equation:

$$\left(-\frac{\hbar^2}{2m}\nabla^2 + \hat{V}\right)\psi(\vec{r}, t) = i\hbar\frac{\partial\psi(\vec{r}, t)}{\partial t}, \quad (2.1)$$

where  $\psi$  is a wavefunction,  $\vec{r}$  – position vector,  $t$  – time,  $\nabla^2$  – Laplacian,  $\hat{V}$  – potential energy operator, and  $\hbar$  – Planck constant divided by  $2\pi$ . The Hamiltonian is defined as

$$\hat{H} = \left[-\frac{\hbar^2}{2m}\nabla^2 + \hat{V}\right], \quad (2.2)$$

*i.e.* it is a sum of kinetic and potential energy operators. The stationary Schrödinger equation is a first-order differential equation:

$$\hat{H}_{\text{tot}}\psi_{\text{tot}} = E_{\text{tot}}\psi_{\text{tot}}, \quad (2.3)$$

where  $E_{\text{tot}}$  and  $\psi_{\text{tot}}$  are eigenvalue and eigenfunction of the Hamiltonian, respectively. The Hamiltonian consists of five terms: kinetic energy of electrons  $\hat{T}_e$ , kinetic energy of nuclei  $\hat{T}_n$ , potential energy of electron-electron interaction  $\hat{V}_{ee}$ , potential energy of nuclei interaction  $\hat{V}_{nn}$ , and potential energy of electron-nucleus interaction  $\hat{V}_{ne}$ .

However, electrons are much lighter than nuclei, therefore they move much faster. Within this assumption, a Born-Oppenheimer approximation [50] is introduced, according to which nuclei are fixed, while only electrons move. Thus, the total wavefunction can be separated into two parts: an electronic part  $\psi_e$  and a nuclear part  $\psi_n$ . In this view, electrons move in a potential field created by the nuclei, and the Schrödinger equation for the electron wavefunction  $\psi_e$  is written as follows:

$$\left(\hat{H}_e + \hat{V}_{nn}\right)\psi_e(\vec{r}, \vec{R}) = E_e(\vec{R})\psi_e(\vec{r}, \vec{R}), \quad (2.4)$$

where  $\vec{r}$  is a position vector for electrons,  $\vec{R}$  – position vector for nuclei. For the chemistry applications in this thesis the electronic wavefunction is sufficient. The nuclei interaction constant  $V_{nn}$  can be added after solving the electron Schrödinger equation, when the PES, on which nuclei can move, is known. The deepest minimum point on such a surface

## 2.1 Theoretical Basis of Quantum Chemistry Calculations

corresponds to the optimal geometry. Thus we have  $\hat{H} = \hat{T}_e + \hat{V}_{ee} + \hat{V}_{ne}$ ,  $\psi = \psi_e$ ,  $E = E_e$ , and can re-write the Schrödinger equation in a simpler form:

$$\hat{H}\psi = E\psi . \quad (2.5)$$

After multiplying by the complex conjugate and integrating over volume

$$\int \psi^* \hat{H}\psi dv = \int \psi^* E\psi dv , \quad (2.6)$$

a scalar value of the energy  $E$  can be found as:

$$E = \frac{\int \psi^* \hat{H}\psi dv}{\int \psi^* \psi dv} . \quad (2.7)$$

In most cases, finding the exact form of the wavefunction is unfeasible. Therefore, additional approximations are introduced to simplify the calculation. Historically the first and most widely used approximation is the Hartree-Fock (HF) method [51]. In order to solve the Schrödinger equation for a multi-electron system, the approximation of non-interacting electrons is introduced. In this case the total wavefunction can be described as a product of one-electron wavefunctions. The Hamiltonian for every electron is:

$$\hat{h}_i = \hat{T}_i + \sum_n \hat{V}_{ni} , \quad (2.8)$$

where  $\hat{T}_i$  is electron kinetic energy, and  $\hat{V}_{ni}$  the potential energy of electron-nucleus interaction. Thus, the Schrödinger equation can be solved for a single-electron system  $\hat{h}_i\psi_i = \varepsilon_i\psi_i$ , where  $\psi_i$  are single-electron wavefunctions and  $\varepsilon_i$  the corresponding energy values. However, such a single-electron composed wavefunction does not properly describe the anti-symmetrization requirement for fermionic systems, known as Pauli principle [52]. Slater therefore suggested to use a linear combination of single-electron spin functions in form of a determinant [53], which then describes the many-electron wavefunction with proper account for the symmetry and the Pauli principle. Such an  $N$ -electron Slater wavefunction is written as:

$$\psi = \frac{1}{\sqrt{N!}} \begin{vmatrix} \chi_1(1) & \dots & \chi_N(1) \\ \vdots & \dots & \vdots \\ \chi_1(N) & \dots & \chi_N(N) \end{vmatrix} , \quad (2.9)$$

where  $\chi$  is a spin function, *i.e.* a single-electron function which accounts for spin. For the given expression of the determinant, all functions describe occupied orbitals.

Within the restricted Hartree-Fock (RHF) method [54, 55] all electrons are paired. Then the set of paired differential equations can be written in form of the Hartree-Fock

## 2 Describing the Energetics and Electronic Structure of Clusters

equations  $f_i\psi_i = \varepsilon_i\psi_i$ , where  $\varepsilon_i$  are the energy eigenvalues for single-electron functions  $\psi_i$ , and  $f_i$  – Fock operator:

$$f_i = \hat{h}_i + \sum_{j=1}^N (J_j(1) - K_j(1)) . \quad (2.10)$$

In eq. (2.10) a summation is done over the number of electrons  $N$ . “1” means that the operator includes coordinates of one electron only.  $J$  is a Coulomb integral describing the electrostatic repulsion between electrons,  $K$  is the exchange integral.

Within the Hartree-Fock method each electron occupies its own orbital and moves within the potential field of the other  $N - 1$  electrons. Thus, electrons can be located closer to each other than they would be, if the energy of each electron was minimized individually. Therefore, the HF method always overestimates the energy. The difference between the energy in the Hartree-Fock limit and the exact non-relativistic energy of a system is designated as correlation energy  $E_{\text{corr}} = E_{\text{exact}} - E_{\text{HF}}$ . Thus, the sum of single-electron energy values does not equal the total energy of the system. Electron-electron interaction is calculated twice upon summation of single-electron energies, and should be corrected through division of the full interaction by two. Then the total energy is:

$$E_{\text{HF}} = \sum \varepsilon_i - \frac{1}{2} \sum_i \sum_j (J_{ij} - K_{ij}) . \quad (2.11)$$

Solution of the Hartree-Fock equations yields molecular orbitals, which describe the spatial distribution of the probability of finding an electron. Each orbital corresponds to a certain energy level. Orbitals are occupied by maximum of two electrons each, starting from the energetically lowest. Occupation of  $N$  orbitals with minimal energy values then yields a minimal total energy, which corresponds to the ground state of the system. The remaining high-energy orbitals are called virtual orbitals. Especially important for chemical applications are the so-called frontier orbitals, *i.e.* the highest occupied (HOMO) and lowest unoccupied (LUMO) molecular orbitals.

Molecular orbitals (MO) filled with electrons are mathematical functions, which can be represented as linear combinations of atomic orbitals (LCAO):

$$\psi_i = \sum_{\mu} C_{\mu i} \phi_{\mu} , \quad (2.12)$$

where  $C_{\mu i}$  is a coefficient,  $\phi_{\mu}$  is an atomic orbital (AO). Atomic orbitals are the solutions of the Schrödinger equation for a hydrogen atom, *i.e.* the orbitals of the hydrogen atom ( $1s, 2s, 2p, 3s, 3p, \dots$ ). The LCAO method allows constructing molecular orbitals using already known functions with only coefficients unknown. Integration over the volume

gives the Roothaan equation [56]:

$$FC = SC\varepsilon, \quad (2.13)$$

where  $F$  is the Fock matrix,  $S$  and  $C$  are matrices with overlap integrals  $S_{\mu\nu}$  and coefficients  $C_{\mu\nu}$ . The matrix elements are

$$F_{\mu\nu} = \int \phi_\nu^* f \phi_\mu dV \quad \text{and} \quad S_{\mu\nu} = \int \phi_\nu^* \phi_\mu dV. \quad (2.14)$$

The solution of the equations can be considered as a procedure of energy minimization, where, according to the variational principle, the best wavefunction corresponds to the minimal energy. The problem can be solved iteratively, with the coefficients  $C_{\mu\nu}$  found by the energy minimization. Such procedure is known as self-consistent field (SCF).

## 2.2 Density Functional Theory

One of the most common present-day computational chemistry approaches is based on the density functional theory (DFT). Within this method, the main variable of quantum mechanics, wavefunction  $\psi$ , is substituted by the electron density  $\rho(r)$ , which is a function of only three spatial coordinates. The total energy, as well as any other observable property of a molecular system, can be defined through  $\rho(r)$  *via* so-called functionals.<sup>1</sup>

According to the Hohenberg-Kohn theorems [43], the electron density can be considered as a variable in many-electron theory. When the ground-state electron density of a system is known, it is possible to calculate energy of the ground state and all molecular properties. The second Hohenberg-Kohn theorem states that the energy of the given configuration obeys the variational principle, and among all possible electron density distributions the one that yields the minimal energy is the ground-state density. However, the Hohenberg-Kohn theorems do not give an exact form of the  $E(\rho)$  functional needed to evaluate such a minimization.

The Kohn-Sham scheme [44] is currently the main procedure for the explicit calculation of electron density and energy for any atomic and molecular system, and is the basis of most present-day DFT calculations. The main goal of the Kohn-Sham method is to calculate a hypothetical system composed of  $N$  electrons, which do not interact with each other, occupy  $N$  orbitals  $\psi_i$ , and move within the potential field  $v_s$ . For this type of systems, the Slater determinant rigorously describes the wavefunction in the ground state. Optimal orbitals for the system can be found by solving single-electron equations:

$$\left(-\frac{1}{2}\nabla^2 + v_s\right)\psi_i = \varepsilon_i\psi_i. \quad (2.15)$$

---

<sup>1</sup>For an extended discussion of Density Functional Theory see ref. [57]. For detailed derivations consult ref. [58].

## 2 Describing the Energetics and Electronic Structure of Clusters

Here, the Hamiltonian consists of the kinetic energy operator and a single-particle effective potential. The total electron density is a sum of orbital densities:

$$\rho_s(\vec{r}) = \sum_{i=1}^N |\psi_i(\vec{r})|^2. \quad (2.16)$$

The connection of the system where there is no electron-electron interaction with the true system, where electrons do interact, can be assessed *via* the choice of an effective potential of one particle in such a way that the electron distribution corresponds to the density distribution of the real system in its ground state. Despite the fact that the exact expression for the density functional  $E(\rho)$  is unknown, its constituent parts can be expressed as follows:

$$E_{\text{DFT}}(\rho) = T_{\text{S}}(\rho) + E_{ne}(\rho) + J(\rho) + E_{\text{XC}}(\rho), \quad (2.17)$$

where  $\rho$  is the density of the system of interacting electrons. The form of the first three terms is known.  $T_{\text{S}}(\rho)$  is the kinetic energy of the system with non-interacting electrons,  $E_{ne}(\rho)$  is the potential energy of the Coulomb interaction between nuclei and electrons, and  $J(\rho)$  is the energy of inter-nuclei repulsion. All other terms are accounted for in the fourth term  $E_{\text{XC}}(\rho)$ , the exchange-correlation functional.  $E_{\text{XC}}(\rho)$  includes all non-classical interaction effects, as well as the part of kinetic energy not included in  $T_{\text{S}}(\rho)$ . The exchange-correlation functional also corrects the  $J(\rho)$ , which allows for a non-physical interaction of the electron with itself. Taking into account eq. (2.16), one can rewrite the eq. (2.17) in the following form:

$$\begin{aligned} E(\rho) = & -\frac{1}{2} \sum_{i=1}^N \int \psi_i^*(\vec{r}) \nabla^2 \psi_i(\vec{r}) d\vec{r} - \sum_{i=1}^N \int \sum_{A=1}^M \frac{Z_A}{|R_A - \vec{r}|} |\psi_i(\vec{r})|^2 d\vec{r} + \\ & \frac{1}{2} \sum_{i=1}^N \sum_{j=1}^N \int \int |\psi_i(\vec{r})|^2 \frac{1}{|\vec{r} - \vec{r}'|} |\psi_j(\vec{r}')|^2 d\vec{r} d\vec{r}' + E_{\text{XC}}(\rho), \end{aligned} \quad (2.18)$$

where  $M$  and  $N$  are the number of nuclei and electrons, respectively. The energy minimization after normalization of the wavefunction yields a set of single-electron Kohn-Sham equations:

$$\hat{h}_{\text{KS}} \psi_i = \varepsilon_i \psi_i, \quad i = 1, 2, \dots, N. \quad (2.19)$$

The single-electron operator  $\hat{h}_{\text{KS}}$  contains the kinetic energy, nuclei potential, the classical Coulomb potential and the potential caused by  $E_{\text{XC}}(\rho)$ :

$$\hat{h}_{\text{KS}} = -\frac{1}{2} \nabla^2 - \sum_A \frac{Z_A}{|R_A - \vec{r}|} + \int \frac{\rho(\vec{r}')}{|\vec{r} - \vec{r}'|} d\vec{r}' + v_{\text{XC}}(\vec{r}) = -\frac{1}{2} \nabla^2 + v_{\text{eff}}(\vec{r}). \quad (2.20)$$

The exchange-correlation potential  $v_{\text{XC}}$  is defined as the functional derivative of the

exchange-correlation energy with respect to  $\rho$ :  $v_{\text{XC}} = \frac{\partial E_{\text{XC}}[\rho]}{\partial \rho(\vec{r})}$ . Comparison of eqs. (2.15), (2.19) and (2.20) reveals that if the potential of a single particle  $v_s$  in eq. (2.15) is defined as  $v_{\text{eff}}(\vec{r})$  in eq. (2.20), then the system with non-interacting electrons transforms into a system where electrons do interact. Thus, the Kohn-Sham equations appear after substitution  $v_s = v_{\text{eff}}(\vec{r})$  in eq. (2.15), and the solution of this equation yields the Kohn-Sham orbitals.  $v_{\text{eff}}(\vec{r})$  depends on the electron density, and in order to find the Kohn-Sham orbitals, eq. (2.19) needs to be solved iteratively using the SCF procedure, just like in the HF method. The energy of the system can be obtained by inserting the electron density found from the Kohn-Sham orbitals (eq. (2.16)) into the eq. (2.17).

As it has been mentioned before, the exact form of the exchange-correlation functional is unknown. Therefore, the quality of the solution obtained withing the DFT framework is directly dependent on the chosen functional  $E_{\text{XC}}$  [59]. Exchange-correlation functionals can be classified according to the way the electron density distribution is described. The simplest approximation is the local density approximation (LDA), with the idea of a hypothetical uniform electron gas, where the electrons sit in an infinite region of space, with a uniform positive external potential, chosen to preserve overall charge neutrality. Then  $E_{\text{XC}}^{\text{LDA}}$  is:

$$E_{\text{XC}}^{\text{LDA}} = \int \rho(\vec{r}) \varepsilon_{\text{XC}}(\rho(\vec{r})) d(\vec{r}) , \quad (2.21)$$

where  $\varepsilon_{\text{XC}}$  is a functional that depends only on the local density at each point  $\vec{r}$ . The exchange-correlation functional can further be divided into two parts  $E_{\text{XC}} = E_{\text{X}} + E_{\text{C}}$ , where  $E_{\text{X}}$  and  $E_{\text{C}}$  are functionals accounting for exchange and correlation parts of the energy, respectively. The form of the exchange part  $E_{\text{X}}$  for the homogeneous electron gas is known, and was originally derived by Bloch [60] and Dirac [61]. No such explicit expression is known for the correlation part  $E_{\text{C}}$ , however. Several authors developed their representations of  $E_{\text{C}}$  [62, 63, 64]. The most recent and accurate one has been suggested by Perdew and Wang [65]. These functionals can be successfully used in systems where the real density resembles the one of the uniform electron gas, *e.g.* in metals.

A step forward in comparison to LDA was done in another (and probably the most widely used nowadays) method: the generalized gradient approximation (GGA). There, not only information about the density  $\rho(\vec{r})$  at a particular point  $\vec{r}$ , but also information about the gradient of the charge density  $\nabla\rho(\vec{r})$  is used in the evaluation of  $E_{\text{XC}}$ , to account for the non-homogeneity of the true electron density. The general form of the GGA exchange-correlation functional is:

$$E_{\text{XC}}^{\text{GGA}} = \int f(\rho, \nabla\rho) d\vec{r} . \quad (2.22)$$

Such functionals are better suited for molecular systems, where the electron density is clearly not uniform. Several GGA functionals have been suggested [66, 67, 68], the most widely used being the PBE functional by Perdew, Burke and Ernzerhof [69]. As

it is also the case for the LDA, spin-polarized versions of these functionals (for collinear treatment of spin) have been developed alongside. The DFT-GGA approach has proven to be very reliable for a wide range of applications and has served as a “workhorse” of quantum chemistry for the last twenty years.

However, GGAs still have the disadvantage of yielding only approximate exchange contributions, which result in certain problems expressing the exchange part of the energy [57]. A way to overcome these difficulties has been suggested by including a component of the exact exchange energy calculated from Hartree-Fock theory. Functionals of this type are known as hybrid functionals [70] and have the following general form:

$$E_{\text{XC}}^{\text{Hybrid}} = cE_{\text{X}}^{\text{HF}} + (1 - c)E_{\text{X}}^{\text{DFT}} + E_{\text{C}}^{\text{DFT}}, \quad (2.23)$$

where the coefficient  $c$  defines the HF exchange contribution. Especially successful hybrid functionals include the empirically-parametrized B3LYP [71] and parameter-free PBE0 [72].

In the present work most calculations have been carried out using the GGA-PBE functional. For comparison the target quantities were also systematically recomputed on the hybrid functional level with the PBE0 functional, without ever obtaining any qualitative changes that would conflict with the conclusions deduced from the standard PBE calculations. Considering the frequent observation that hybrid functional DFT yields results that for  $3d$  transition metal containing systems are at least en par, if not superior to correlated wavefunction approaches [73, 74, 75, 76], this supports the reliability of the herein reported results. The detailed discussion of the computational setup is given within the corresponding chapters. Of course, going beyond the accuracy of GGAs and hybrids is tempting, but more accurate electronic structure theory proves to be extremely computationally challenging when a large number of evaluations is required like in the context of global geometry optimization.

### 2.3 Numerical Atom-Centered Basis Sets

The set of functions that constitutes the molecular orbitals is called a basis set. Each orbital is described as a linear combination of basis functions according to eq. (2.12), where  $C_{\mu i}$  are coefficients and  $\psi_{\mu}$  are basis functions. For constructing MOs, several kinds of mathematical functions can be used as basis functions, *e.g.* atomic orbitals of hydrogen atom as in LCAO, Slater-type [77] orbitals, or analytically defined Gaussians [78]. The implementation of the all-electron full-potential DFT-code **FHI-aims** (Fritz-Haber-Institut *ab initio* molecular simulations) [79, 80], which was used for all ground-state calculations in this work, resorts to numerically defined atom-centered orbitals of



the form

$$\psi(\vec{r}) = \frac{u_i(r)}{r} Y_{lm}(\theta, \phi), \quad (2.24)$$

where  $Y_{lm}(\theta, \phi)$  are spherical harmonics. The radial part  $u_i(r)$  is numerically tabulated, thus being very flexible since any kind of desired shape can be achieved. This allows generating efficient species-dependent basis sets, which are constructed strictly hierarchical, so that the accuracy can be continuously increased up to meV level. By including the radial functions of occupied free-atom orbitals in the basis, the all-electron orbital shape and nodes near the deep nuclear  $Z/r$  potential are close to exact in bonded structures as well. Specifically, atom-centered orbitals are especially suitable for describing the cusp at the nucleus of a real AO, which makes them a good choice to treat systems containing transition metals. Together with a well-defined control of convergence, these advantages make the [FHI-aims](#) package a suitable tool for the calculations of  $M$ -doped Si clusters.

In [FHI-aims](#) the minimal basis of a species corresponds to the occupied orbitals of the effective Kohn-Sham potential of the corresponding non-polarized, spherically symmetric free atom. This basis thus facilitates the all-electron calculation since the oscillatory behaviour of the wavefunctions in the core-region are already well described at this level. Additionally the minimal basis avoids the atomic basis set superposition error (BSSE) [81] which can typically be observed for analytical localized basis sets.

The minimal basis set is further improved by additional classes of basis functions, one of which is formed by ion-like radial functions that are in particular suitable for describing a chemical bond as demonstrated by Delley [82]. These are states obtained from calculations of positive ions, which are supposed to describe the charge transfer of a system in a chemical bond. Hydrogen-like functions are used in addition, especially as polarization functions for angular momenta beyond those present in the free atom itself. These functions are derived from one-electron atoms with an arbitrary nuclear charge, that does not need to be an integer. Since radial functions originating from different potentials are not necessarily orthonormal to one another even on the same atomic site, all on-site radial functions are orthonormalized explicitly using a simple Gram-Schmidt process [83].

The different basis functions resulting from the basis set generation typically arise in groups of different angular momenta, *spd* or *spdf*, and are thus organized in so-called “tiers” [79] which contain a basis function of each angular momentum. The number of the “tier” thereby denotes the accuracy of the basis set.

All global geometry sampling calculations in this work are done with the “tier 2” basis set, which for instance contains 43 basis functions for Si, 67 basis functions for Ti and 88 basis functions for Cr. For the ensuing electronic structure analysis of the optimized geometries, the electron density was recomputed with an enlarged “tier 3” basis set which contains *e.g.* 64 basis functions for Si, 103 basis functions for Ti and 124 basis functions

for Cr. Several examples of basis sets used in the present work are given in detail in Appendix A.

## 2.4 Relativity with DFT

The hitherto discussed non-relativistic quantum-mechanical model is not suitable for describing systems containing heavy elements. Instead of the Schrödinger equation, in principle one has to solve the Dirac equation, which satisfies both the postulates of special relativity and those of quantum mechanics, and involves a four component Hamiltonian [84]:

$$\begin{pmatrix} v & c\boldsymbol{\sigma} \cdot \vec{p} \\ c\boldsymbol{\sigma} \cdot \vec{p} & -2c^2 + v \end{pmatrix} \begin{pmatrix} \psi \\ \chi \end{pmatrix} = \epsilon \begin{pmatrix} \psi \\ \chi \end{pmatrix}, \quad (2.25)$$

where  $\vec{p} = -i\nabla$  is the momentum operator,  $\boldsymbol{\sigma}$  is a vector of Pauli spin matrices, and  $\psi$  and  $\chi$  themselves have two components each.

However, since the dimension of the secular problem is very large, the requirements for integral evaluation time and data storage will be unfeasible. An attractive alternative is to transform the Dirac Hamiltonian to a form with less components. Several such formalisms have been developed and one of the most simple and elegant approaches is the zeroth-order regular approximation (ZORA) [85].

FHI-aims adopts a one-component, scalar-relativistic scheme [79], which in its most general form is found by solving one of the sub-equations of eq. (2.25) for  $\chi$  and then eliminating  $\chi$  from the other one. By neglecting spin-orbit coupling, one obtains:

$$\left( \vec{p} \cdot \frac{c^2}{2c^2 + \epsilon_i - v} \cdot \vec{p} + v \right) \psi_i = \epsilon_i \psi_i. \quad (2.26)$$

The scalar-relativistic Hamiltonian in eq. (2.26) is approximated as a whole, and then corrected by a subsequent perturbative treatment.

Self-consistent solutions of  $|\psi_i\rangle$  are obtained by using the ZORA kinetic energy operator:

$$\hat{t}_{\text{ZORA}} = \vec{p} \cdot \frac{c^2}{2c^2 - v} \cdot \vec{p}, \quad (2.27)$$

corresponding to  $|\epsilon_i| \ll 2c^2$ . After self-consistency is reached, each eigenvalue is rescaled using the “scaled ZORA” expression:

$$\epsilon_i^{\text{scaled}} = \frac{\epsilon_i^{\text{ZORA}}}{1 + \langle \psi_i | \vec{p} \frac{c^2}{(2c^2 - v)^2} \vec{p} | \psi_i \rangle}. \quad (2.28)$$

For total energies the sum of ZORA eigenvalues  $\epsilon_i^{\text{ZORA}}$  is then replaced with the sum of scaled ZORA eigenvalues  $\epsilon_i^{\text{scaled}}$ .

It has been shown [79] that the ZORA scheme gives good results when treating systems

with pronounced relativistic effects, for example small gold clusters.

## 2.5 Time-Dependent DFT

In order to explore optical properties of the transition metal doped silicon clusters, it is necessary, *e.g.* to calculate optical excitation spectra. A conventional, ground state density functional theory calculation can not provide the necessary information for this task. Instead, a theory capable of describing the excited states of the system is required. Several approaches for solving this problem have been suggested, ranging from a simple ground-state based  $\Delta$ SCF scheme [86] to more complicated and computationally costly configuration interaction (CI) [87] and multi-configurational self-consistent field methods, such as complete active space SCF (CASSCF) [88]. The most widely used approach nowadays is a time-dependent density functional theory (TD-DFT) [45] linear response formalism.<sup>2</sup>

In short, TD-DFT exploits the fact that the frequency dependent linear response of a finite system with respect to a time-dependent perturbation has discrete poles at the exact, correlated excitation energies of the unperturbed system [57]. The frequency dependent mean polarizability  $\alpha(\omega)$  describes the response of the dipole moment to a time-dependent electric field with frequency  $\omega(t)$ . It can be shown that the  $\alpha(\omega)$  are related to the electronic excitation spectrum according to

$$\alpha(\omega) = \sum_I \frac{f_I}{\omega_I^2 - \omega^2}, \quad (2.29)$$

where  $\omega_I$  is the excitation energy ( $E_I - E_0$ ),  $f_i$  are the corresponding oscillator strengths, and the sum runs over all excited states  $I$  of the system. Translated into the Kohn-Sham scheme, the exact linear response can be expressed as the linear density response of a non-interacting system to an effective perturbation. The formal foundation of TD-DFT is the Runge-Gross theorem [45] – the time-dependent analogue of the Hohenberg-Kohn theorem [43]. The Runge-Gross theorem shows that, under certain quite general conditions, there is a one-to-one correspondence between time-dependent one-body densities  $n(\vec{r}, t)$  and time-dependent one-body potentials  $v_{\text{ext}}(\vec{r}, t)$ , for a given initial state. This implies that the many-body wavefunction, depending upon  $3N$  variables, is equivalent to the density, which depends upon only three, and that all properties of a system can thus be determined from knowledge of the density alone. Then one can define a fictitious system of non-interacting electrons moving in a time-dependent effective potential:

$$i \frac{\partial \psi_j(\vec{r}, t)}{\partial t} = \left[ -\frac{\nabla^2}{2} + v_{\text{KS}}[n](\vec{r}, t) \right] \psi_j(\vec{r}, t), \quad (2.30)$$

---

<sup>2</sup>For a comprehensive discussion of all aspects of the current state of TD-DFT consult ref. [89].

whose density

$$n(\vec{r}, t) = \sum_{j=1}^N |\psi_j(\vec{r}, t)|^2 \quad (2.31)$$

is precisely that of the real system. This effective potential is known as the time-dependent Kohn-Sham potential [89]. After applying standard linear response theory [90, 91], it is possible to derive the central equation of the TD-DFT linear response:

$$\chi(\vec{r}, \vec{r}', \omega) = \chi_{\text{KS}}(\vec{r}, \vec{r}', \omega) + \int d^3r_1 \int d^3r_2 \chi_{\text{KS}}(\vec{r}, \vec{r}_1, \omega) \left( \frac{1}{|\vec{r}_1 - \vec{r}_2|} + f_{\text{XC}}(\vec{r}, \vec{r}_1, \omega) \right) \chi(\vec{r}_2, \vec{r}', \omega), \quad (2.32)$$

where all objects are functionals of the ground-state density. This equation is the key to electronic excitations within TD-DFT. When  $\omega$  matches a true transition frequency of the system, the response function  $\chi$  “blows up”, *i.e.* has a pole as a function of  $\omega$ . Likewise  $\chi_{\text{KS}}$  has a set of such poles at the single-particle excitations of the KS system.

In current implementations of TD-DFT the so-called adiabatic approximation [89] is employed, where the time-dependent exchange-correlation potential that occurs in the corresponding time-dependent Kohn-Sham equations is approximated as the functional derivative of a standard, time-independent  $E_{\text{XC}}$  with respect to charge density at time. It is worth emphasizing, however, that TD-DFT is not a simple extension of ground-state DFT. According to one of the developers of the theory, E. K. U. Gross [89], “it is an application of DFT philosophy to the world of driven systems, *i.e.* to the time-dependent Schrödinger equation, a first-order differential equation in time. Thus, while many of the statements look similar, the functionals themselves contain greatly different physics”.

In the present work a TD-DFT linear response formalism as implemented [46] in the `Gaussian 03` package [92, 93] is used to calculate excitation spectra of  $M$ -doped Si clusters.

## 2.6 Density Functional Based Tight Binding

The tight binding model [48] is an approach to the calculation of electronic band structure using an approximate set of wave functions based upon superposition of wave functions for isolated atoms located at each atomic site<sup>3</sup>. In the DFTB formalism the Kohn-Sham single-particle wavefunctions  $\psi_i$  are represented as LCAO:

$$\psi_i(\vec{r}) = \sum_v c_{vi} \psi_v(\vec{r} - \vec{R}_\alpha), \quad (2.33)$$

---

<sup>3</sup>An insightful overview of the DFTB capabilities and the theory behind it can be found in the ref. [94].

with the nuclei  $\alpha$  centered at  $\vec{R}_\alpha$ . The atomic orbitals  $\psi_\nu$  are determined by self-consistent calculations of the neutral atoms. Using this approach the Kohn-Sham equations can be transformed into a secular problem:

$$\sum_{\nu=1}^N c_{\nu i} (H_{\mu\nu} - \varepsilon_i S_{\mu\nu}) = 0; \quad \forall i, \mu \quad (2.34)$$

with the Hamiltonian matrix elements denoted by  $H_{\mu\nu}$  (Kohn-Sham matrix) and the non-orthogonal overlap matrix elements by  $S_{\mu\nu}$ :

$$S_{\mu\nu} = \langle \psi_\mu | \psi_\nu \rangle; \quad H_{\mu\nu} = \langle \psi_\mu | \hat{T} + V_{\text{eff}}(\vec{r}) | \psi_\nu \rangle . \quad (2.35)$$

To achieve a two-center representation for the Hamiltonian matrix elements, the non-self-consistent effective potential  $V_{\text{eff}}(\vec{r})$  is formally decomposed into atomic-like contributions, *i.e.* superposition of potentials of neutral pseudo-atoms [47].

The solution of the Kohn-Sham equations in the form of the secular problem (eq. 2.34) results in approximate molecular orbitals  $\psi(\vec{r})$  and therefore the density  $\rho(\vec{r})$  of the system under consideration. From these equations, the total energy  $E_{\text{tot}}$  and the forces of the system  $\vec{F}_\alpha$  acting on a nucleus  $\alpha$  can be obtained by introducing repulsive pair potentials.

The name ‘‘tight binding’’ of this electronic band structure model suggests that this quantum mechanical model describes the properties of tightly bound electrons in solids. The electrons in this model should be tightly bound to the atom to which they belong and they should have limited interaction with states and potentials on surrounding atoms of the solid. As a result the wave function of the electron will be rather similar to the atomic orbital of the free atom it belongs to. The energy of the electron will also be rather close to the ionization energy of the electron in the free atom or ion because the interaction with potentials and states on neighboring atoms is limited.

In the non-self-consistent DFTB scheme, first the pseudo atomic wavefunctions and the effective potential are calculated in the representation of Slater type orbitals [77]. Once these values are calculated, the integrals (2.35) are computed and tabulated as functions of the distance between the two atomic centers for an adequately dense grid of nodes. These tables are the so-called Slater-Koster tables [95].

In this work, one of the major codes providing the DFTB method, DFTB+ [96] has been used for the computationally costly global pre-sampling of the clusters adsorbed on a surface.

### 3 Exploring the Configurational Space of Clusters

One of the largest problems of studying clusters is finding the geometry of the most stable ground-state structure and also locating the geometries of the energetically low-lying isomers, that could be observed in experiments due to kinetic effects or finite temperatures. The main reason for the limited data about the geometry of clusters is a lack of direct experimental methods. Thus, applying theoretical approaches is necessary. Clusters possess rather complex potential energy surfaces, and since the PES is a function of  $3N-6$  atomic coordinates, prediction of geometries of large clusters is a challenging task. To describe and explore the potential energy surface, two problems have to be solved. First, a method that yields the total energy for a given atomic configuration is needed to accurately evaluate the PES. This information is obtained through the DFT framework, described in Chapter 2. Second, methods to sample the vast configurational space are needed, including local and global geometry optimization schemes [97]. This chapter is devoted to the most popular algorithms that provide this functionality.

#### 3.1 Local Geometry Optimization

Local geometry optimization requires a method that can bring the system into the next local potential energy surface minimum from any surrounding starting point, thus following the surface downhill according to some algorithm. Typically, local information such as the gradient (the first derivative of the function being minimized) or in some methods even the Hessian (the second derivative) are used to obtain the next structure.

The simplest approach, the *Steepest Descent* method [98], utilizes the fact that the gradient vector  $\nabla F(\vec{a})$  always points in the direction where the function increases most, therefore the function value can be lowered by stepping in the opposite direction:

$$\vec{b} = \vec{a} - \gamma \nabla F(\vec{a}) \quad , \quad (3.1)$$

where  $\gamma$  is a step width parameter. The main advantage of the steepest descent algorithm is that it typically always lowers the function value, provided that the step size is chosen well, thus being guaranteed to find a minimum. However, there are two main problems. First, two subsequent line searches are necessarily perpendicular to each other, which causes typical oscillations around the shortest path to the minimum. Therefore, the steepest descent algorithm tends to somewhat “spoil” the function lowering obtained by the previous step. Second, the rate of convergence always slows down as the minimum is approached. Usually the steepest descent is therefore used to quickly generate a better starting point before some of the more advanced algorithms are applied.

The *Conjugate Gradient* [99] scheme, consisting of successive line minimizations along a search direction, tries to improve on the “spoiling previous result” problem of the steep-

est descent method by performing each line search not along the current gradient, but along a line that is constructed in a way that it is conjugate to the previous search direction. In other words, the method “remembers” the information from previous searches, so that the new search does not destroy the progress of the previous one. The first step is equivalent to a steepest descent step, but subsequent searches are performed along a line formed as a mixture of the current negative gradient and the previous search direction:

$$\vec{c} = \vec{b} - \gamma \nabla F(\vec{b}) + \beta \vec{a}, \quad (3.2)$$

where  $\beta$  defines how much of the previous direction is to be taken into account. Therefore, the conjugate gradient scheme does not strictly follow the PES downhill, but along a search direction that is conjugate to the previous search directions. There are several ways of choosing the  $\beta$  value, such as the Fletcher-Reeves [100], Polak-Ribière [97] and Hestenes-Stiefel [101] approaches. Conjugate gradient methods typically have much better convergence than the steepest descent. However, for non-quadratic surfaces [97], the conjugate gradient does not hold rigorously, and must often be restarted (*i.e.*  $\beta$  should be set to zero) during the optimization.

The *Newton-Raphson* type of methods [102] expand the information needed about the current point  $\vec{a}$  to the second derivative (Hessian):

$$\vec{b} = \vec{a} + \nabla F(\vec{b} - \vec{a}) + \frac{1}{2} \nabla^2 F^2(\vec{b} - \vec{a}). \quad (3.3)$$

This Newton-Raphson formula is used iteratively for stepping towards a stationary point. Near a minimum all the Hessian eigenvalues are positive, and the step direction is opposite to the gradient direction. If, however, one of the Hessian eigenvalues is negative, the step in this direction will be along the gradient component, and thus will increase the function value. In this case, the optimization may end up at a saddle point, which can not occur in the steepest descent or conjugate gradient algorithms. Therefore, besides faster convergence, another advantage of the Newton-Raphson approach is the ability of locating saddle points, which is important for finding transition states in mechanistic studies. The main problems of the Newton-Raphson scheme are the complicated determination of the step size and its relatively high computational cost, since calculation of the full second derivative matrix is required, which must be stored and diagonalized.

The [FHI-aims](#) package used in this work employs the *Broyden-Fletcher-Goldfarb-Shanno* (BFGS) [103, 104] optimization method. The BFGS method is a quasi-Newton scheme that approximates Newton’s method and also uses the additional information in the form of the second derivative of the PES. Knowing an approximate form of the Hessian  $H$ , a new search direction  $\vec{b}$  can be obtained by solving a Newton-like equation:

$$H\vec{b} = -\nabla F(\vec{a}). \quad (3.4)$$

The next atomic configuration can then be obtained by performing a line minimization as in the conjugate gradient scheme (eq. 3.2). If the PES was perfectly harmonic and the Hessian known exactly, the local minimum would be found within one line search. In practice, however, the calculation of the Hessian matrix in each iteration step can be prohibitively expensive, so that it is instead successively approximated in each iteration step, therewith being a quasi-Newton scheme. Since more information of the PES is taken into account, the BFGS method can be more efficient than steepest descent or even conjugate gradient, but it works efficiently only if the system is close to the local minimum, where the harmonic approximation is justified. It is therefore typically recommended to start with a few steepest descent steps to bring the system close to the local minimum as in the case of the conjugate gradient scheme.

## 3.2 Global Geometry Optimization

All the methods mentioned above are designed to bring the system to the closest local minimum, located somewhere near the arbitrary starting point. In contrast, a truly global minimization should be able to find the global minimum irrespective of the starting point. Since local information is not enough to locate the global minimum, stochastic methods are required that provide some recipe to systematically sample the huge configurational space. Considering that the number of minima typically grows exponentially with the number of variables, the global optimization problem is an extremely difficult task for a multi-dimensional function, such as a PES of a cluster. Luckily, optimization problems are quite general in mathematics and physics [105, 106], and several methods of global geometry optimization have already been developed [107, 108] and successfully applied [109] to different chemistry-relevant systems, including silicon clusters [110]. Here a short summary of the most popular global optimization schemes is presented.

A first intuitive choice for an algorithm capable of overcoming barriers and thus exploring potential energy surfaces not only strictly downhill would be *Molecular Dynamics* [111] (MD) methods. Given a high enough energy, which is closely related to the simulation temperature in a canonical ensemble, the dynamics will sample the whole surface, but will also require extremely long simulation times, which makes the application of the method in general impractical.

A classical statistical mechanics global optimization algorithm applied to many fields is the *Simulated Annealing* [38] scheme based on the Metropolis algorithm [112]. Similar to MD, the method employs a system temperature as a guiding parameter for generating and accepting new geometries. A Monte-Carlo run is then initiated, during which the temperature is slowly reduced. Starting from an arbitrary configuration with a total energy  $E$ , a new structure is generated by randomly displacing the atoms in the so-called trial move, leading to a change of the total energy  $E$ . If the energy has decreased, *i.e.*



$\Delta E < 0$ , the new structure is accepted and used as starting point for the next step. In the opposite case, however, the structure is not discarded unconditionally, but accepted with a probability

$$P(\Delta E) = \exp\left(-\frac{\Delta E}{k_B T}\right). \quad (3.5)$$

At zero temperature, only isomers that are lower in energy would be accepted which would be an intuitive choice at first glance, since the system is thereby pushed towards the ground state. However, the system is then likely to get stuck in a local minimum. A finite temperature allows instead for controlled uphill steps, thus enabling the system to get out of local minima. The name, simulated annealing, comes from the analogy of growing crystals. If a melt is cooled slowly, large single crystals, representing a ground state, are formed. A rapid cooling produces a disordered solid, representing local minima, such as glass [97].

A further development of the simulated annealing idea has been implemented in the *basin-hopping* algorithm [40]. Additional to the trial move, a local structure relaxation is performed and the total energy of this local minimum is then assigned to the initial configuration. Therefore within this idea the configuration space is explored by performing consecutive jumps from one local PES minimum to another. The PES is therewith transformed into a set of interpenetrating staircases, known as “basins of attraction”, formed by all PES points whose local optimization paths lead to a certain local minimum:

$$\tilde{E}\{\vec{R}\} = \min E\{\vec{R}\}. \quad (3.6)$$

The most significant feature of this method is the allowance for the system to navigate between local minima, in particular, from a lower energy minimum to a higher one, enabling the system to hop among them. The basin-hopping algorithm has been shown to be very successful in dealing with complex systems ranging from clusters to biomolecules [113, 114], and demonstrated high efficiency for locating the geometries of small silicon clusters [41].

Obviously, there are many technical aspects that influence the performance of the global sampling technique. First of all, the initial geometry has to be chosen either randomly or guided by some sort of a chemical intuition based educated guess. Secondly, this geometry has to be disturbed in one or another way. For this, single-particle or collective moves, in which all atoms (collective move) or a randomly picked atom (single-particle move) is displaced in a random direction, can be chosen. The direction and the step size of the displacement is not *a priori* specified, and therefore, the displacement vector has to be chosen somehow and might even be optimized in the process of sampling. Besides the move class and displacement vector, the acceptance criterion, according to which a generated trial structure is accepted and then replaces the current structure as

### 3 Exploring the Configurational Space of Clusters

a new starting point, needs to be specified. For this, some kind of effective temperature  $T_{\text{eff}}$  should be chosen, which, on the one hand, would allow the system to overcome PES barriers, and, on the other hand, would eventually lead the system to the lowest lying PES areas in order to be able to find the ground-state structure. Then the basin-hopping acceptance rule based on the Metropolis algorithm [112] can be formulated like this:

$$P(\Delta E) = \exp\left(-\frac{\Delta\tilde{E}}{k_B T_{\text{eff}}}\right). \quad (3.7)$$

Finally, a method to perform local geometry optimizations and energy evaluations for the basin-hopping sampling has to be chosen.

Another popular type of global optimization schemes is represented by *Genetic Algorithms*, that take their idea and name from Darwin’s principle of the survival of the fittest [39, 115, 116]. Based on the principles of natural evolution, it uses operators that are analogues of the evolutionary processes of mating, mutation and natural selection to explore the configurational space. Instead of a single initial configuration used in simulated annealing or basin-hopping algorithms, here the starting point is a population of randomly generated cluster structures. New clusters are generated by choosing two candidate structures from the population (“parents”), which are then “mated” to create a “child”, allowing for “mutations” in the process. The best species from the population are selected based on Darwin’s principle, and carried on to the next “generation”, while the less suitable structures are discarded. Genetic algorithms have become popular recently due to ease of implementation [97] and have been applied for studying a wide range of clusters of different type, such as fullerenes, metal, ionic and molecular clusters [116].

A number of other algorithms has been suggested, such as the *Diffusion Methods*, where the energy surface is changed so that it will eventually contain only one minimum [117], or the *Distance Geometry Methods*, where the trial geometries can be generated from a set of lower and upper bounds on distances between all pairs of atoms [118]. Besides, many modifications of the basic types of global optimization schemes have been suggested, such as the *minima hopping* algorithm, where the random displacements are substituted by a molecular dynamics trajectory [119, 120], or the *landscape paving*, where the energy is artificially increased in regions that have already been explored [121].

In this work a basin-hopping implementation by Ralf Gehrke [41, 122] using the [FHI-aims](#) package as a “calculator” for local geometry optimizations has been used to sample the geometries of clusters, as well as a self-implemented version for optimizations of clusters on surfaces using the [DFTB+](#) package as a “calculator”.

## 4 Statistical Thermodynamics

In Chapter 2 the basic DFT machinery has been discussed, which provides a wealth of information about the electronic structure of the system under consideration as a function of its electronic density. Despite common belief, DFT is not merely a zero-temperature zero-pressure technique [123]. Instead, since the electronic density is itself a function of the atomic configuration, it provides complete information on the potential energy surface, which then contains the relevant information needed to describe the effect of temperature on the atomic positions.

In order to be able to discuss the influence of finite temperature and pressure, one needs to achieve a matching with thermodynamics. This idea is explored by *ab initio* atomistic thermodynamics, which employs the information of the first-principles potential energy surface to calculate appropriate thermodynamic functions, such as enthalpy, entropy or the Gibbs free energy [42, 124, 125, 126]. After getting the thermodynamic potential function in question, it is possible to evaluate macroscopic system properties using the standard methodology of thermodynamics [127, 128, 129].

Especially interesting for our clusters discussion is the Gibbs free energy, which under the defined conditions (temperature and pressure) is the appropriate thermodynamic potential to consider. Free energy per formula unit is equivalent to the chemical potential  $\mu$  in case of infinite, homogeneous system. In other words, if the homogeneous system is viewed as a reservoir,  $\mu$  gives the cost at which this reservoir provides particles. Then the cluster environment can be reduced to chemical potentials with which the cluster is in equilibrium. This then suggests a route to sample the ground-state geometries for a wide range of compositions and compare their relative stabilities for any given chemical potential. As a first step, obviously, we need a way to calculate the Gibbs free energy of the reference system to get information on the chemical potential of the atom in question. For this, we need to compute the so-called partition function, from which all thermodynamic values can be obtained. <sup>4</sup>

### 4.1 Partition Function

Assume that a thermodynamically large system is in constant thermal contact with the environment, with a temperature  $T$ , and both the volume of the system and the number of constituent particles are fixed. Such system is usually called a *canonical ensemble*. Then all possible states of such system can be described as:

$$Q = \sum_i e^{-\frac{E_i}{k_B T}}, \quad (4.1)$$

---

<sup>4</sup>For detailed discussion of Statistical Thermodynamics please refer to refs. [130] and [131].

## 4 Statistical Thermodynamics

where  $k_B$  is the Boltzmann constant and  $T$  is temperature. This expression is called *partition function* (denoting the partition of the ensemble into a set of systems) or the *sum over states* (referring to the summation over  $i$ ). The  $1/k_B T$  coefficient is often denoted as  $\beta$  and called Boltzmann factor. The partition function is obtained by summing Boltzmann factors over all states (or integrating over the phase space in case of the system with continuous energies). Thus,  $Q$  is obtained as a result of summing over all macroscopic states and is not a function of an individual state. Through  $Q$ , however, it is possible to connect macroscopic quantities with microscopic states [132].

The probability of finding the canonical ensemble system in one given energy state  $E_i$  is given by:

$$P_i = \frac{e^{-\beta E_i}}{Q} . \quad (4.2)$$

Gibbs first obtained the distribution function  $P_i$  given by eq. (4.2) by considering such an ensemble. Therefore, the method of deriving the distribution function for a canonical ensemble is called *Gibb's ensemble method*. Using the expression for  $P_i$ , we can evaluate canonical ensemble averages. For instance, the average energy is:

$$U = \sum_i \frac{E_i e^{-\beta E_i}}{Q} . \quad (4.3)$$

From here, the relations between statistical averages of observables and thermodynamic functions can be found. For example, eq. (4.3) can be obtained by differentiating  $\ln Q$  with respect to  $-\beta$ . Taking into account that  $Q$  is a function of temperature and total volume, we take a total derivative of  $k_B T \ln Q$ :

$$-d(k_B T \ln Q) = -k_B T \left( \frac{\partial \ln Q}{\partial T} + \frac{1}{T} \ln Q \right) dT - \frac{\partial(k_B T \ln Q)}{\partial V} dV . \quad (4.4)$$

At the same time, according to the second law of thermodynamics:

$$dU = T dS - p dV , \quad (4.5)$$

where  $U$  is the internal energy,  $S$  is the entropy, and  $p$  is the pressure. Thus, the Helmholtz energy is defined by:

$$F = U - TS , \quad (4.6)$$

which gives

$$dF = -S dT - p dV = - \left( \frac{U - F}{T} \right) dT - p dV . \quad (4.7)$$

Taking into account eq. (4.4), the average energy given by eq. (4.3) is:

$$U = - \left( \frac{\partial \ln Q}{\partial \beta} \right)_V = \left( \frac{\partial \ln Q}{\partial T} \right)_V k_B T^2 . \quad (4.8)$$

If we consider  $U$  as the thermodynamic internal energy, eq. (4.4) and eq. (4.7) become identical, giving

$$F = -k_B T \ln Q, \quad (4.9)$$

which is one of the fundamental equations of thermodynamics. Taking the same approach, one can show that, due to its important general statistical meaning, the partition function can be used to derive all other thermodynamic functions.

## 4.2 Getting Thermodynamic Functions From Molecular Data

As we have discussed above, all thermodynamic functions can be obtained through the partition function  $Q$ . In the general case, the total energy of a molecule (within the ideal gas approximation, suitable for calculating a finite gas phase environment of clusters) can be presented as a sum of at least four different contributions:

$$\varepsilon = \varepsilon_0 + \varepsilon_{\text{transl.}} + \varepsilon_{\text{rotat.}} + \varepsilon_{\text{vibrat.}} + \varepsilon_{\text{electr.}}, \quad (4.10)$$

where  $\varepsilon_0$  is the energy in the lowest energetical state. Within the Born-Oppenheimer approximation [50] all these contributions are considered to be independent of each other. Then the total partition function is

$$Q = Q_{\text{transl.}} + Q_{\text{rotat.}} + Q_{\text{vibrat.}} + Q_{\text{electr.}}. \quad (4.11)$$

The partition function can be used to express any thermodynamic function [133, 134].

The *translational* contribution to the partition function (within the ideal gas model) is described as:

$$Q_{\text{transl.}} = \frac{(2\pi k_B T m)^{3/2}}{h^3} \cdot \frac{k_B T}{p}. \quad (4.12)$$

Then the translational part of the Gibbs free energy per one mole of particles is:

$$G_{\text{transl.}} = -RT \ln \left( \frac{(2\pi k_B T m)^{3/2}}{h^3} \cdot \frac{k_B T}{p} \right) = -RT \ln Q. \quad (4.13)$$

For entropy:

$$S_{\text{transl.}} = R \ln \left( \frac{(2\pi k_B T m)^{3/2}}{h^3} \cdot \frac{k_B T}{p} \right) + \frac{5}{2}R = R \ln Q + \frac{5}{2}R. \quad (4.14)$$

For enthalpy and heat capacity:

$$H_{\text{transl.}} = \frac{5}{2}RT \quad C_p^{\text{transl.}} = \frac{5}{2}R. \quad (4.15)$$

As one can see from the equations above, only the mass of the molecule under consider-

## 4 Statistical Thermodynamics

ation, as well as the temperature and pressure are required to calculate the translational contribution to thermodynamic functions.

The *rotational* contribution to the partition function is usually computed within the rigid rotor approximation. For symmetrical molecules (*e.g.* a diatomic gas) the rotational partition function is:

$$Q_{\text{rotat.}} = \sum_{J=0}^{\infty} (2J+1) \exp\left(\frac{-J(J+1)\hbar^2}{2Ik_B T}\right), \quad (4.16)$$

where  $J$  is the rotational quantum number and  $I$  is the moment of inertia. The rotational constants can be computed from molecular data. For this, one first needs to calculate the product of the moments of inertia  $I_A I_B I_C$ :

$$I_A I_B I_C = I_{xx} I_{yy} I_{zz} - 2I_{xy} I_{xz} I_{yz} - I_{xx}^2 I_{yy} - I_{xy}^2 I_{zz} - I_{yz}^2 I_{zz}, \quad (4.17)$$

with individual products defined as

$$\begin{aligned} I_{xx} &= \sum_i m_i (y_i^2 + z_i^2); & I_{yy} &= \sum_i m_i (x_i^2 + z_i^2); & I_{zz} &= \sum_i m_i (x_i^2 + y_i^2); \\ I_{xy} &= \sum_i m_i x_i y_i; & I_{xz} &= \sum_i m_i x_i z_i; & I_{yz} &= \sum_i m_i y_i z_i \end{aligned}, \quad (4.18)$$

where  $m_i$  are atomic masses, and  $(x_i, y_i, z_i)$  are atomic coordinates. Then the rotational partition function is:

$$Q_{\text{rotat.}} = \frac{8\pi^2}{\sigma} \left(\frac{2\pi k_B T}{h^2}\right)^{3/2} \cdot (I_A I_B I_C)^{1/2}, \quad (4.19)$$

where  $\sigma$  is a classical symmetry number, indicating the number of indistinguishable orientations that the molecule can have. Then the rotational part of the Gibbs free energy per one mole of particles is:

$$G_{\text{rotat.}} = -RT \ln \left[ \frac{8\pi^2}{\sigma} \left(\frac{2\pi k_B T}{h^2}\right)^{3/2} \cdot (I_A I_B I_C)^{1/2} \right] = -RT \ln Q. \quad (4.20)$$

For entropy:

$$S_{\text{rotat.}} = R \ln \left[ \frac{8\pi^2}{\sigma} \left(\frac{2\pi k_B T}{h^2}\right)^{3/2} \cdot (I_A I_B I_C)^{1/2} \right] + \frac{3}{2}R = R \ln Q + \frac{3}{2}R. \quad (4.21)$$

For enthalpy and heat capacity:

$$H_{\text{rotat.}} = \frac{3}{2}RT \quad C_p^{\text{rotat.}} = \frac{3}{2}R. \quad (4.22)$$

As one can see from the equations above, only the coordinates of the atoms in the molecule under consideration, as well as the temperature and pressure are required to calculate the rotational contribution to thermodynamic functions.

The *vibrational* contribution to the partition function is obtained within the harmonic approximation by writing the partition function as a sum over the harmonic oscillators of all  $N$  fundamental modes  $\nu_i$  of the particle:

$$Q_{\text{vibr.}} = \sum_i^N \left[ 1 - \exp\left(\frac{-h\nu_i}{k_B T}\right) \right]^{-1}. \quad (4.23)$$

Then the vibrational part of the Gibbs free energy per one mole of particles is:

$$G_{\text{vibr.}} = RT \sum_i \ln \left[ 1 - \exp\left(\frac{-h\nu_i}{k_B T}\right) \right], \quad (4.24)$$

or with the account of zero-point vibrations:

$$G_{\text{vibr.}} = E^{\text{ZPE}} + \Delta G_{\text{vibr}} = \sum_i \left\{ N_A \frac{h\nu_i}{2} + RT \ln \left[ 1 - \exp\left(\frac{-h\nu_i}{k_B T}\right) \right] \right\}, \quad (4.25)$$

where  $N_A$  is Avogadro's constant. Obviously, for evaluating the vibrational contribution, we need to compute the vibrational spectrum of the molecule under consideration. The expression for entropy is:

$$S_{\text{vibr.}} = R \sum_i \frac{h\nu_i}{k_B T} \left[ \exp\left(\frac{h\nu_i}{k_B T}\right) - 1 \right]^{-1} - R \sum_i \ln \left[ 1 - \exp\left(\frac{-h\nu_i}{k_B T}\right) \right]. \quad (4.26)$$

For enthalpy and heat capacity:

$$H_{\text{vibr.}} = \frac{R}{k_B} \sum_i \frac{h\nu_i}{\exp\left(\frac{h\nu_i}{k_B T}\right) - 1} \quad C_p^{\text{vibr.}} = R \sum_i \frac{\left(\frac{h\nu_i}{k_B T}\right)^2 \exp\left(\frac{h\nu_i}{k_B T}\right)}{\left[\left(\exp\left(\frac{h\nu_i}{k_B T}\right) - 1\right)\right]^2}. \quad (4.27)$$

For certain molecules (mostly organic) a part of the  $3N - 6$  intermolecular degrees of freedom appear not as vibrations, but instead as rotations, *e.g.* of the  $\text{CH}_3$  group around the single C–C bond. Such rotations do not break the bonds, and can lead to existence of rotational isomers (conformers), which can be distinguished experimentally. The difference between vibrations and rotations is small in case of steric or energetic constraints limiting the rotation. In other cases, however, if such limiting potential is low, the contribution of internal rotations to thermodynamic functions has to be taken into account. In case of Si clusters there are no internal rotations, therefore this type of motion is not that important for the present work.

Thus, with an electronic contribution to the free energy computed as total energy

## 4 Statistical Thermodynamics

of the structure, we have a complete machinery that allows us to calculate the total Gibbs free energy of a system under consideration. From here, standard thermodynamics approaches can be used, for example, to evaluate relative stabilities of different systems. A more detailed discussion on this topic regarding clusters is given in [Chapter 10](#).



Part II

# From Building Blocks to Functionalized Materials

The prevalence of silicon in the semiconductor industry has sparked great interest in silicon-based nanostructures that could act as building blocks for new easy-to-integrate and engineered materials. Endohedral doping appears as a remarkable avenue to tailor the intrinsic properties of silicon clusters [15, 16, 17, 18, 135]. In contrast to the compact and reactive structures caused by the preferable  $sp^3$  bonding in pure Si clusters [136, 137, 138, 139], the incorporation of even a single impurity atom can lead to the stabilization of otherwise unfavourable cage-like geometries [140, 141, 142, 143], such as saturated fullerenes and other polyhedral cage structures. As in clathrates [144] or carbon nanostructures [13], these cages with endohedral metal atoms then represent appealing symmetric and unreactive building blocks for novel cluster-assembled materials with engineered properties. For instance, such systems have shown potential as an intriguing novel nanoform of Si for *e.g.* optoelectronic device applications [18, 145].

Of course, it's a long way from creating doped Si cluster building blocks to assembling a material with fine-tuned properties. First of all, one would need to assess the stability of such endohedrally doped clusters, since there is no systematic recipe known in literature to predict which dopants and/or cluster sizes should be stable. For this, a comprehensive study of the stabilization mechanism and electronic manifold of the structure has to be carried out in order to understand the nature of the bonding within the cluster. This problem is addressed in Chapter 4, largely based on our published article [146].

The next step would be to find a way to tune the magnetic and optical properties of doped clusters, *i.e.* to suggest a strategy to conserve the high spin moment of the encapsulated transition metal. In order to achieve this, one has to make sure that there is no charge transfer from the endohedral metal to the surrounding Si cage. Taking into account the large number of Si dangling bonds caused by the preferable  $sp^3$  hybridized state of Si in such clusters, this seems to be an essential problem. Chapter 5, as well as our paper [147], is devoted to this discussion.

Finally, a central question for chemistry and material science is how to assemble individual building blocks into one material. A critical evaluation of synthetically feasible routes to polymerization is of vital importance for a theoretical study of new materials. In Chapter 6, supported by our recently published work [148], the possibility of using endohedrally doped Si cages as building blocks for constructing highly magnetic materials is systematically assessed.

# 5 Stabilization Mechanism of Endohedrally Doped Si Clusters

A prerequisite to a systematic synthesis of silicon cluster based materials are simple rules that rationalize which metal dopants stabilize cages and of which size. While this has been controversially discussed, one commonly agreed criterion for highly stable so-called “magic” clusters is geometric and electronic shell closure [16, 141, 142]. Here, the electronic manifold of a highly symmetric cage is viewed as states in a spherical potential, and particular stability is expected, if the electrons fill any one of the angular momentum shells, *i.e.*  $1s$  ( $2e^-$ ),  $1p$  ( $6e^-$ ),  $1d$  ( $10e^-$ ),  $1f$  ( $14e^-$ ),  $2s$  ( $2e^-$ ),  $1g$  ( $18e^-$ ),  $2p$  ( $6e^-$ ),  $2d$  ( $10e^-$ ) etc. [149].

For a 16 Si atom endohedral Frank-Kasper (FK) polyhedron [150, 151] “magicity” would hence be predicted for a dopant atom donating four valence electrons, as the resulting  $16 \times 4 + 4 = 68$  electrons achieve closure of the  $2d$  shell. Within this model the known high stability of  $\text{VSi}_{16}^+$  is thus naturally explained, if the nature of the bonding in the cluster is viewed in terms of a full formal charge transfer, *i.e.* “ $\text{VSi}_{16}^+ = \text{V}^{5+} + \text{Si}_{16}^{4-}$ ” [27, 143, 152]. Recently, however, Lau *et al.* deduced from their X-ray absorption spectroscopy data that also  $\text{TiSi}_{16}^+$  and  $\text{CrSi}_{16}^+$  with one valence electron less and more, respectively, stabilize in a cage geometry, with furthermore a highly similar local electronic structure around the dopant atom compared to the classic  $\text{VSi}_{16}^+$  system [30]. These findings were a motivation of the investigation presented in this chapter as a first step of our theoretical study, which follows a twofold approach. First, we perform a first-principles global geometry optimization of the three cluster systems  $M\text{Si}_{16}^+$  ( $M = \text{Ti}, \text{V}, \text{Cr}$ ) to firmly establish that the endohedral FK cage indeed represents the ground state geometry for all three dopant atoms. Second, we analyze the obtained electronic structure to obtain a more qualified view on the nature of the chemical bonding and elucidate the mechanism that still stabilizes the cage despite the differing number of valence electrons in these three systems.

## 5.1 Computational Setup

All calculations presented within this chapter have been performed with the all-electron full-potential density functional theory (DFT) code **FHI-aims** [79, 80]. Electronic exchange and correlation was treated within the generalized-gradient approximation (GGA) functional due to Perdew, Burke and Ernzerhof (PBE) [69]. For comparison single-point calculations at the optimized PBE geometries were also performed on the hybrid functional level using the B3LYP [71] and PBE0 [72] functionals, without obtaining results that would lead to any conclusions different to the ones derived and presented below on the basis of the PBE data. This concerns in particular the energetic ordering of the

low-lying isomers and the electronic structure analysis.

**FHI-aims** employs basis sets consisting of atom-centered numerical orbitals (see Section 2.3). All sampling calculations are done with the “tier 2” basis set, which contains 43 basis functions for Si, 67 basis functions for Ti, 88 basis functions for V, and 88 basis functions for Cr, respectively. The numerical integrations have been performed with the “tight” settings, which correspond to integration grids with 85, 97, 99, and 101 radial shells for Si, Ti, V, and Cr, respectively, in which the number of integration points is successively decreased from 434 for the outermost shell to 50 for the innermost one [79]. For the ensuing electronic structure analysis of the optimized geometries the electron density was recomputed with an enlarged “tier 3” basis set, which contains 64 basis functions for Si, 103 basis functions for Ti, 115 basis functions for V and 124 basis functions for Cr (see Appendix A). Systematic convergence tests indicate that these settings are fully converged with respect to the target quantities (energetic difference of different isomers in the sampling runs; electron density distribution in the electronic structure analysis). This holds in particular for a central quantity of our analysis, the radial electron density distribution of the different doped cages. This quantity is defined as

$$n(r) = \int_0^{2\pi} \int_0^\pi r^2 n(r, \theta, \phi) \sin\theta \, d\theta d\phi, \quad (5.1)$$

where  $n(r, \theta, \phi)$  is the electron density at a given point at spherical coordinates  $(r, \theta, \phi)$  away from the central dopant atom at  $r = 0$ . To build a radial distribution of the electron density we calculate the surface integral (eq. (5.1)) for a set of spheres of increasing radii, and then plot the obtained values as a function of the sphere radius. The numerical integration is hereby performed using a cubic ( $400 \times 400 \times 400$ ) volumetric data grid with  $0.02 \text{ \AA}$  voxel width. The chosen finite integration radius and angle steps equal  $0.02 \text{ Bohr}$  and  $\pi/360$ , respectively.

Local structure optimization is done using the Broyden-Fletcher-Goldfarb-Shanno [103, 104] method relaxing all force components to smaller than  $10^{-2} \text{ eV/\AA}$ . To make sure that the cage-like geometry indeed represents the ground-state structure for all three dopant atoms we relied on basin-hopping (BH) based global geometry optimization [36, 40, 41] (for details on the method see Section 3.2). Within the BH idea the configuration space is explored by performing consecutive jumps from one local minimum of the potential energy surface (PES) to another. To achieve this, positions of atoms in the cluster are randomly perturbed in a so-called trial move followed by a local geometry optimization which brings the system again into a local PES minimum. A Metropolis-type acceptance rule is used to either accept or reject the jump into the PES minimum reached by the trial move. As specific BH implementation we chose collective as well as single-particle trial moves, in which all atoms (collective move) or a randomly picked atom (single-particle move) is displaced in a random direction. Two different starting

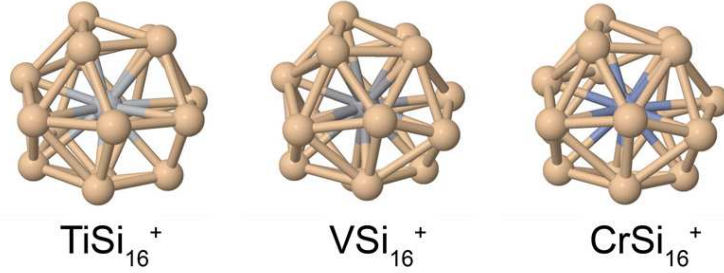


Figure 5.1: Ball-and-stick views of the identified ground-state FK cage geometries.

points were used for all optimization runs: 1) All atoms are randomly positioned inside a box of dimension  $(9 \times 9 \times 9) \text{ \AA}^3$ , or 2) the solution for the Thomson-problem [153] (how to put point charges on a sphere with minimal energy) is employed to position the Si atoms and then the doping metal atom is added at the center. Typical BH runs comprised of the order of 100 accepted trial moves, and unanimously identified the cage geometry as lowest energy structure regardless of the specific settings employed for the Metropolis rule [112] or the single-particle/collective moves.

## 5.2 Cage-like Ground State Geometry

In contrast to preceding work on  $\text{Si}_{20}$  fullerenes [154], our extended unbiased configuration searches confirm that the endohedral FK cage indeed represents the ground-state isomer for  $M\text{Si}_{16}^+$  with all three dopant atoms, *cf.* Fig. 5.1. The “non-magicity” in case of Ti and Cr doping only expresses itself in form of a much reduced energetic gap to the second lowest energy isomer identified in the BH runs: For  $\text{VSi}_{16}^+$  this gap amounts to 1.00 eV, whereas for  $\text{TiSi}_{16}^+$  and  $\text{CrSi}_{16}^+$  it is only 0.01 eV and 0.08 eV, respectively. Within a 1.00 eV range above the identified ground state we correspondingly found about 15 inequivalent isomers for the latter two systems. In the Cr-doped case all of them are capped  $\text{CrSi}_{15}^+$  cages, for Ti more compact  $\text{TiSi}_{16}^+$  cages are found within 0.1 eV above the ground state. Above this mostly capped  $\text{TiSi}_{15}^+$  structures are identified. For none of the three systems do we thus find exohedral structures among the energetically low-lying isomers. Detailed information about the structures of these lowest lying isomers can be found in Appendix B and ref. [146].

The incomplete shell-closure of  $\text{TiSi}_{16}^+$  and  $\text{CrSi}_{16}^+$  also shows up in the symmetry of the FK cage. Whereas the “ideal”  $\text{VSi}_{16}^+$  cluster exhibits perfect  $T_d$  symmetry, the cages with Ti and Cr dopants only exhibit  $C_1$  symmetry. The distortions away from perfect  $T_d$  symmetry are, however, only minor, as can best be seen from the *M*-Si bond distances within the cage. In a perfect FK polyhedron these distances fall into two closely spaced shells: one with four Si atoms that form a perfect tetrahedron, and slightly beyond that another one with 12 Si atoms that are all equidistant from the encapsulated metal atom.

In the  $\text{VSi}_{16}^+$  cluster, these two shells are located at distances of 2.54 Å and 2.81 Å, respectively. In the less symmetric  $\text{TiSi}_{16}^+$  and  $\text{CrSi}_{16}^+$  geometries the distortions lift the degeneracies of the two shells and we instead find  $M$ -Si distances spread over a range of 2.64 Å to 2.86 Å for Ti and over a range of 2.50 Å to 3.35 Å for Cr, respectively. Overall this leads in case of Ti doping to a slightly increased average cage radius of 2.78 Å, compared to the average  $M$ -Si distance of 2.74 Å in both  $\text{VSi}_{16}^+$  and  $\text{CrSi}_{16}^+$ .

Overall, the geometric differences between the three cages are thus rather small. We furthermore verified that these differences have only insignificant effects with respect to the discussion of the electronic structure of the cage presented in the following. In fact, also the other low-lying endohedral isomers identified for the “non-magic” clusters exhibit (despite their somewhat larger geometric distortions) an electronic structure that differs only insignificantly with respect to the following analysis from the one obtained for the ground-state isomer. We keep this in mind and correspondingly base our analysis for all three doped and the empty cages on the symmetric ground-state geometry obtained for  $\text{VSi}_{16}^+$ , *i.e.* in all cases the geometry was kept as in  $\text{VSi}_{16}^+$  and only the electron density was each time self-consistently computed. This procedure facilitates the qualitative discussion of the nature of the bonding and of the concomitant charge redistribution as it allows to directly subtract the electron densities obtained for the different dopants and, because of the higher symmetry, makes the presentation of radial electron distributions averaged over the solid angle more meaningful.

### 5.3 Spherical Potential Model

The prevalent model to rationalize the stability of doped Si cage geometries is the spherical potential model [16, 140, 141, 142, 143, 149], which has been discussed in detail for the “magic”  $\text{VSi}_{16}^+$  cluster by Torres, Fernández and Balbás [143]. As a first step in our attempt to qualify the chemical bonding and stability in the “non-magic” FK clusters doped with Ti and Cr we first briefly recapitulate the essentials of this discussion. The spherical potential model exploits the near sphericity of the ideal FK polyhedron, which suggests to classify the electronic states in shells of a determined radial and angular momentum quantum number. The computed density of states (DOS) of  $\text{VSi}_{16}^+$  shown in Fig. 5.2(b) demonstrates that the Kohn-Sham states indeed group into the expected sequence ( $1s, 1p, 1d, 1f, 2s, 1g, 2p, 2d, 1h, \dots$ ), with the 68 valence electrons exactly achieving closure of the  $2d$  shell. Also more subtle features like the splitting into the different tetrahedral ( $T_d$ ) sub-groups are perfectly obeyed, *i.e.* the different shells are sub-divided as  $s(a_1), p(t_2), d(e + t_2), f(a_2 + t_1 + t_2), g(a_1 + e + t_1 + t_2), h(e + t_1 + 2t_2)$ . Bonding to the transition metal dopant is predominantly expected *via* the  $\pi$ -type orbitals with one radial node ( $2s, 2p, 2d$ ), with hybridization following an approximate  $l$ -selection rule, *i.e.* the dopant  $3d$  and  $4s$  valence orbitals mix with Si cage  $d$  and  $s$   $\pi$ -orbitals, respectively.

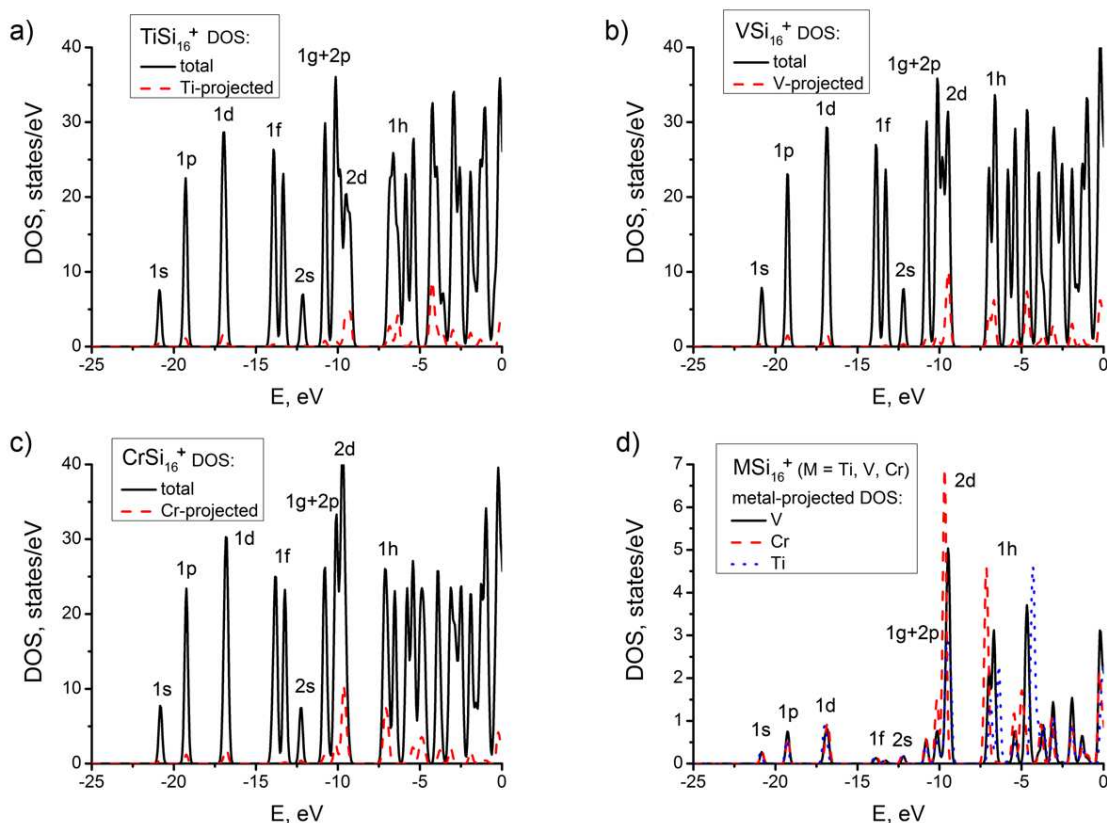


Figure 5.2: Total density of states (DOS) and DOS projected on the metal dopant for a)  $\text{TiSi}_{16}^+$ , b)  $\text{VSi}_{16}^+$ , and c)  $\text{CrSi}_{16}^+$ . Panel d) directly compares the metal-projected DOS for the three cases to illustrate the varying degree of metal-Si hybridization. The zero-reference for the energy scale is the vacuum level, and the labels given to the different groups of states follow the notation of the spherical potential model (see text).

The metal-projected DOS contained in Fig. 5.2(b) proves that also this feature of the spherical potential model is fully reproduced by the actual computation.

However, these features are not a specificity of the “magic”  $\text{VSi}_{16}^+$  cluster, but instead simply inherent properties of the near-spherical polyhedral cage shape. As apparent from Fig. 5.2(a) and 5.2(c) essentially the same groupings of the Kohn-Sham states are equally obtained for the other two dopants, *i.e.* also here the electronic manifold is well described within the spherical potential model. Exactly as expected from the differing number of valence electrons, the only difference is that electronic shell closure is not achieved. In  $\text{TiSi}_{16}^+$  (with 67 valence electrons) the highest energy state of the  $2d$  shell is unoccupied, and in  $\text{CrSi}_{16}^+$  (with 69 valence electrons) the lowest energy state of the  $1h$  shell is occupied. This lifts many of the degeneracies within the different electronic shells and leads to small inter-spin HOMO-LUMO gaps (see Tables 5.1 and 5.2), but the overall structure in terms of angular momentum shells is still preserved. Furthermore, as confirmed by our first-principles sampling calculations the endohedral FK polyhedron still represents the lowest-energy isomer for the “non-magic”  $\text{TiSi}_{16}^+$  and

| System                          | Spin    | HOMO, eV |       | LUMO, eV |       | gap, eV           |               |
|---------------------------------|---------|----------|-------|----------|-------|-------------------|---------------|
|                                 |         | alpha    | beta  | alpha    | beta  | same spin channel | by definition |
| TiSi <sub>16</sub> <sup>+</sup> | doublet | -9.01    | -9.28 | -7.12    | -8.69 | 1.89              | 0.32          |
| VSi <sub>16</sub> <sup>+</sup>  | singlet | -9.44    |       | -6.99    |       | 2.45              |               |
| CrSi <sub>16</sub> <sup>+</sup> | doublet | -7.90    | -9.17 | -7.16    | -7.26 | 1.91              | 0.64          |

Table 5.1:  $MSi_{16}^+$  ( $M = \text{Ti, V, Cr}$ ) HOMO and LUMO levels and HOMO-LUMO gap, computed both within the same spin channel and by definition.

CrSi<sub>16</sub><sup>+</sup>. Electronic shell closure might thus be a criterion for enhanced stability with respect to other potential isomers. However, it is not a necessary condition to stabilize the endohedral cage geometry *per se*.

## 5.4 Charge Transfer *vs.* Hybridization

Insight into the weakened role of electronic shell closure can come from a more qualified discussion of the nature of the chemical bond within the doped clusters. The simplified picture connected with the “magicity” of VSi<sub>16</sub><sup>+</sup> assumes a formal charge transfer of all five valence electrons to the Si cage manifold. This “formal” view is readily checked by evaluating the difference of the actually computed electron density of VSi<sub>16</sub><sup>+</sup> with respect to a mere superposition of the electron densities of an empty Si<sub>16</sub><sup>4-</sup> cage and a V<sup>5+</sup> cation. If the formal charge transfer picture was correct, then this electron density difference should be zero throughout. Figure 5.3 shows this difference in form of the radial electron density distribution, *i.e.* averaged over the solid angle, *cf.* eq. (5.1). The largely negative values exhibited at radii larger than the average cage radius of 2.74 Å indicate that a formally 4- charged Si cage would contain much more electron density at the outside as compared to the real VSi<sub>16</sub><sup>+</sup> system, while simultaneously there would be much less charge in the inside (positive regions in Fig. 5.3). However, this does not simply indicate that a smaller formal charge transfer from metal to cage takes place. As illustrated in Fig. 5.3 also other superpositions of differently charged empty cages and cations do not represent the real electron density well. This holds in particular for the radial region between  $\sim 1 - 2$  Å, *i.e.* exactly the bonding region between central metal atom and cage. The metal-Si bonding is thus rather the result of a more complex hybridization than mere formal charge transfer.

Equivalent results shown in Fig. 5.4 are also obtained for the “non-magic” TiSi<sub>16</sub><sup>+</sup> and CrSi<sub>16</sub><sup>+</sup> clusters, which means that also there the real electron density of the endohedral cage cannot be fully rationalized in terms of a formal charge transfer. However, in all three dopant cases the true electron density outside the cage is best represented,



| System                          | MO   | Spin channel |            |                                      |            |
|---------------------------------|------|--------------|------------|--------------------------------------|------------|
|                                 |      | Alpha        |            | Beta                                 |            |
|                                 |      | E, eV        | Isosurface | E, eV                                | Isosurface |
| TiSi <sub>16</sub> <sup>+</sup> | LUMO | -7.12        |            | -8.69                                |            |
|                                 | HOMO | -9.01        |            | -9.28                                |            |
| VSi <sub>16</sub> <sup>+</sup>  | LUMO | -6.99        |            | Singlet spin state:<br>same as alpha |            |
|                                 | HOMO | -9.44        |            |                                      |            |
| CrSi <sub>16</sub> <sup>+</sup> | LUMO | -7.16        |            | -7.26                                |            |
|                                 | HOMO | -7.90        |            | -9.17                                |            |

Table 5.2:  $MSi_{16}^+$  ( $M = \text{Ti, V, Cr}$ ) frontier orbitals.

*i.e.* the radial electron density difference distribution is closest to zero, for a charge combination of a positively charged Si cage and a neutral metal atom. This suggests that the different number of valence electrons in the three systems resides predominantly around the dopant. Figure 5.5 demonstrates that this is indeed the case. Depicted is the electron density difference between VSi<sub>16</sub><sup>+</sup> and TiSi<sub>16</sub><sup>+</sup>, as well as between VSi<sub>16</sub><sup>+</sup> and CrSi<sub>16</sub><sup>+</sup>, which allows to locate the missing electron in TiSi<sub>16</sub><sup>+</sup> and the excess electron of CrSi<sub>16</sub><sup>+</sup> as compared to the “magic” VSi<sub>16</sub><sup>+</sup> cluster, respectively. In both cases this is close to the central metal atom.

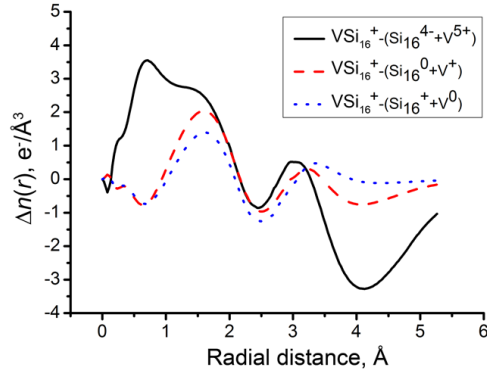


Figure 5.3: Radial distribution, *cf.* eq. (5.1), of the electron density difference,  $\Delta n(r) = n_{\text{VSi}_{16}^+}(r) - n_{\text{Si}_{16}^{4-}}(r) - n_{\text{V}^{5+}}(r)$  (black solid line), where  $n_{\text{VSi}_{16}^+}(r)$  is the electron density of the doped cage,  $n_{\text{Si}_{16}^{4-}}(r)$  the density of the empty Si cage, and  $n_{\text{V}^{5+}}(r)$  the density of the V cation. If the formal charge transfer picture was correct,  $\Delta n(r)$  should be essentially zero throughout. Note the average cage radius, *i.e.* the position of the Si atoms, is at 2.74  $\text{\AA}$ . Additionally shown are other charge combinations of the two fragments ( $\text{Si}_{16} + \text{V}^+$ , red dashed line;  $\text{Si}_{16}^+ + \text{V}$ , blue dotted line).

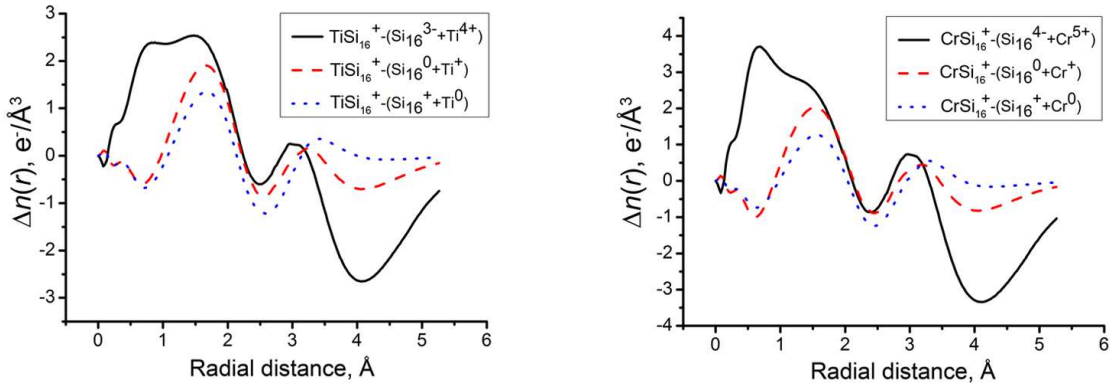


Figure 5.4: Same as Fig. 5.3, but for  $\text{TiSi}_{16}^+$  (left panel) and for  $\text{CrSi}_{16}^+$  (right panel).

A complementary view comes from the analysis of the projected DOS. For this Fig. 5.2(d) specifically compares the metal-projected DOS for the three doped cages. Interestingly, the metal contribution to the lower lying electronic shells up to the  $2p$  shell is essentially the same in all cases, *i.e.* the intra-shell bonding is little affected. This is much different for the frontier shells  $2d$  and  $1h$ , which are mostly responsible for the bonding between cage and dopant. Here, there is a clear trend of increasing metal weight to the states when going from  $\text{TiSi}_{16}^+$  over  $\text{VSi}_{16}^+$  to  $\text{CrSi}_{16}^+$ . If we add up these metal contributions over the occupied set of  $2d$  and  $1h$  states, we arrive at a total of 2.1 (Ti), 3.1 (V) and 3.7 (Cr) electrons in the three cases. Between Ti and V, as well as between V and Cr the metal dopant provides thus each time around one electron more to the hybridized states. The adapting degree of metal-Si hybridization hence compensates

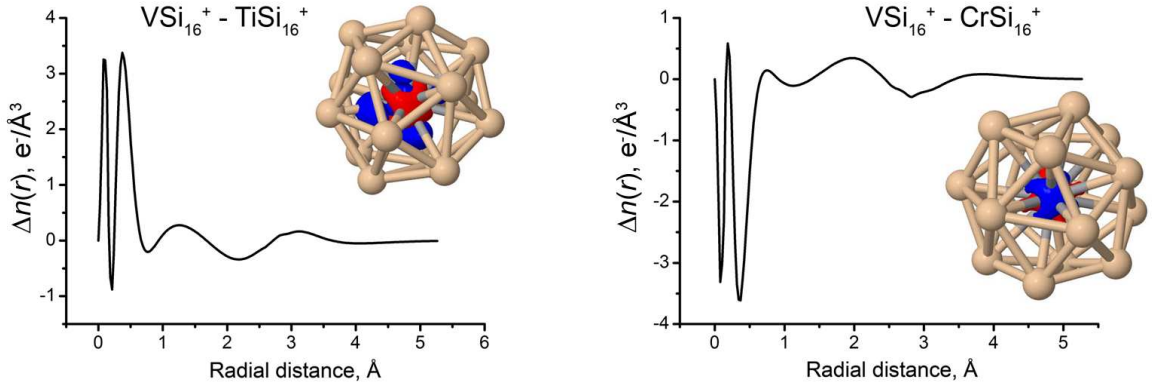


Figure 5.5: Electron density difference  $\text{VSi}_{16}^{+} - \text{TiSi}_{16}^{+}$  (left panel) and  $\text{VSi}_{16}^{+} - \text{CrSi}_{16}^{+}$  (right panel). The radial electron density distribution, *cf.* eq. (5.1), as well as the 3D isosurface at  $0.02 e/\text{\AA}^3$  in the inset demonstrate that the missing electron in the former and excess electron in the latter case are predominantly located around the central metal atom.

largely for the different total electron numbers. In other words, while from  $\text{TiSi}_{16}^{+}$  over  $\text{VSi}_{16}^{+}$  to  $\text{CrSi}_{16}^{+}$  there is each time one more valence electron in the topmost  $2d$  and  $1h$  shells, the number of electrons that is actually assigned to the Si cage remains essentially the same. The cage therefore effectively “sees” similar charge numbers, as the adaptive ability of the orbitals that are predominantly responsible for the metal-silicon bonding can accommodate for the charge excess or deficit. However, intriguingly it is not just one state that is responsible for this, *e.g.* intuitively the one with the changed occupation. Instead it is the rehybridization of the entire set of  $2d$  and  $1h$  states, which effectively compensates for the “non-magicity”. This adaptive capability diminishes the role of electronic shell closure and is in our view the main reason that helps to stabilize the endohedral cage geometry also for  $\text{TiSi}_{16}^{+}$  and  $\text{CrSi}_{16}^{+}$  despite their differing number of valence electrons.

## 5.5 Conclusions to Chapter 5

In summary our DFT-based unbiased configuration searches confirm the preceding interpretation of Lau *et al.* [30] that the Frank-Kasper polyhedron indeed represents the ground-state geometry for the series of doped  $\text{TiSi}_{16}^{+}$ ,  $\text{VSi}_{16}^{+}$  and  $\text{CrSi}_{16}^{+}$  clusters. Endohedral doping can thus be used as avenue to stabilize cage-like  $\text{Si}_{16}$  geometries. The electronic structure analysis demonstrates that all three systems are well described within the spherical potential model, *i.e.* the electronic manifold groups into states of defined radial and angular momentum number. Only the classic  $\text{VSi}_{16}^{+}$  cluster achieves closure of the electronic  $2d$  shell, while the varying number of valence electrons leads to an unoccupied  $2d$  state in case of  $\text{TiSi}_{16}^{+}$  and an occupied  $1h$  state in case of  $\text{CrSi}_{16}^{+}$ . Shell

closure is thus not a necessary condition for the stabilization of the cage-like geometry as ground-state structure.

We attribute this diminished role of shell closure for the stabilization to the adaptive capability of the metal-Si bonding, which is more the result of a complex hybridization than the mere formal charge transfer picture originally proposed in connection with the spherical potential model. This adaptive capability allows to locate the deficient electron in case of  $\text{TiSi}_{16}^+$ , as well as the excess electron in case of  $\text{CrSi}_{16}^+$  predominantly around the metal dopant. The effective charge assigned to the Si cage is then essentially the same in all three systems, *i.e.* the rehybridization of the  $2d$  and  $1h$  shells compensates for the “non-magicity”. This re-hybridization also causes a complete quenching of the dopant spin moment, which itself is thus a confirmation of the here suggested view.

While electronic shell closure is still certainly a criterion for particularly enhanced stability, the flexibility of the metal-Si bond can thus help to stabilize also other cage-dopant combinations than predicted by this simple rule. Enhanced stability here does not refer to other cluster sizes or dopants, but as confirmed by our global geometry optimizations to alternative, potentially exohedral isomers of the given doped cluster. If such an enhancement is a necessary criterion to maintain the structural integrity of the endohedral cage upon ligand bonding remains to be confirmed by future studies explicitly addressing the adsorption of such groups. Only if it is the case, it would make sense to transfer the concept of “magicity” — relating geometric stability to electronic shell closure — to the design of cluster-assembled materials.

## 6 Hydrogenated Si Fullerenes as Magnetic Building Blocks

As has been shown in Chapter 5, the cage geometry in endohedrally doped silicon clusters is stabilized through a strong interaction with the encapsulated dopant atom, which unfortunately goes hand in hand with a quenching of the dopant spin moment [146]. The recent suggestion that also hydrogen termination of Si clusters could yield an (empty) fullerene configuration [155, 156] has thus raised hopes that metal-doping of corresponding hydrogenated fullerenes would yield cage structures with minimized  $M$ -Si interaction [157]. With the atomic character of *e.g.* magnetic dopants then likely conserved, this would offer a route to specifically develop Si fullerene species with large magnetic moments for magneto-electronic applications.

In order to further explore and substantiate this idea, within this chapter we perform density functional theory based global geometry optimizations of the smallest hydrogenated endohedral cage,  $\text{Si}_{16}\text{H}_{16}$ , for a range of metal dopants. In order to address a possible influence of the size of the dopant atoms, this range comprises not only previously discussed high magnetic moment species like Ti or Cr [157], but extends over the entire  $3d$  series. While our extensive unbiased sampling indeed confirms the cage-like geometry as global ground state of empty  $\text{Si}_{16}\text{H}_{16}$ , this is unfortunately not the case for any of the  $3d$  dopants. Instead of a symmetric metal encapsulation, strongly distorted or even broken cages are significantly more stable in all cases. Moreover, the stronger  $M$ -Si interaction in these ground-state structures leads to the same quenching of the magnetic moment as in the regular  $M\text{Si}_{16}$  fullerenes. Attributing these discouraging findings to the insufficient space inside  $\text{Si}_{16}\text{H}_{16}$ , we therefore extend our study to the next larger fullerene-like structure,  $\text{Si}_{20}\text{H}_{20}$  [155]. Testing the high magnetic moment sequence Ti, V, Cr, and Co we now obtain in all cases perfectly symmetric endohedral cage geometries as ground states. Spin density distribution analysis furthermore reveals that the high spin states of these structures come indeed primarily from conservation of the dopant magnetic moment, *i.e.* the tested sequence already offers an intriguing toolbox of Si nanoforms with septet to quartet spin, respectively. Confirming also the next larger  $\text{Si}_{24}\text{H}_{24}$ ,  $\text{Si}_{26}\text{H}_{26}$  and  $\text{Si}_{28}\text{H}_{28}$  cages in the fullerene sequence as corresponding ground-state geometries, this strongly supports the idea of generating promising magnetic building blocks by doping sufficiently-sized hydrogenated Si cages.

### 6.1 $M\text{Si}_{16}\text{H}_{16}$ ( $M = 3d$ Metal) Clusters

The starting point of our investigation is an extended configurational search, which even after thousands of trial structures confirms that the ground-state structure of  $\text{Si}_{16}\text{H}_{16}$  is indeed the perfectly symmetrical tetrahedral ( $T_d$ ) cage shown in Fig. 6.1 [155]. Featuring

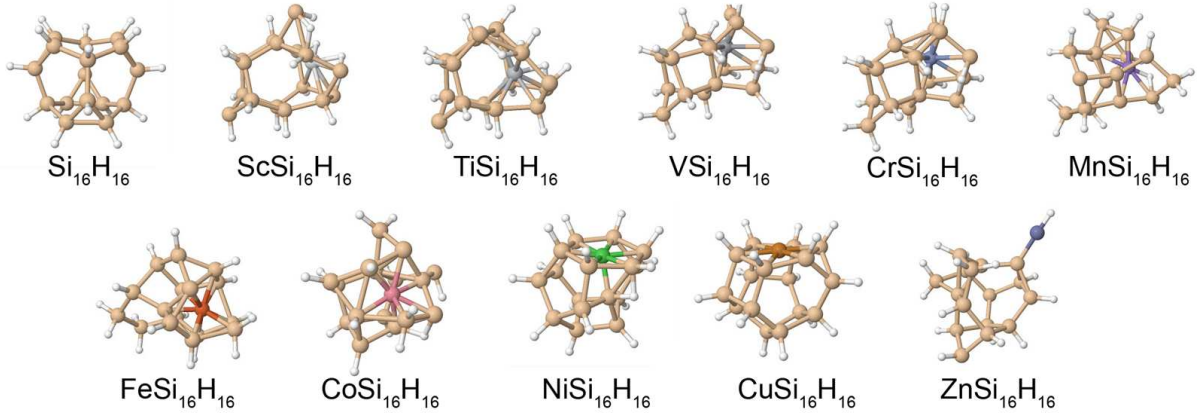


Figure 6.1: Identified ground-state geometry of  $\text{Si}_{16}\text{H}_{16}$ , as well as of  $M\text{Si}_{16}\text{H}_{16}$  clusters (with  $M$  covering the  $3d$  metal series).

Si atoms at distances of 2.95 Å and 3.17 Å from the center, this cage provides in principle enough geometric space to host an endohedral dopant atom, with the hydrogenation hoped to minimize the actual  $M$ -Si interaction. Unfortunately, the global geometry optimization results for  $M\text{Si}_{16}\text{H}_{16}$  clusters with metal dopant atoms ranging over the entire  $3d$  series from Sc to Zn reveal a different picture. In all cases only a few BH steps are required to identify significantly more stable geometries, which correspond to severely distorted cages or more compact structures that push the dopant atom from the center to the cluster fringe (or even expel it completely in case of Zn), *cf.* Fig. 6.1 (consult Appendix B or ref. [147] for detailed information about the structures and energetics of identified low-lying isomers). With the exception of Zn (0.37 eV) the energetic difference of these new structures to the symmetric endohedral cage is of the order of 1 eV or larger, which makes a kinetic trapping in the high-energy tetrahedral cage geometry rather unlikely. It also suggests that the obtained energetic order is not affected by the well-known limitations of the employed semi-local DFT functional. To further validate this, we nevertheless evaluated the energetic differences also with the hybrid PBE0 functional [72], without obtaining any qualitative changes.

As already indicated by the typically high Si coordination, the identified low-energy isomers exhibit a rather strong  $M$ -Si interaction involving substantial charge rearrangements. Not surprisingly, this goes along with an almost complete quench of the dopant spin moment. Clusters having an even number of electrons are singlets (Ti, Cr, Fe, Ni and Zn doping), clusters with odd number of electrons are doublets (Sc, V, Mn, Co and Cu doping), with again no changes observed when repeating the calculations at the PBE0 hybrid functional level. In case of the doublets, the unpaired electron is hereby not even necessarily centered on the dopant atom: For both Co and Sc the spin density is either partly or even mainly located on Si atoms, respectively. Obviously, this completely rules out the original proposition of using these clusters as highly magnetic Si building blocks.

|         | Ti                   |              | V            |              | Cr           |              | Co           |              |
|---------|----------------------|--------------|--------------|--------------|--------------|--------------|--------------|--------------|
|         | Relative, energy, eV |              |              |              |              |              |              |              |
|         | PBE                  | PBE0         | PBE          | PBE0         | PBE          | PBE0         | PBE          | PBE0         |
| singlet | 0.00                 | 0.00         |              |              | 0.00         | 0.00         |              |              |
| doublet |                      |              | 0.00         | 0.00         |              |              | 0.00         | 0.00         |
| triplet | -0.35                | -0.31        |              |              | -0.46        | -0.51        |              |              |
| quartet |                      |              | -0.67        | -0.86        |              |              | <b>-0.78</b> | <b>-0.69</b> |
| quintet | <b>-0.43</b>         | <b>-0.39</b> |              |              | -1.65        | -1.88        |              |              |
| sextet  |                      |              | <b>-1.23</b> | <b>-1.25</b> |              |              | 3.06         | 2.37         |
| septet  |                      |              |              |              | <b>-2.78</b> | <b>-3.09</b> |              |              |

Table 6.1: Calculated spin states (GGA-BPE and hybrid-PBE0) of Ti, V, Cr and Co atoms. Highlighted are the most stable spin states.

## 6.2 $MSi_{20}H_{20}$ ( $M = Co, Ti, V, Cr$ ) Clusters

Suspecting an insufficient space inside the cage as reason for these findings we proceed to the next larger hydrogenated fullerene-like cage  $Si_{20}H_{20}$ , for which extensive sampling again confirms the empty cage geometry shown in Fig. 6.2(a) as ground-state structure. Intriguingly, the increased radius of 3.33 Å of this icosahedral ( $I_h$ ) cage now seems to be large enough to even accommodate most space-demanding high spin-state dopant atoms. Focusing on the sequence Co, Ti, V, and Cr with quartet, quintet, sextet and septet atomic spin moments, respectively (see Table 6.1), the endohedrally-doped symmetric cage corresponds each time to the most stable structure found in our extensive sampling runs. Moreover, the energetic gap to the second lowest identified isomer, which then corresponds to a distorted or broken cage structure, is in all cases larger than  $\sim 0.5$  eV. From this we again do not suspect our findings to be jeopardized by the limitations of the employed semi-local DFT functional; an interpretation that we find confirmed by hybrid PBE0-level calculations that yield for all four dopant atoms the same energetic order of ground-state cage and second lowest isomer as in the PBE case.

Now, let's take a look at the electronic structure of the  $CrSi_{20}H_{20}$  cluster as an example of the doped hydrogenated silicon fullerene system. To locate the position of unpaired electrons we have plotted the spin density distribution of the cluster, in a form of both space-averaged radial distribution (zero corresponds to the center of the cage, *i.e.* the dopant atom) and a three-dimensional isosurface plot (Fig. 6.3(a)). Analysis of the spin density distribution confirms that the unpaired electrons indeed reside predominantly on the central metal atom. The area below the plot integrates to  $6.0 e^-$ , which corresponds to six unpaired electrons (septet state). The area under the first peak gives an estimation of the share of Cr dopant. This is in line with the obtained almost negligible hybridization

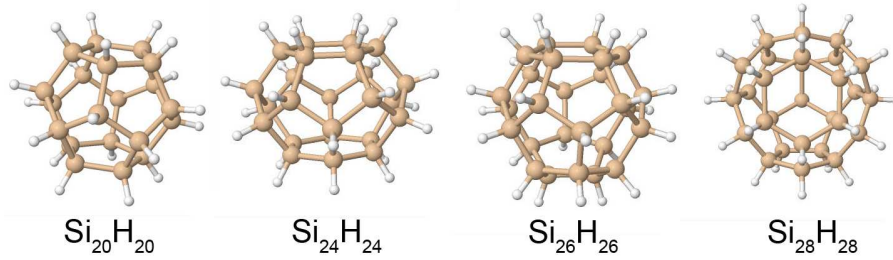


Figure 6.2: Identified hollow cage ground-state geometries of the next larger hydrogenated Si fullerenes.

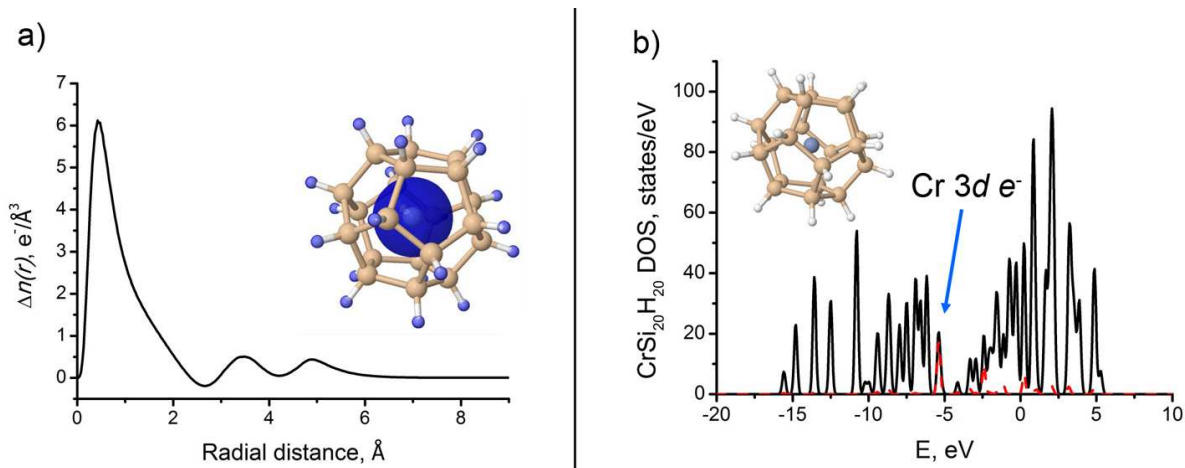


Figure 6.3: a) Radial spin density distribution of the  $\text{CrSi}_{20}\text{H}_{20}$  cluster. The inset shows the spin density distribution within the structure; b) Total DOS (black solid line) and DOS projected on metal dopants (red dashed line) for the  $\text{CrSi}_{20}\text{H}_{20}$  cluster.

of the occupied metal  $3d$  states. The Density of States (DOS) diagram of the  $\text{CrSi}_{20}\text{H}_{20}$  cluster, both total and dopant-projected, is presented in Fig. 6.3(b). The Cr-specific peak shows that five unpaired  $3d$  electrons belong almost exclusively to Cr atom. Thus, the atomic character of the dopant is largely preserved in the endohedral doped structure. A very similar picture is also observed for the other  $M\text{Si}_{20}\text{H}_{20}$  clusters considered. Thus, one can see that endohedral doping within the hydrogenated  $\text{Si}_{20}\text{H}_{20}$  cage allows conservation of the magnetic moments typical for the atomic states of the considered dopants.

For this fullerene size we thus find a beautiful confirmation of the hydrogenation concept, considering that previous global geometry optimization work clearly identified the corresponding endohedral  $M\text{Si}_{20}$  cages ( $M = \text{Ti}, \text{V}, \text{Cr}$ ) as metastable, with the ground-states of these unhydrogenated clusters instead given by heavily distorted and reactive structures [154]. In contrast to the again almost complete spin quench in the latter structures, the doped hydrogenated fullerenes furthermore perfectly conserve the high magnetic moments of their metal dopants, *i.e.*  $\text{CoSi}_{20}\text{H}_{20}$ ,  $\text{TiSi}_{20}\text{H}_{20}$ ,  $\text{VSi}_{20}\text{H}_{20}$ ,  $\text{CrSi}_{20}\text{H}_{20}$  exhibit quartet, quintet, sextet and septet spin moments, respectively. Analysis of the spin density distribution confirms that the unpaired electrons indeed reside predomi-



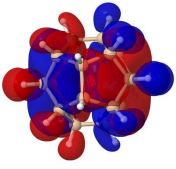
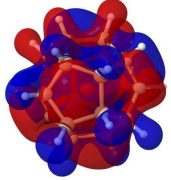
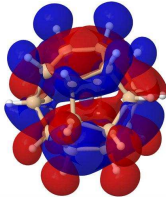
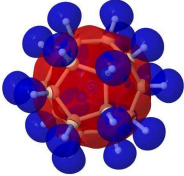
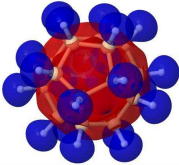
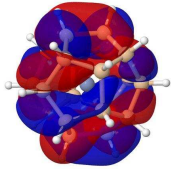
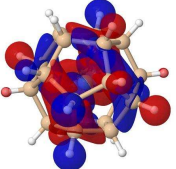
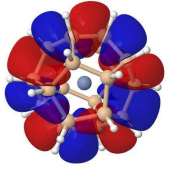
| System                          | MO     | Spin channel |  |       |  |
|---------------------------------|--------|--------------|--|-------|--|
|                                 |        | Alpha        |  | Beta  |  |
|                                 |        | E, eV        | Isosurface   | E, eV | Isosurface   |
| $\text{CrSi}_{20}\text{H}_{20}$ | LUMO+1 | -3.30        |   | -2.94 |   |
|                                 | LUMO   | -3.31        |   | -4.13 |   |
|                                 | HOMO   | -5.23        |   | -6.14 |   |
|                                 | HOMO-1 | -5.40        |  | -6.16 |  |

Table 6.2:  $\text{CrSi}_{20}\text{H}_{20}$  frontier orbitals.

nantly on the central metal atom, which is in line with the obtained almost negligible hybridization of the occupied metal  $3d$  states. The metal-cage interaction instead seems to be largely mediated *via* the metal  $4s$  state, which rationalizes the stabilization of a symmetric dopant position in the center of the cage. The high stability of the structures is reflected in rather high values of the HOMO-LUMO gaps (see Table 6.2 and 6.3).

Despite considerable binding energies, which at the PBE-level exceed 1 eV (see Table 6.3) and therewith stabilize the endohedral cage geometry, the atomic character of the metal dopant atom is thus largely conserved. Energies of the frontier orbitals in Table 6.3 are presented with respect to the vacuum (zero) level. For open-shell systems both alpha and beta spin channels are presented. Since the definition of the HOMO-LUMO gap for open-shell systems is somehow arbitrary, here we present two values: energy difference corresponding to the same spin channel orbitals and energy difference computed by definition (unoccupied orbital with the lowest energy minus occupied orbital with the

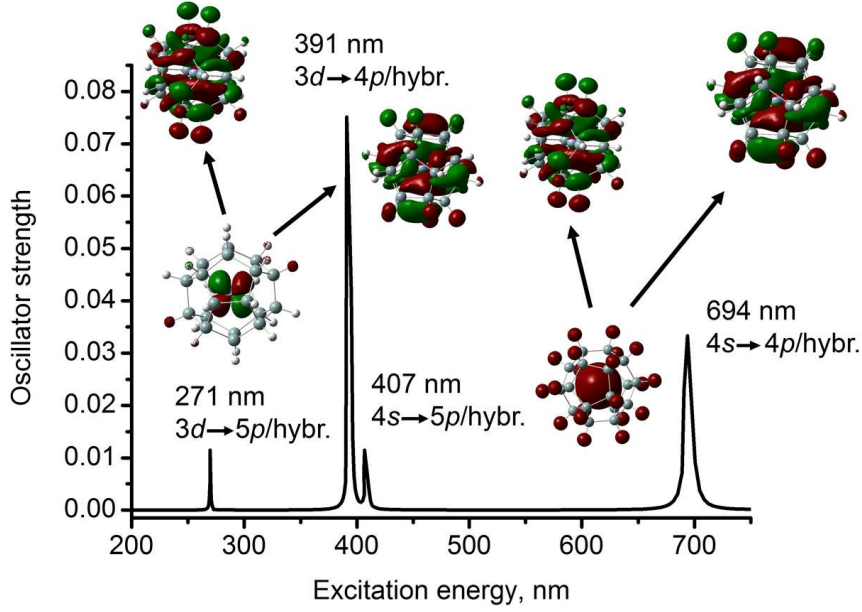


Figure 6.4: Calculated TD-DFT optical excitation spectrum of the endohedral  $\text{CrSi}_{20}\text{H}_{20}$  fullerene ground-state, with the insets illustrating the dominant Kohn-Sham orbitals behind the individual transitions.

highest energy). Binding energies are computed as follows:

$$E_b = E(\text{Si}_n\text{H}_n) + E(M) - E(M\text{Si}_n\text{H}_n), \quad (6.1)$$

where,  $E(M)$  is total energy of isolated dopant atom,  $E(\text{Si}_n\text{H}_n)$  and  $E(M\text{Si}_n\text{H}_n)$  are total energies of global minima of empty and doped hydrogenated silicon cage, respectively. One can see that systems with strong  $M$ -Si interaction ( $M\text{Si}_{16}\text{H}_{16}$ ) exhibit quenching of the dopant spin moments, as opposed to highly symmetric  $M\text{Si}_{20}\text{H}_{20}$  clusters with minimized  $M$ -Si interaction, featuring spin states of quartet, quintet, sextet and septet for Co, Ti, V and Cr, respectively. It is worth mentioning that strong-interacting systems are also characterized by typically higher binding energies towards the metal dopant. Comparing HOMO-LUMO gaps, one can come to the conclusion that all  $M\text{Si}_{16}\text{H}_{16}$  clusters show a smaller gap than the empty  $\text{Si}_{16}\text{H}_{16}$  cage, which can again be attributed to strong  $M$ -Si interaction, while highly symmetric  $M\text{Si}_{20}\text{H}_{20}$  systems with minimized dopant-cage interaction do not exhibit significant gap quenching.

The preserved atomic character of the metal dopant is also apparent in the optical excitation spectra, computed within the time-dependent density functional theory (TD-DFT) linear response formalism [45, 46] as implemented in the [Gaussian 03](#) suite [92]. To calculate the excitation spectrum of the cluster, the first one hundred transitions have been computed using the PBE0 [72] functional and the effective core potential double-zeta type LANL2DZ [158] basis set, which describes 28 core electrons with a pseudopotential and  $3s^2 3p^6 3d^{10} 4s^1$  electrons with a  $[5s, 5p, 5d/3s, 3p, 2d]$  valence basis

| System            | Spin    | HOMO, eV |       | LUMO, eV |       | gap, eV  |         | BE, eV |
|-------------------|---------|----------|-------|----------|-------|----------|---------|--------|
|                   |         | alpha    | beta  | alpha    | beta  | same ch. | by def. |        |
| $Si_{16}H_{16}$   | singlet | -5.46    |       | -3.05    |       | 2.40     |         | -      |
| $ScSi_{16}H_{16}$ | doublet | -4.91    | -5.18 | -3.81    | -4.03 | 1.10     | 0.89    | 4.17   |
| $TiSi_{16}H_{16}$ | singlet | -4.88    |       | -4.24    |       | 0.65     |         | 3.61   |
| $VSi_{16}H_{16}$  | doublet | -4.20    | -4.79 | -3.24    | -3.49 | 0.96     | 0.71    | 4.70   |
| $CrSi_{16}H_{16}$ | singlet | -4.66    |       | -3.43    |       | 1.23     |         | 3.38   |
| $MnSi_{16}H_{16}$ | doublet | -4.76    | -4.91 | -3.72    | -3.95 | 1.04     | 0.81    | 3.16   |
| $FeSi_{16}H_{16}$ | singlet | -4.54    |       | -3.12    |       | 1.42     |         | 5.24   |
| $CoSi_{16}H_{16}$ | doublet | -4.59    | -5.19 | -3.36    | -4.14 | 1.23     | 0.44    | 4.96   |
| $NiSi_{16}H_{16}$ | singlet | -4.92    |       | -3.10    |       | 1.82     |         | 6.28   |
| $CuSi_{16}H_{16}$ | doublet | -3.79    | -5.54 | -2.90    | -3.41 | 0.89     | 0.38    | 4.86   |
| $ZnSi_{16}H_{16}$ | singlet | -4.91    |       | -3.47    |       | 1.45     |         | 0.62   |
| $Si_{20}H_{20}$   | singlet | -6.15    |       | -3.26    |       | 2.89     |         | -      |
| $TiSi_{20}H_{20}$ | quintet | -4.21    | -6.14 | -3.68    | -4.03 | 2.11     | 0.18    | 1.87   |
| $VSi_{20}H_{20}$  | sextet  | -4.58    | -6.16 | -4.50    | -4.10 | 2.06     | 0.09    | 1.72   |
| $CrSi_{20}H_{20}$ | septet  | -5.23    | -6.14 | -3.31    | -4.13 | 1.92     | 1.09    | 1.42   |
| $CoSi_{20}H_{20}$ | quartet | -5.57    | -5.21 | -3.32    | -4.93 | 2.26     | 0.28    | 1.34   |
| $Si_{24}H_{24}$   | singlet | -6.02    |       | -3.23    |       | 2.79     |         | -      |
| $Si_{26}H_{26}$   | singlet | -6.08    |       | -3.24    |       | 2.83     |         | -      |
| $Si_{28}H_{28}$   | singlet | -6.19    |       | -3.25    |       | 2.94     |         | -      |

Table 6.3: Spin states, frontier orbitals energies, HOMO-LUMO gaps and binding energies for  $MSi_nH_n$  clusters. See text for details.

set. Figure 6.4 illustrates this for the  $CrSi_{20}H_{20}$  case. In stark contrast to corresponding spectra of *e.g.* the broken cage structures of  $MSi_{16}H_{16}$ , only a few well-defined transitions are apparent in the optical range. These transitions are energetically shifted and changed in their order in comparison to the corresponding spectra of the isolated atomic dopants. Nevertheless the “atomic” character is preserved, *i.e.* apart from their magnetic properties the endohedrally-doped hydrogenated fullerenes also exhibit promising optical properties.

We have also checked whether the symmetry of the dopant atom’s electronic configuration can influence the preferred  $Si_nH_n$  cage geometry and therefore size. For this, we have run global geometry optimization for  $MSi_{16}H_{16}$  and  $MSi_{20}H_{20}$  clusters encapsulating

several different  $f$ -elements. In all cases for  $MSi_{16}H_{16}$  the found ground-state structures correspond to highly distorted geometries, which agrees well with the results obtained for  $d$ -metal dopants.  $Si_{20}H_{20}$  cage is again found to be sufficiently large to accommodate the dopant atom, despite the increased atomic radius. For instance, we have found a perfectly symmetrical  $USi_{20}H_{20}$  cluster with a spin state of quintet, which agrees nicely with the dopant's electronic configuration  $5f^36d^17s^2$ .

### 6.3 Conclusions to Chapter 6

In summary, we have thus systematically scrutinized the possibility of stabilizing endohedrally doped Si fullerenes through hydrogenation. Our unbiased global geometry optimization based on semi-local and hybrid functional DFT undoubtedly revealed that the smallest hydrogenated  $Si_{16}H_{16}$  cage focused on in previous works is generally too small to encapsulate  $3d$  transition metals. On a conceptual level this underscores the danger of basing nanoscale materials design through predictive-quality theory on incomplete explorations of the vast configurational space, such as simple comparisons of chemically intuitive candidate structures. For the next larger fullerene-like cage though, our first-principles sampling indeed identifies perfectly symmetric  $MSi_{20}H_{20}$  ( $M = Co, Ti, V, Cr$ ) cage structures as ground states. Compared to distorted or broken cage geometries, these structures are stabilized through substantial delocalized  $4s$ -cage interaction, while nevertheless largely retaining the atomic character of the metal dopant. With respect to magnetic properties, the confirmed quartet, quintet, sextet and septet spin moments of  $CoSi_{20}H_{20}$ ,  $TiSi_{20}H_{20}$ ,  $VSi_{20}H_{20}$ , and  $CrSi_{20}H_{20}$ , respectively, thus already offer a nice toolbox of unreactive building blocks with high magnetic moments. Nicely shielded by the fullerene cage, the encapsulated dopants furthermore also conserve atom-like optical properties. This strongly suggests endohedral doping of hydrogenated fullerenes as a viable route to novel cluster-based materials for magneto-optic applications. This vision gets further support by extensive sampling runs that also suggest empty cage geometries as ground states for the next larger hydrogenated Si fullerenes up to  $Si_{28}H_{28}$ , *cf.* Fig. 6.2. Eventually, these cages will offer enough space to also host multi-core dopants. Encapsulation into hydrogenated Si fullerenes thus appears as a promising avenue to generally protect metal clusters from reactive environments and make their unique material's properties available in applications.

## 7 Assembling Functionalized Materials

As has been suggested in Chapter 6, especially interesting for magnetic applications is the case of hydrogenated metal-doped Si clusters, where a minimized cage-dopant interaction preserves the high magnetic moments of the encapsulated transition metal dopants [147, 155]. This discriminates such saturated structures from their non-hydrogenated counterparts, where the cage geometry is often stabilized through a strong cage-dopant interaction, which leads to quenching of the metal magnetic moment [146] (see Chapter 5). Without doubt, such highly-magnetic building blocks offer great potential for instance for data storage or spin-based electronic devices [159, 160].

Assembling the building blocks into one material structure is, of course, a key problem in chemistry and material science. The possibility of building homo- and heterogeneous aggregations of  $MSi_{16}$  clusters for different metal dopants  $M$  has been theoretically investigated by the groups of Balbás [20] and Nakajima [21]. Robles and Khanna reported that assemblies of  $CrSi_{12}$  clusters may have a net spin moment [161]. However, to the best of our knowledge, no study of potentially highly magnetic aggregates of hydrogenated endohedrally doped Si cages has been performed so far. The key question in this is how such saturated clusters can be assembled at all. As we have shown in the [previous](#) chapter,  $Si_{20}H_{20}$  is the smallest Si fullerene capable of conserving a high spin state of an encapsulated  $3d$  transition metal atom [147], with the H termination simultaneously ensuring total saturation of all Si dangling bonds, *cf.* Fig. 7.1(a). As opposed to this, non-hydrogenated  $MSi_{20}$  clusters do not form cage-like structures at all as the Si compensates for its undercoordination through strong  $M$ -Si interaction [154]. This suggests that a carefully reduced degree of hydrogenation (and, therefore, increased amount of unsaturated Si bonds) might be used to control the number of bonding sites offered by the cluster. As long as this does not jeopardize the structural integrity of the cage, such a strategy would lead to a toolbox of monomers with differing number of “docking sites”, that may offer the possibility to build network architectures of any morphology.

Scrutinizing this idea through quantitative first-principles calculations is the objective of this chapter dedicated to  $MSi_{20}H_{20}$  aggregates. The approach taken is as follows: First, we perform density-functional theory based global geometry optimizations for the prototypical high-spin  $CrSi_{20}H_{20}$  cage with different number of H vacancies introduced. This indeed validates the structural integrity of such “non-ideal” clusters. Second, we also use DFT-based global geometry optimization to show that particularly Si-Si doubly bridged dimers and trimers of these clusters actually represent most stable and highly magnetic ground-state configurations for a given Si/H composition. The energetics thus obtained finally allows us to discuss the thermodynamic feasibility of further polymerization of such clusters into one-dimensional chains, two-dimensional sheets or, eventually, more complicated three-dimensional structures.

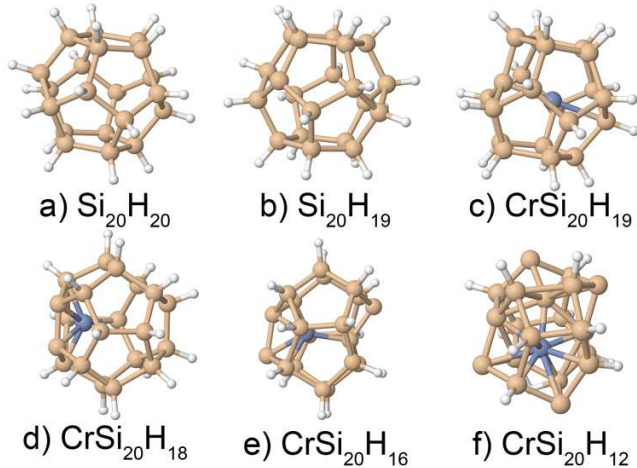


Figure 7.1: Identified ground-state geometries of possible monomer structures, together with their spin states and energies relative to their lowest-lying non-cage isomers: a)  $\text{Si}_{20}\text{H}_{20}$ , singlet,  $-3.96$  eV; b)  $\text{Si}_{20}\text{H}_{19}$ , doublet,  $-3.18$  eV; c)  $\text{CrSi}_{20}\text{H}_{19}$ , sextet,  $-1.23$  eV; d)  $\text{CrSi}_{20}\text{H}_{18}$ , singlet,  $-1.95$  eV; e)  $\text{CrSi}_{20}\text{H}_{16}$ , singlet,  $-0.80$  eV; f)  $\text{CrSi}_{20}\text{H}_{12}$ , singlet,  $-0.24$  eV.

## 7.1 Building Block Monomers

The starting point of our investigation is the check on the structural integrity of a  $M\text{Si}_{20}\text{H}_{20}$  building block, when introducing an increasing number of H vacancies to create undercoordinated reactive Si sites that would then represent natural “docking” candidates for aggregation. At the minimized  $M$ -Si interaction in the hydrogenated cage, we do not expect a strong dependence on the actual metal  $M$  used for doping [147]. This view receives support from test calculations with different metals, as well as from the fact that we obtain comparable findings also for the empty  $\text{Si}_{20}\text{H}_{20}$  cluster, which already by itself adopts a fullerene-type cage structure, *cf.* Fig. 7.1(a). Within the focus on magnetic properties, we therefore concentrate in the following on Cr as prototypical dopant atom, which we previously reported to yield the highest septet spin state in the  $\text{CrSi}_{20}\text{H}_{20}$  cage [147].

Extended configurational sampling shows that one hydrogen vacancy does not change the geometrical and electronic structure much, *i.e.* the identified  $\text{CrSi}_{20}\text{H}_{19}$  global minimum is still a (slightly distorted) cage, *cf.* Fig. 7.1(c), with a rather high sextet spin moment. In order to further analyze the  $M$ -Si interaction and the concomitant magnetic properties, Fig. 7.2 summarizes the total and Cr-projected density of states (DOS) of  $\text{CrSi}_{20}\text{H}_{19}$ . Consistent with the equally shown 3D spin density distribution this confirms that the unpaired electrons are predominantly located on the metal dopant, *i.e.* the latter preserves most of its atomic character as was the case for the ideal  $\text{CrSi}_{20}\text{H}_{20}$  cage [147].

The next lowest isomer found, which then corresponds to an irregular compact geometry, is 1.23 eV higher in energy. For the empty  $\text{Si}_{20}\text{H}_{19}$ , *cf.* Fig. 7.1(b), this energetic

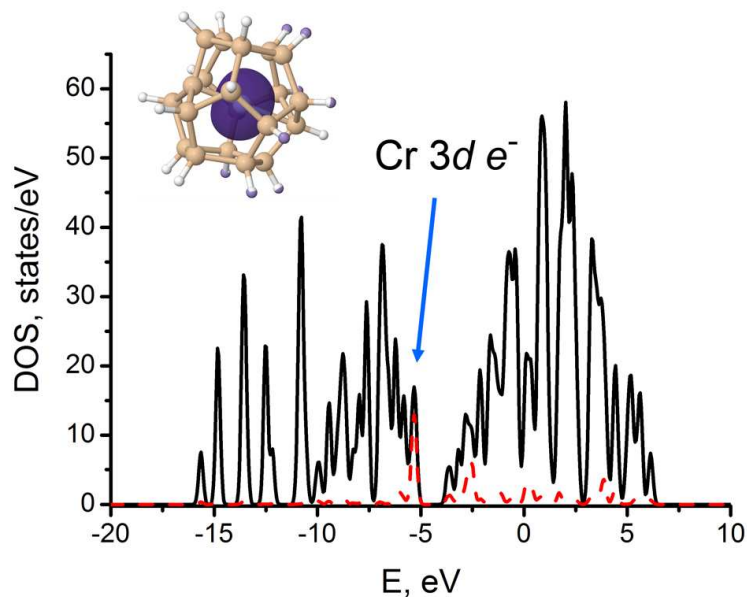


Figure 7.2: Total density of states (DOS) (black solid line) and DOS projected on the metal dopant (red dashed line) for  $\text{CrSi}_{20}\text{H}_{19}$  (highest occupied state lies at  $-5.23$  eV, vacuum level is used as zero reference). The Cr-specific peak (shown with arrow) indicates that five unpaired  $3d$  electrons belong almost exclusively to the Cr atom. The inset shows the spin density distribution within the cluster, which resides almost exclusively on the metal dopant.

gap to broken cage geometries even amounts to  $3.18$  eV. In both cases there is thus a clear thermodynamic preference for the endohedral cage, which demonstrates that the reduced hydrogenation has almost no effect on the structural integrity. What if we thus further increase the amount of H defects? Fig. 7.1(d) shows the identified ground-state structure for  $\text{CrSi}_{20}\text{H}_{18}$  corresponding to two H vacancies. Again, the cage-like geometry is preserved and the energetic gap to the lowest-lying non-cage-like isomer is with  $1.95$  eV quite pronounced. Still, what has changed is the position of the metal-dopant, which is now no longer more or less centered within the cage, but located close to the two dehydrogenated Si atoms. This indicates a stronger  $M$ -Si interaction of the type found for bare  $M\text{Si}_{20}$  cages. This perception is confirmed by a spin DOS analysis as the one in Fig. 7.2 and is also reflected in the spin-quenched singlet state of the  $\text{CrSi}_{20}\text{H}_{18}$  cage.

An intriguing feature that will become central for the aggregation discussed below is the obtained preference to locate the two H vacancies directly next to each other in the  $\text{CrSi}_{20}\text{H}_{18}$  structure. Energetically lowest-lying alternative arrangements with the two H vacancies *e.g.* located at opposite sides of the cage are by  $0.3 - 0.4$  eV less favorable than the paired-vacancy ground-state isomer. This structural motif intriguingly prevails if the number of H defects is further increased. Fig. 7.1(e) shows the identified ground-state geometry for the  $\text{CrSi}_{20}\text{H}_{16}$  cluster featuring a total of four hydrogen vacancies. Again, the H vacancies are paired and furthermore located at opposite ends of the cage. In

| System                             | Spin state | H <sub>2</sub> abstraction cost, eV |
|------------------------------------|------------|-------------------------------------|
| CrSi <sub>20</sub> H <sub>20</sub> | septet     | 1.92                                |
| CrSi <sub>20</sub> H <sub>18</sub> | singlet    | 1.25                                |
| CrSi <sub>20</sub> H <sub>16</sub> | singlet    | 0.47                                |

Table 7.1: Relative stability of the monomer clusters against dehydrogenation.

fact, despite substantial sampling, this was the only H arrangement we could identify that yields a stable cage-like geometry at all. All other energetically low-lying isomers found, which start above an energetic gap of 0.8 eV to the cage ground-state, correspond to irregular structures. Concomitant with the tendency to pair H vacancies, there is thus a tendency to arrange such H vacancy pairs as far away from each other as possible. Considering that an agglomeration of vacancies at one side of the cage is likely to break it up, the latter tendency is indirectly a consequence of the energetic stability of the cage, *i.e.* its resilience to alternative compact geometries. Quite nicely, these effectively repulsive interactions between H vacancy pairs then allow to accommodate an unusually high amount of H defects without jeopardizing the structural integrity of the cage. This is also reflected in the obtained ground-state geometry for the CrSi<sub>20</sub>H<sub>12</sub> cluster, *cf.* Fig. 7.1(f), which despite a total of eight H vacancies still maintains an (admittedly distorted, but still) endohedral geometry exhibiting four H vacancy pairs.

The energy cost to remove H<sub>2</sub> molecules from the suggested monomer structures follows the intuitive trend. It costs more energy to abstract an H<sub>2</sub> molecule from the perfectly symmetrical, totally saturated CrSi<sub>20</sub>H<sub>20</sub> cluster to form CrSi<sub>20</sub>H<sub>18</sub>, than it does to remove a second one from CrSi<sub>20</sub>H<sub>18</sub> to form CrSi<sub>20</sub>H<sub>16</sub>: 1.92 eV vs. 1.25 eV. The abstraction of the next two H<sub>2</sub> molecules to form a CrSi<sub>20</sub>H<sub>12</sub> cluster requires even less energy (0.47 eV per H<sub>2</sub> molecule). These data are summarized in Table 7.1.

## 7.2 Dimerization and Trimerization

The results of the [last](#) section reveal the prevalence of the cage-like geometry despite an increasing degree of dehydrogenation. One would expect the H vacancy sites formed at the CrSi<sub>20</sub>H<sub>20-n</sub> cages to then be natural candidates for aggregation, *i.e.* the docking sites to fuse clusters together. With just one H defect per cluster, the obtained CrSi<sub>20</sub>H<sub>19</sub> cage only allows for the formation of a dimer. However, the resulting dimer shown in Fig. 7.3(a) is with a computed binding energy of 0.15 eV only very weakly bound. Notwithstanding, the geometry shown is the end result of extensive sampling runs, *i.e.* it is the optimum structure found for a given composition of Cr<sub>2</sub>Si<sub>40</sub>H<sub>38</sub>. In particular, this means that the identified dimer is thermodynamically stable against decomposition into



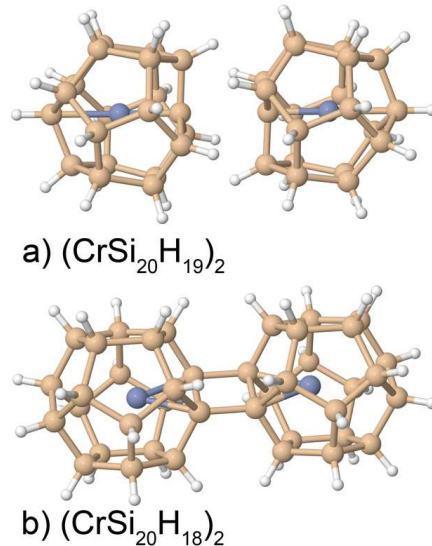


Figure 7.3: Identified ground-state geometries of cluster dimers: a)  $(\text{CrSi}_{20}\text{H}_{19})_2$ , ten unpaired electrons, 3.83 Å intermonomer distance and 0.15 eV binding energy; b)  $(\text{CrSi}_{20}\text{H}_{18})_2$ : twelve unpaired electrons, 2.42 Å intermonomer distance and 3.46 eV binding energy.

any smaller sub-units (under the constraint that in the present microcanonical sampling the total number of species in all sub-units together must equal  $\text{Cr}_2\text{Si}_{40}\text{H}_{38}$ ). Furthermore intriguing is the finding that the overall spin moment of the obtained dimer corresponds to ten unpaired electrons, *i.e.* we arrive at a highly magnetic structure.

As reflected in the 3.83 Å distance between the undercoordinated Si atoms in the two cages, we attribute the low binding energy particularly to steric constraints that prevent the two clusters from further approaching each other without H atoms coming uncomfortably close, *cf.* Fig. 7.3(a). This should be much alleviated for the H-vacancy pairs. Indeed, we obtain a significantly increased binding energy of 3.46 eV for the dimer formed by two  $\text{CrSi}_{20}\text{H}_{18}$  cages, which after extensive sampling again results as ground-state isomer with as large an energetic gap as 6.63 eV to the next low-lying structure. As apparent from Fig. 7.3(b), the intermonomer distance is concomitantly significantly decreased to 2.42 Å and therewith within the normal range found for Si-Si bonds. The resulting Si double-bridge type bonding between the two monomers has recently also been suggested by Nakajima and coworkers [21] as a favorable motif for the aggregation of smaller  $M\text{Si}_{16}$  clusters. In difference to these works, the appealing feature of the present structure is that it affords for a minimized *M*-Si interaction and yields a high magnetic moment of twelve unpaired electrons.

The analysis of the DOS diagram in Fig. 7.4(a) shows that the overall picture behind this high magnetization stays the same as discussed for the monomer  $\text{CrSi}_{20}\text{H}_{20}$  case before. The distribution of the spin density, inset in Fig. 7.4(a), further supports this view. Moreover, the optical excitation spectrum in Fig. 7.4(b), computed within the

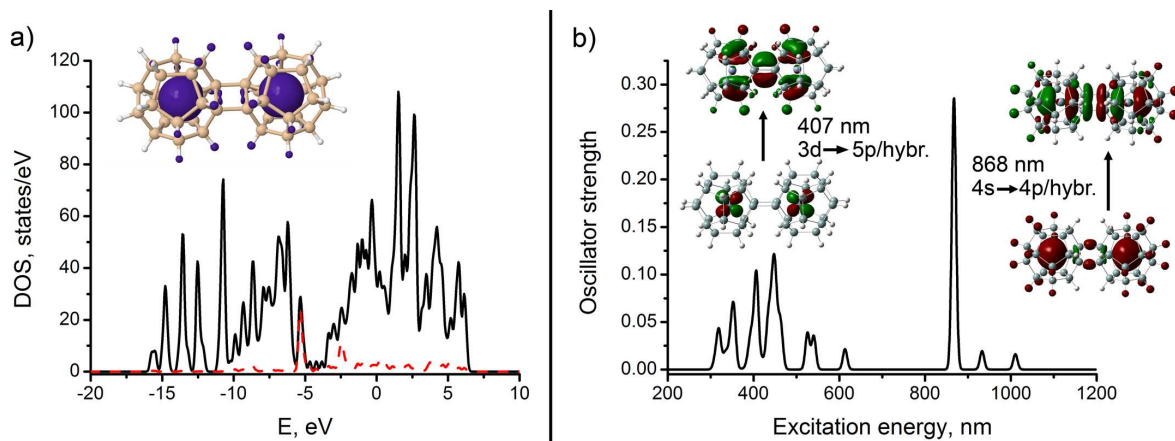


Figure 7.4: a) Total DOS (black solid line) and DOS projected on metal dopants (red dashed line) for the  $(\text{CrSi}_{20}\text{H}_{18})_2$  dimer (highest occupied state lies at  $-4.67$  eV, vacuum level is used as zero reference). The inset shows the spin density distribution within the structure; b) Calculated TD-DFT optical excitation spectrum of the  $(\text{CrSi}_{20}\text{H}_{18})_2$  dimer ground state, with the insets illustrating the dominant Kohn-Sham orbitals behind the characteristic Cr transitions.

time-dependent DFT (TD-DFT) linear response formalism, indicates that the optical properties of the  $(\text{CrSi}_{20}\text{H}_{18})_2$  dimer still have a lot in common with those of the  $\text{CrSi}_{20}\text{H}_{20}$  monomer, and even with an isolated Cr atom. Similar to the monomer case, several well-defined excitations from Cr  $4s$  and  $3d$  orbitals can be clearly discerned, where, due to the presence of two Cr atoms, intensities are just typically higher than in the case of the monomer, and some of the peaks are split.

Analysis of the dimer electronic structure shows that several bonding frontier orbitals have distinct  $p$ -character (*e.g.* LUMO in alpha spin channel, as well as several energetically close to it orbitals in beta spin channel). This, therefore, seems to suggest that the tendency of H vacancies to pair might be caused by the formation of intra-molecule Si-Si  $\pi$ -bonds that change into inter-molecular ones upon aggregation. However, the position of the dopant atom within the  $\text{CrSi}_{20}\text{H}_{18}$  monomer cage indicates strong interaction between Cr and Si, as is also reflected by the observed quenching of the spin moment (singlet *vs.* septet in  $\text{CrSi}_{20}\text{H}_{20}$  cluster with isolated Cr dopant located right in the center, as we have shown in [previous](#)) chapter. In many of the  $\text{CrSi}_{20}\text{H}_{18}$  frontier orbitals there is thus an evident contribution of the dopant, which supports an explanation of the reasons for the vacancies pairing along the lines of dopant-cage interaction. The information about the frontier orbitals of the  $\text{CrSi}_{20}\text{H}_{18}$  monomer and  $(\text{CrSi}_{20}\text{H}_{18})_2$  dimer is summarized in the [Tables 7.2](#) and [7.3](#), respectively.

Encouraged by these findings we have run a global geometry optimization of the linear  $[\text{CrSi}_{20}\text{H}_{16}](\text{CrSi}_{20}\text{H}_{18})_2$  trimer, which is at the edge of present-day computational capabilities. The resulting ground-state geometry is presented in [Fig. 7.5](#) and indeed corresponds to a highly symmetrical, doubly Si-Si bridge bonded trimer structure with a very high spin

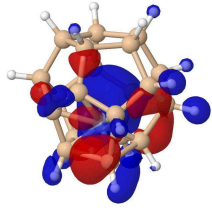
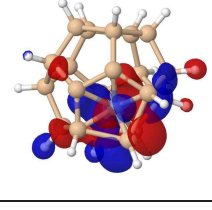
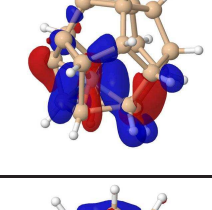
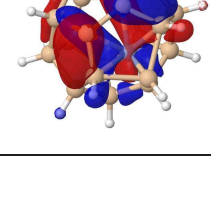
| System                             | MO     | MO energy, eV | Isosurface   |
|------------------------------------|--------|---------------|--|
| CrSi <sub>20</sub> H <sub>18</sub> | LUMO+1 | -3.73         |   |
|                                    | LUMO   | -3.86         |   |
|                                    | HOMO   | -4.70         |   |
|                                    | HOMO-1 | -4.75         |  |

Table 7.2: CrSi<sub>20</sub>H<sub>18</sub> monomer frontier orbitals.

moment of 18 unpaired electrons altogether, again located predominantly on the three Cr dopants. The energetic gap to the next low-lying isomer has increased to an incredible 7.16 eV. We stress again that as a result of extensive sampling this includes the stability against decomposition into any set of separated smaller clusters containing in sum the same number of species. For instance, we have explicitly evaluated by separate global geometry optimization of the smaller fragments that the obtained [CrSi<sub>20</sub>H<sub>16</sub>](CrSi<sub>20</sub>H<sub>18</sub>)<sub>2</sub> trimer is by 8.15 eV more stable than a set formed of two CrSi<sub>20</sub>H<sub>20</sub>, one CrSi<sub>8</sub> and one Si<sub>12</sub>H<sub>12</sub>, or by 9.03 eV more stable than a set formed of two CrSi<sub>20</sub>H<sub>20</sub>, one Si<sub>8</sub> and one CrSi<sub>12</sub>H<sub>12</sub>.

### 7.3 Routes to Polymerization

The dimerization and trimerization results indicate possibility of assembling very stable aggregates that largely conserve the magnetic properties of the dopant atoms. Involving cages with higher degree of dehydrogenation then opens up a pathway to more complicated network architectures, *e.g.* the CrSi<sub>20</sub>H<sub>12</sub> cage with four H vacancy pairs might be used for building two-dimensional sheets. Another important feature here is that the

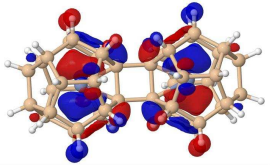
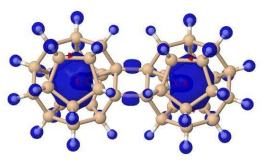
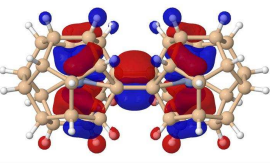
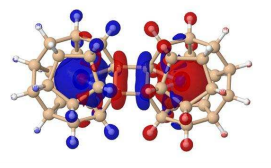
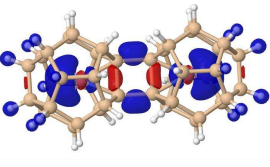
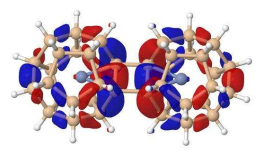
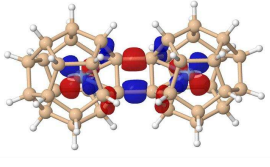
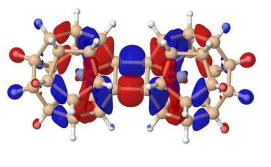
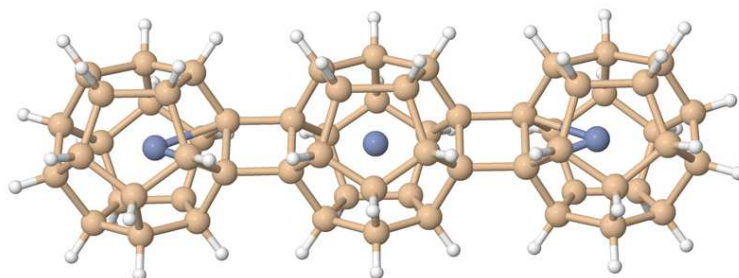
| System                              | MO     | Spin channel |   |       |   |
|-------------------------------------|--------|--------------|---|-------|---|
|                                     |        | Alpha        |   | Beta  |   |
|                                     |        | E, eV        | Isosurface  | E, eV | Isosurface  |
| $(\text{CrSi}_{20}\text{H}_{18})_2$ | LUMO+1 | -3.36        |    | -3.83 |    |
|                                     | LUMO   | -3.46        |    | -4.21 |    |
|                                     | HOMO   | -4.67        |    | -5.78 |    |
|                                     | HOMO-1 | -5.05        |  | -6.00 |  |

Table 7.3:  $(\text{CrSi}_{20}\text{H}_{18})_2$  dimer frontier orbitals.Figure 7.5: Ground-state geometry of the  $[\text{CrSi}_{20}\text{H}_{16}](\text{CrSi}_{20}\text{H}_{18})_2$  trimer, featuring 18 unpaired electrons.

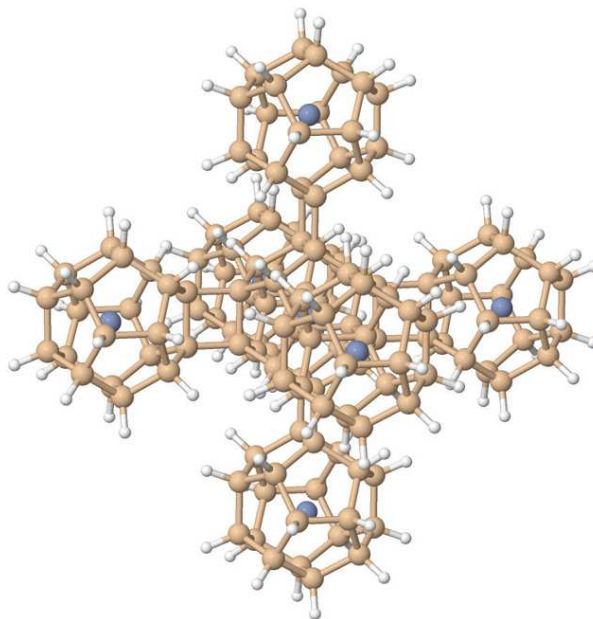


Figure 7.6: Locally optimized geometry of a  $[\text{CrSi}_{20}\text{H}_8](\text{CrSi}_{20}\text{H}_{18})_6$  doubly Si-Si bridge bonded 3D octahedral aggregate, exhibiting 42 unpaired electrons.

doubly-bridged Si bonding between the cages compensates for the H-vacancy pair induced Si undercoordination in the monomers. Whereas  $\text{CrSi}_{20}\text{H}_{20-2n}$  monomers with larger numbers of H vacancy pairs were found to keep their structural integrity, the increased  $M$ -Si interaction still led to a quenching of the dopant spin moment, *cf.* Fig. 7.1. In contrast, within the dimer and trimer structures the magnetic moment is re-established and contributes to the high total number of unpaired electrons. Indeed, consistent with this understanding we have managed to obtain the locally optimized  $[\text{CrSi}_{20}\text{H}_8](\text{CrSi}_{20}\text{H}_{18})_6$  doubly Si-Si bridge bonded 3D octahedral aggregate shown in Fig. 7.6 with the overall number of unpaired electrons reaching an impressive 42. At the implied reminimized  $M$ -Si cage interaction within the aggregates our findings should also not be specific to the Cr dopant used as showcase. In [previous](#) chapter we have established that dopants from the entire  $3d$  transition metal series yield  $M\text{Si}_{20}\text{H}_{20}$  cages as ground state isomers [147]. Correspondingly, we expect the here suggested dehydrogenation route to polymerization to hold for a wider range of in particular magnetic dopants, which would then offer a flexible toolbox to engineer electronic or magnetic properties in hetero-aggregates [21].

In our view crucial for a potential synthesis is the structural completion of the individual endohedral cages in the doubly-bridge bonded aggregates. In this respect, they are real cluster-assembled materials and thus differ qualitatively from known Si clathrates which are also composed of endohedral fullerene-like building blocks (*e.g.*  $M\text{Si}_{20}$ ,  $M\text{Si}_{24}$ ,  $M\text{Si}_{28}$ ). Elements of a typical Si clathrate usually share facets [162, 163, 164, 165], such that all Si valence bonds are saturated by surrounding Si atoms. They can thus not be separated into structurally complete fullerene monomers and represent rather a

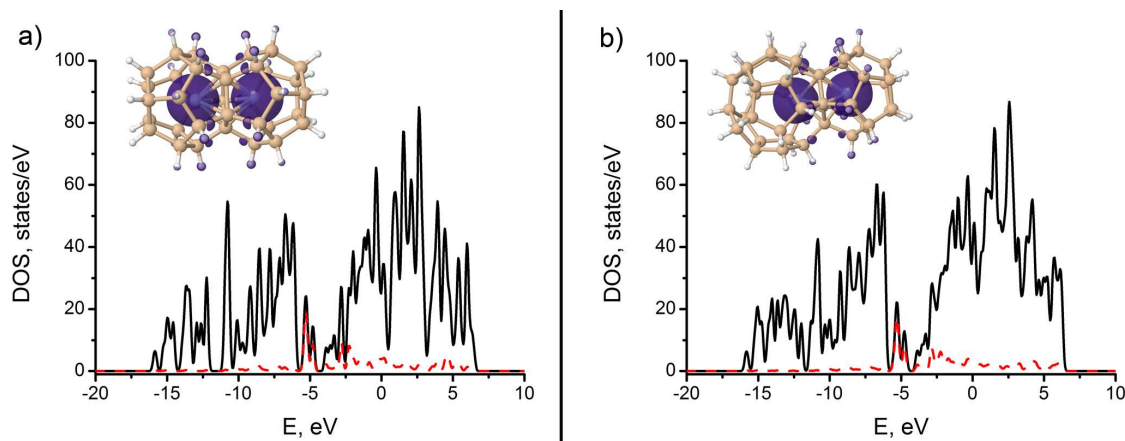


Figure 7.7: Total DOS (black solid line) and DOS projected on metal dopants (red dashed line) for a)  $\text{Cr}_2\text{Si}_{35}\text{H}_{30}$  cluster made of two  $\text{CrSi}_{20}\text{H}_{20}$  sharing facets; b)  $\text{Cr}_2\text{Si}_{43}\text{H}_{38}$  cluster made of one  $\text{CrSi}_{28}\text{H}_{28}$  and one  $\text{CrSi}_{20}\text{H}_{20}$  sharing a pentagonal facet. Insets show the spin density distribution within the corresponding structures.

space-filling framework than a cluster assembly at the molecular level.

To check if clathrate-like facets-sharing assemblies are possible in our case, we have constructed two dimer structures: a  $\text{Cr}_2\text{Si}_{35}\text{H}_{30}$  cluster made of two  $\text{CrSi}_{20}\text{H}_{20}$  cages sharing facets (to directly compare with our  $(\text{CrSi}_{20}\text{H}_{18})_2$  dimer), and a  $\text{Cr}_2\text{Si}_{43}\text{H}_{38}$  cluster made of one  $\text{CrSi}_{28}\text{H}_{28}$  and one  $\text{CrSi}_{20}\text{H}_{20}$  cluster sharing a pentagonal facet (as an example of a proper clathrate structure consisted of the elements of different size). Such a choice also allows to check whether different size of building blocks in clathrates is determined by purely geometrical reasons or there is an electronic structure argument behind it. Our global geometry optimization shows that in both cases the ground state structures are symmetrical clathrate-type dimers, which are 1.40 eV (in case of  $\text{Cr}_2\text{Si}_{35}\text{H}_{30}$ ) and 3.84 eV (in case of  $\text{Cr}_2\text{Si}_{43}\text{H}_{38}$ ) lower in energy compared to the corresponding next-lowest lying isomer (see insets in Fig. 7.7). The electronic structure analysis reveals that in both cases there are twelve unpaired electrons mostly located at Cr dopant atoms. DOS diagrams of these dimers (Fig. 7.7) also appear quite similar to the double-bridge dimer (Fig. 7.4). However, one can see that in case of clathrate-type dimers there is much smaller HOMO-LUMO gap, which can be explained by the closely bound facet-sharing geometry. Nevertheless, due to equivalent full saturation of Si dangling bonds, clathrate-type facets sharing can also be used as a route to build cluster aggregates.

This underlines the fact that a key to stabilization of cage-like cluster assemblies is full saturation of Si bonds. As long as all four Si valence bonds are saturated, there is no tendency for cage-dopant interaction, provided that, as we have shown previously [147], there is enough geometrical space to isolate a dopant. Therefore, both double-bridge binding and clathrate-type facets sharing can be used to construct highly magnetic materials. However, these possibilities are not equivalent from the point of view of practical

design and obtained material architecture.

In contrast to concomitant clathrate synthesis routes *via* annealing of bulk material, we thus rather expect polymerization strategies *via* controlled dehydrogenation of formed  $MSi_{20}H_{20}$  clusters to potentially realize the here suggested doubly Si-Si bridge bound aggregates. A central feature for this could be their very high stability, which renders *e.g.* a simple  $H_2$  abstraction reaction upon aggregation exothermic. For the dimer formation reaction  $CrSi_{20}H_{20} + CrSi_{20}H_{20} \rightarrow (CrSi_{20}H_{18})_2 + 2H_2$  we compute this as 0.35 eV (0.17 eV per formed  $H_2$ ) released upon aggregation, and similarly 0.14 eV per formed  $H_2$  for the abstraction of 4 or 12  $H_2$  molecules upon the formation of the trimer and 3D octahedral aggregate shown in Fig. 7.5 and Fig. 7.6, respectively. This suggests a range of hydrogen chemical potential to selectively dehydrogenate and build corresponding oligomers, for example in solution.

## 7.4 Conclusions to Chapter 7

In summary, we have systematically assessed the possibility of using endohedrally-doped hydrogenated Si-cages as building blocks for constructing highly magnetic materials. Our unbiased first-principles global geometry optimization highlights the structural integrity of the cage geometry of *e.g.* the  $CrSi_{20}H_{20}$  fullerene despite an increasing degree of dehydrogenation. The preferentially formed H-vacancy pairs then act as natural “docking sites” for polymerization. Depending on the amount of H-vacancy pairs of the involved monomers, this yields network architectures of any morphology, including linear chains, 2D sheets or 3D structures.

In contrast to face-sharing Si clathrates, the resulting aggregates represent real cluster assembled materials, in which structurally complete endohedral Si cages are doubly bridged through Si-Si bonds. The latter geometric motif yields a high thermodynamic stability and has also been observed in preceding work on smaller  $MSi_{16}$  clusters [20, 21]. For the present hydrogenated fullerenes, it affords a flexible and controllable molecular assembly, while maintaining the high magnetic moments of the dopant atoms inside the constituent cluster monomers. Taking into account the possibility to also stabilize larger cages (such as  $Si_{24}H_{24}$ ,  $Si_{26}H_{26}$ ,  $Si_{28}H_{28}$ ) and combining metal dopants having different spin states in hetero-aggregates, this strongly suggests such assemblies of hydrogenated endohedral Si-clusters as promising candidates for the construction of highly magnetic nanostructured materials.

Unlike in the case of carbon fullerenes, where  $sp^2$  bonding makes the aggregation of several cages improbable due to the concomitant necessity of breaking double bonds, synthetic control of the hydrogenation degree of Si cages by reducing the number of  $H_2$  molecules in the reactive environment seems to be quite feasible. This renders Si clusters not as just another possible building block composition that mimics the properties of

## 7 Assembling Functionalized Materials

carbon fullerenes, but rather as a new type of host cages, allowing for both isolation of the dopant from reactive environment and controllable building of extensive aggregates with engineered properties.



Part III

# Beyond the Scope of Conventional Cluster Science

## 8 Multi-Doped Si Cages: High Spin States Beyond the Septet Limit

Adding several different dopant atoms to the system appears to yield unique properties, unavailable for singly-doped clusters, such as large dipole [21] or magnetic [166] moments. Recent studies show high potential of complex molecular systems to be used in the rapidly growing field of molecular electronics, with the possibility of building conductive molecular junctions [167], charge separation layers for photovoltaic cells [168, 169, 170], p–n junctions to serve as transistors and emitting diodes [171]. To date, two main directions of the cluster multi-doping idea have been looked upon: either to form multiply doped systems by creating hetero-oligomers [18, 20, 21, 148, 172, 173] and even silicon nanorods [174, 175, 176] made of several singly-doped clusters, or to create truly multiply doped individual cages, accommodating several dopant atoms [13, 166, 177, 178] or even whole molecules [179, 180] within the same cavity. It has been shown that incorporation of magnetic ions within the cluster cage can lead to the formation of so-called single-molecule magnets with long relaxation times [166]. To the best of our knowledge, the latter idea has only been applied to carbon fullerene cages, being sufficiently large and stable to accommodate complex dopants. However, as we have shown in Chapter 6, hydrogenated Si clusters are also capable of forming large fullerene-like cages [147, 148, 155, 156, 157], which suggests the possibility of providing sufficient space to create multi-doped endohedral Si structures.

One of the first experimental steps towards Si cluster multi-doping has been reported by the groups of A. Fielicke and P. Lievens [29]. They demonstrated that the physisorption of Ar can act as a structural probe for transition metal doped silicon clusters, and is very sensitive to the position of the transition metal in the cluster. The experimental study shows that argon does not attach to elemental silicon, but instead only to surface-located transition metal atoms. Using this technique, “critical” sizes for Ar attachment to doubly doped clusters have been suggested. For instance,  $\text{Cr}_2\text{Si}_{16}^+$  has been predicted as a smallest doubly Cr-doped Si cluster (however, it should be noted that “endohedral” generally means that the dopant is surrounded by other atoms, not necessarily encapsulated within a symmetric cage-like structure). Several theoretical works have also been carried out on this topic. For example, Kumar and Kawazoe [155] suggested a double prism structure for  $\text{Cr}_2\text{Si}_{18}$ . Ji and Luo [181] studied  $M_2\text{Si}_{18}$  clusters for the whole range of  $3d$  metal dopants and found several symmetric geometries. However, although no systematic global PES sampling has been performed, no highly magnetic structures have been reported.

One of the exciting prospects of multi-doping within the same cluster cavity is the potentially increased magnetic moments of such complex dopants. While single-atom dopants are limited by the maximum number of five ( $d$ -shell) or six ( $s$  and  $d$ ) unpaired

electrons (*e.g.*  $4s^23d^5$  or  $4s^13d^5$  configurations of Mn and Cr, among the  $3d$  series), complex dopants open a path for larger spin moments. For instance, T. Lau *et al.* have reported X-ray absorption spectroscopy evidence for the localized character of the valence electrons in  $\text{Cr}_2^+$ ,  $\text{Mn}_2^+$ , and  $\text{CrMn}^+$  dimer cations [182]. With bonding predominantly mediated by  $4s$  electrons, these transition-metal dimers exhibit local high spin states with up to  $5 \mu_B$  spin moment of the  $3d$  electrons at each metal core. If such dopants can preserve their unique properties when encapsulated within the Si cage, it might be a way to bring these properties to cluster-assembled materials, for example by constructing doubly Si-Si bound aggregates, as was discussed in Chapter 7.

In order to systematically assess the possibility of multi-doping of Si clusters, we here again apply density functional theory based global geometry optimization to validate the idea of stabilizing symmetric structures with high magnetic moments within the smallest possible hydrogenated  $M_2\text{Si}_{18}\text{H}_{12}$  clusters. After this, we scrutinize the possibility of multi-doping of larger hydrogenated Si cages ( $\text{Si}_{24}\text{H}_{24}$ ,  $\text{Si}_{28}\text{H}_{28}$ ) with highly magnetic dimers ( $\text{Cr}_2^+$ ,  $\text{Mn}_2^+$  and  $\text{CrMn}^+$ ) with the view of going beyond the single-atom dopant  $4s^13d^5$  septet limit.

## 8.1 $M_2\text{Si}_{18}\text{H}_{12}$ Clusters

The starting point of our investigation is an extended configurational search, which confirmed that the ground-state structure of  $\text{Cr}_2\text{Si}_{18}$  is indeed a highly symmetric ( $D_{6h}$ ) double prism (see Fig. 8.1(b)), as suggested by Kumar and Kawazoe [155] and Ji and Luo [181]. An energetic difference to the next isomer of 0.68 eV and a HOMO-LUMO gap of 1.17 eV indicate a rather high stability of this symmetrical structure. As can be clearly seen from Fig. 8.1, the  $\text{Cr}_2\text{Si}_{18}$  structure is basically composed of two  $\text{CrSi}_{12}$  prisms [183, 184] merged together. Although such a combination does not provide the possibility of achieving electronic shell closure ( $18 \times 4 e^-$  from Si atoms +  $6 \times 2 e^-$  from Cr atoms =  $84 e^-$ , with  $2d$  or  $1h$  shell closure requiring 68 and 90 electrons, respectively) [143, 146, 149], it does effectively saturate all Si dangling bonds through the strong Cr-Si interaction, thus stabilizing the found geometrical structure. Therefore, one may expect the electronic structure of the  $\text{Cr}_2\text{Si}_{18}$  cluster to be rather similar to that of its “monomer”, *i.e.*  $\text{CrSi}_{12}$ .

Indeed, the electronic structure analysis reveals a very similar character of the dopant-cage interaction, as is observed for the  $\text{CrSi}_{12}$  case. For instance, the comparison of the density of states (DOS) diagram of  $\text{Cr}_2\text{Si}_{18}$  (Fig. 8.2(b)) and the corresponding DOS of  $\text{CrSi}_{12}$  (Fig. 8.2(a)) shows that the main features of the two are very similar, just with  $\text{Cr}_2\text{Si}_{18}$  states being higher populated, owing to the presence of two Cr atoms and six additional Si atoms. Here in both cases one can see a significant contribution of the Cr dopant atom to the frontier levels of the cluster, which illustrates a strong interaction

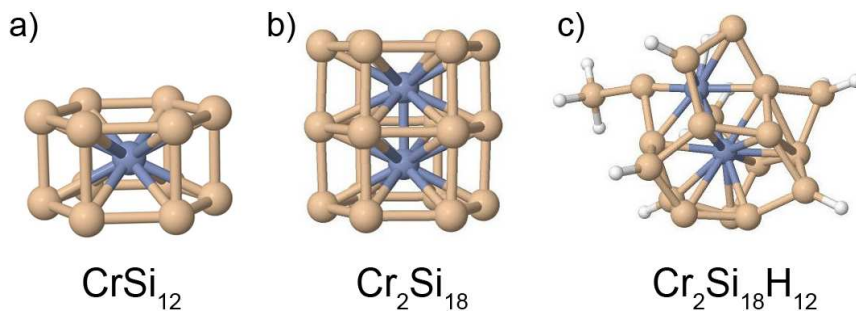


Figure 8.1: The identified ground-state structures of (a) CrSi<sub>12</sub>, (b) Cr<sub>2</sub>Si<sub>18</sub> and (c) Cr<sub>2</sub>Si<sub>18</sub>H<sub>12</sub> with singlet spin state in all cases.

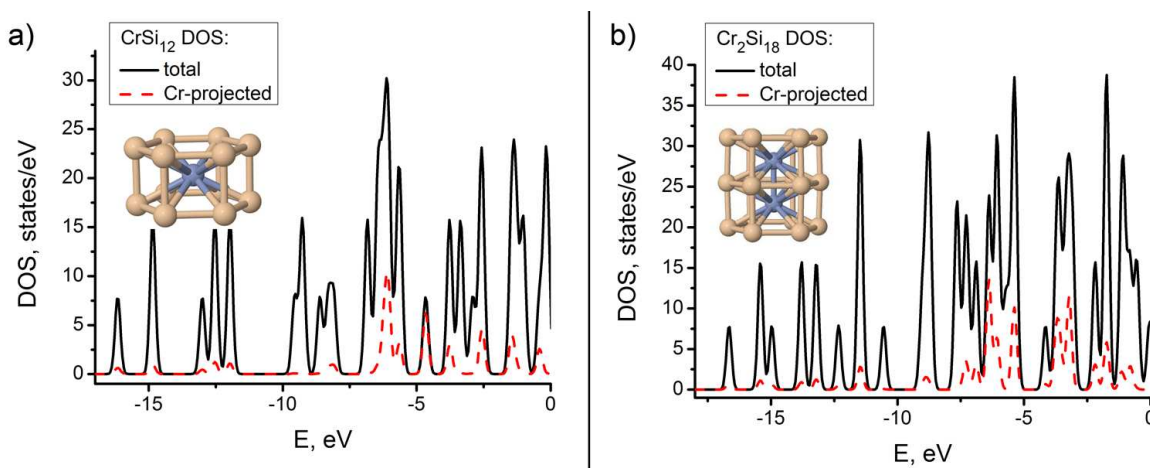


Figure 8.2: Total density of states (DOS) (black solid line) and DOS projected on the metal dopant (red dashed line) for (a) CrSi<sub>12</sub> and (b) Cr<sub>2</sub>Si<sub>18</sub>. Highest occupied orbitals lie at  $-5.63$  eV (CrSi<sub>12</sub>) and  $-5.32$  eV (Cr<sub>2</sub>Si<sub>18</sub>); the vacuum level is used as a zero reference.

between the dopant and the cage. A quite similar DOS structure has been observed earlier for  $MSi_{16}^+$  ( $M = \text{Ti, V, Cr}$ ) cages [146]. In contrast, larger hydrogenated silicon cages with the dopant metal isolated inside exhibit negligibly small Cr-Si hybridization, which is illustrated by a clear separation of the silicon and metal dopant levels in the DOS (see Fig. 6.3 and Fig. 7.4) [147, 148]. This view is in line with the complete quenching of the Cr spin state within both structures and is also complemented by the analysis of the frontier orbitals shapes, where the contribution of Cr is quite pronounced (see insets in Table 8.1).

As has been mentioned above, a rather high value of the HOMO-LUMO gap (1.17 eV for Cr<sub>2</sub>Si<sub>18</sub> cluster) also indicates that the structure should be rather stable. However, it is significantly smaller than the one corresponding to truly “magic” structures, like *e.g.* VSi<sub>16</sub><sup>+</sup> (more than 2 eV) [146]. Interestingly, even the positions of the HOMO and LUMO of the Cr<sub>2</sub>Si<sub>18</sub> cluster ( $-5.32$  eV and  $-4.15$  eV with respect to the vacuum level) are very close to those of the CrSi<sub>12</sub> cluster ( $-5.63$  eV and  $-4.66$  eV respectively, see Table 8.1). Similar to the CrSi<sub>12</sub> cluster, argon does not bind to either neutral or positively

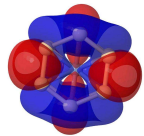
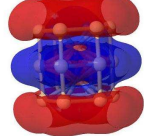
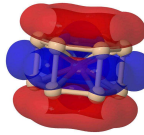
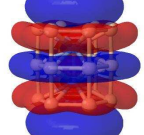
|      | CrSi <sub>12</sub> |         |   | Cr <sub>2</sub> Si <sub>18</sub> |         |   |
|------|--------------------|---------|---|----------------------------------|---------|---|
|      | Energy, eV         | Gap, eV | Isosurface  | Energy, eV                       | Gap, eV | Isosurface  |
| HOMO | -5.63              | 0.96    |  | -5.32                            | 1.17    |  |
| LUMO | -4.66              |         |  | -4.15                            |         |  |

Table 8.1: Frontier orbitals of CrSi<sub>12</sub> and Cr<sub>2</sub>Si<sub>18</sub> clusters.

charged Cr<sub>2</sub>Si<sub>18</sub> clusters (with an optimized Ar-Si distance of about 4Å) which supports the experimental observations reported in ref. [29].

To check if the hydrogen termination idea is applicable in our case, we also run a global geometry optimization of the hydrogen-terminated Cr<sub>2</sub>Si<sub>18</sub>H<sub>12</sub> structure. The identified ground-state structure has a heavily distorted geometry, presented in Fig. 8.1(c). The symmetric hydrogenated double-prism is only a local minimum, lying 1.81 eV higher than the here identified ground-state structure. This may be explained in view of the strong interaction between Si and H atoms, trying to saturate Si dangling bonds. With the apparently insufficient space within the cluster to keep the dopant atoms inside, the structure ends up with the complex combination of Si-H and Si-Cr interactions which makes the structure “explode”. This result agrees well with the previously reported insufficient space within Si<sub>16</sub>H<sub>16</sub> clusters for conserving any 3*d* metal dopants [147]. While in case of Si<sub>16</sub>H<sub>16</sub> the average radius of the cage is about 3Å, here in the symmetric Cr<sub>2</sub>Si<sub>18</sub> cluster the dopant-cage distance amounts only to 2.67Å, which makes the concept of conservation of the atomic character of the magnetic dopant impossible.

Curiously, the available space within the Si<sub>18</sub> double prism structure is hardly enough to accommodate two dopant atoms even with the strong dopant-cage interaction. To check on the size effects, we have tried to locate the  $M_2\text{Si}_{18}$  and  $M_2\text{Si}_{18}\text{H}_{12}$  ground-state structures for the metal dopant having more valence electrons. For this, we have chosen the iron atom, having the 4*s*<sup>2</sup>3*d*<sup>6</sup> configuration, where the half-filled *d*-shell stability is broken by an additional electron. Our global geometry optimization has found distorted structures for both Fe<sub>2</sub>Si<sub>18</sub> and Fe<sub>2</sub>Si<sub>18</sub>H<sub>12</sub> clusters (Fig. 8.3). With symmetrical double-prism local minima isomers lying 0.75 eV and 2.79 eV higher in energy for Fe<sub>2</sub>Si<sub>18</sub> and Fe<sub>2</sub>Si<sub>18</sub>H<sub>12</sub> respectively, it is quite evident that the insufficient space within the cluster leads to a significant distortion of the structure. Obviously, due to the even stronger

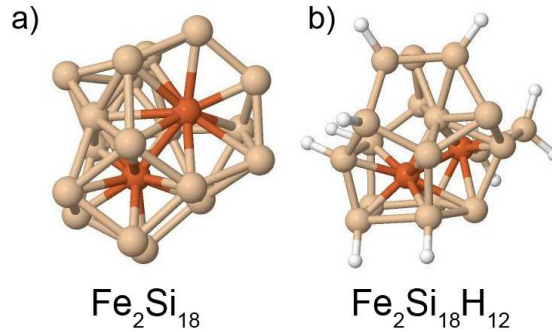


Figure 8.3: Ground-state structures of (a)  $\text{Fe}_2\text{Si}_{18}$  and (b)  $\text{Fe}_2\text{Si}_{18}\text{H}_{12}$  clusters.

interaction between the dopant and the cage, the dopant spin state is quenched to singlet in both cases.

Therefore, it is evident that the  $\text{Si}_{18}$  cluster is generally too small to accommodate two dopants with their magnetic character preserved. Thus, we need to take a look at larger  $\text{Si}_n\text{H}_n$  cages in order to be able to stabilize multiple magnetic dopants. As has been reported earlier [147], extensive sampling runs suggest empty cage geometries as ground states for the larger hydrogenated Si fullerenes, such as  $\text{Si}_{20}\text{H}_{20}$ ,  $\text{Si}_{24}\text{H}_{24}$ ,  $\text{Si}_{26}\text{H}_{26}$  and  $\text{Si}_{28}\text{H}_{28}$ . Eventually, these cages should offer enough space to also host multicore dopants, which allow achieving higher magnetic moments than are available through encapsulation of the single-atom transition metals. This idea constitutes the next part of our investigation.

## 8.2 Electronic Structure of $\text{Cr}_2^+$ , $\text{Mn}_2^+$ , and $\text{CrMn}^+$ Magnetic Dimers

The first question we have to answer is whether the suggested dimers ( $\text{Cr}_2^+$ ,  $\text{Mn}_2^+$ , and  $\text{CrMn}^+$ ) are indeed highly magnetic. For this, we optimized the geometries of all three dimers for all possible spin states at the hybrid functional level using the PBE0 [72] functional, which is commonly agreed to yield reliable results for the rich transition metal chemistry [76]. The obtained results are then compared to the neutral  $\text{Cr}_2$  and  $\text{Mn}_2$  dimers in order to discuss the difference in their electronic structure.

Table 8.2 summarizes the obtained results for the cationic dimers. In good agreement with experiment [182],  $\text{Cr}_2^+$  and  $\text{Mn}_2^+$  both exhibit ground-state configurations with 11 unpaired electrons. Since the  $3d$  electrons are localized at the metal cores in both clusters, bonding is predominantly mediated by the remaining  $4s$  electron, shared between the two atoms ( $\text{Cr}_2^+$ ), or the remaining three  $4s$  electrons ( $\text{Mn}_2^+$ ) situated in a fully occupied bonding and a singly occupied antibonding  $\sigma$ -orbital, respectively. The experimentally observed values of the bond energies of about 1.4 eV [185] also agree well with the obtained results.

| unpaired $e^-$  | $M$ - $M$ distance,<br>$\text{\AA}$ | Relative energy,<br>eV | Binding energy,<br>eV |
|-----------------|-------------------------------------|------------------------|-----------------------|
| $\text{Cr}_2^+$ |                                     |                        |                       |
| <b>11</b>       | <b>2.90</b>                         | <b>0.00</b>            | <b>1.55</b>           |
| 9               | 2.64                                | 1.03                   | 0.52                  |
| 7               | 2.28                                | 3.24                   | -1.68                 |
| 5               | 1.77                                | 3.74                   | -2.18                 |
| 3               | 1.65                                | 4.31                   | -2.76                 |
| 1               | 1.56                                | 4.24                   | -2.68                 |
| $\text{Mn}_2^+$ |                                     |                        |                       |
| 13              | 4.18                                | 2.51                   | -0.83                 |
| <b>11</b>       | <b>2.93</b>                         | <b>0.00</b>            | <b>1.68</b>           |
| 9               | 2.48                                | 0.97                   | 0.71                  |
| 7               | 2.13                                | 3.67                   | -1.99                 |
| 5               | 1.90                                | 5.43                   | -3.75                 |
| 3               | 1.73                                | 7.46                   | -5.78                 |
| 1               | 1.63                                | 7.14                   | -5.46                 |
| $\text{CrMn}^+$ |                                     |                        |                       |
| 12              | 3.34                                | 0.90                   | 0.61                  |
| <b>10</b>       | <b>2.80</b>                         | <b>0.00</b>            | <b>1.51</b>           |
| 8               | 2.44                                | 1.72                   | -0.22                 |
| 6               | 2.29                                | 4.40                   | -2.89                 |
| 4               | 1.81                                | 4.45                   | -2.95                 |
| 2               | 1.60                                | 5.54                   | -4.04                 |
| 0               | 1.61                                | 6.07                   | -4.56                 |

Table 8.2: Optimized  $M$ - $M$  distances, relative stabilities and binding energies (all calculated using PBE0 functional with “tier 3” basis set) for all possible spin states of  $\text{Cr}_2^+$ ,  $\text{Mn}_2^+$ , and  $\text{CrMn}^+$  dimers.

In  $\text{CrMn}^+$ , two  $4s$  orbitals occupy a bonding orbital, leading to the overall number of ten unpaired  $3d$  electrons. In all cases the rather high bond lengths (2.80 to 2.93  $\text{\AA}$ ) confirm that only  $s$ -electrons contribute to bonding. Despite of being isoelectronic to the neutral  $\text{Cr}_2$  dimer,  $\text{CrMn}^+$  shows a very different electronic structure.  $\text{Cr}_2$  is a singlet with a formal sextuple bond, exhibiting a bond length of only 1.59  $\text{\AA}$ , which agrees well with the experimental value of 1.68  $\text{\AA}$  [187].  $\text{Mn}_2$ , on the other hand, is an only weakly bound (0.17 eV) dimer with a very long equilibrium distance of 3.48  $\text{\AA}$  (Table 8.3), and can be described as a van der Waals molecule. Again, this agrees perfectly with the experimentally reported values of the bond length (3.4  $\text{\AA}$ ) and the bond energy ( $0.44 \pm 0.30$  eV), *cf.* ref. [188, 189].

Thus, a strong  $3d$  valence electron localization in  $\text{Cr}_2^+$ ,  $\text{Mn}_2^+$ , and  $\text{CrMn}^+$  dimers due to the half-filled  $3d$  shells of Cr and Mn atoms, observed in the core-level X-ray absorption spectroscopy experiments [182], is also confirmed by DFT calculations at the hybrid PBE0 functional level. This opens the perspective of using such high spin dimers as dopants

| unpaired e <sup>-</sup> | $M$ - $M$ distance,<br>Å | Relative energy,<br>eV | Binding energy,<br>eV |
|-------------------------|--------------------------|------------------------|-----------------------|
| Cr <sub>2</sub>         |                          |                        |                       |
| 12                      | 3.23                     | 1.36                   | 0.11                  |
| 10                      | 2.71                     | 0.98                   | 0.49                  |
| 8                       | 2.38                     | 2.56                   | -1.08                 |
| 6                       | 2.04                     | 2.40                   | -0.93                 |
| 4                       | 1.79                     | 1.47                   | 0.00                  |
| 2                       | 1.68                     | 1.02                   | 0.45                  |
| <b>0</b>                | <b>1.59</b>              | <b>0.00</b>            | <b>1.47</b>           |
| Mn <sub>2</sub>         |                          |                        |                       |
| 14                      | 2.88                     | 3.49                   | -3.32                 |
| 12                      | 2.91                     | 0.94                   | -0.78                 |
| <b>10</b>               | <b>3.48</b>              | <b>0.00</b>            | <b>0.17</b>           |
| 8                       | 2.54                     | 1.96                   | -1.80                 |
| 6                       | 1.96                     | 3.50                   | -3.34                 |
| 4                       | 2.21                     | 5.23                   | -5.06                 |
| 2                       | 2.49                     | 8.36                   | -8.19                 |
| 0                       | 1.64                     | 5.61                   | -5.44                 |

Table 8.3: Optimized  $M$ - $M$  distances, relative stabilities and binding energies (all calculated using PBE0 functional with “tier 3” basis set) for all possible spin states of Cr<sub>2</sub> and Mn<sub>2</sub> dimers.

for larger hydrogenated Si cages, in order to construct highly magnetic building blocks for novel engineered cluster-assembled materials.

### 8.3 Si<sub>24</sub>H<sub>24</sub> Cage Doped with Magnetic Dimers

The next question to address is what size of the Si <sub>$n$</sub> H <sub>$n$</sub>  cage is capable of accommodating an intact high spin state dimer, conserving its individual magnetic moment. As we have shown previously [147], Si<sub>20</sub>H<sub>20</sub> is the smallest cluster capable of conserving the atomic character of the high-spin single-atom dopant, such as Cr. Therefore, intuitive candidates for multi-doping are the next hydrogenated Si fullerene-like cages, *i.e.* Si<sub>24</sub>H<sub>24</sub>, Si<sub>26</sub>H<sub>26</sub>, and Si<sub>28</sub>H<sub>28</sub>.

As the first step in this part of our study we have run global geometry optimization of the Si<sub>24</sub>H<sub>24</sub> cage doped with the chromium dimer cation Cr<sub>2</sub><sup>+</sup>, denoted therewith as Cr<sub>2</sub><sup>+</sup>@Si<sub>24</sub>H<sub>24</sub>. The unbiased configurational sampling reveals that the ground-state structure corresponds to a highly symmetric  $D_{6d}$  structure (Fig. 8.4(a)) with 11 unpaired electrons (structure I). Interestingly, this turned out to be not the only possible structure with a Cr<sub>2</sub><sup>+</sup> dimer encapsulated within the cage. Figure 8.4(b) illustrates another high-spin isomer with the dimer oriented perpendicular to the cage’s principal axis, which corresponds to the  $C_{2v}$  symmetry group (structure II). This structure also has 11 unpaired



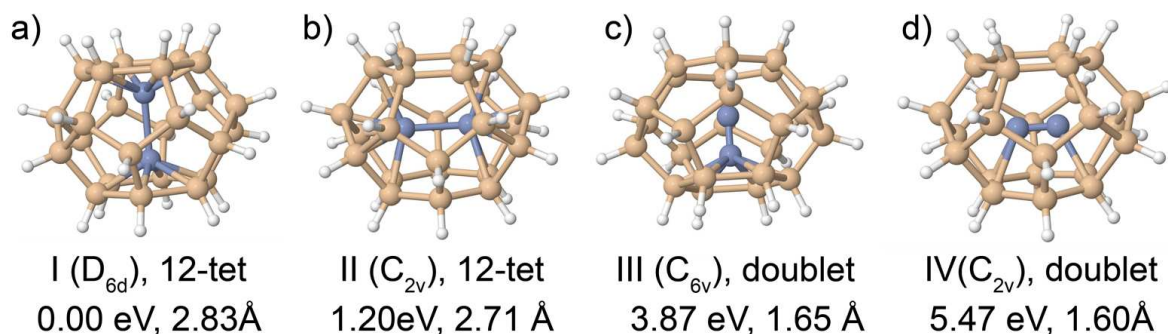


Figure 8.4: Selected cage-like structures of  $\text{Cr}_2^+@Si_{24}H_{24}$  with their multiplicities, relative energies and Cr-Cr bond lengths. (a) ground-state structure ( $D_{6d}$ , structure I) with 11 unpaired electrons; (b) structure II (11 unpaired electrons, 1.20 eV above the global minimum); c) and d) – doublet structures with one unpaired electron (3.87 and 5.47 eV less stable than the ground-state structure, respectively).

electrons in total. However, it is 1.20 eV higher in energy than the ground-state structure. For comparison, the most stable compact structure (with distorted non-cage geometry) is 2.09 eV less stable than the ground-state structure.

It is also possible to stabilize other spin states within the cage. For example, a doublet  $\text{Cr}_2^+$  dimer can also be encapsulated in the  $\text{Si}_{24}\text{H}_{24}$ , oriented either along (structure III,  $C_{6v}$ ) or perpendicular to (structure IV,  $C_{2v}$ ) the cage's principal axis (see Fig. 8.4(c) and Fig. 8.4(d)). However, these structures possess much higher total energies (3.87 eV and 5.47 eV higher than the ground-state structure, respectively), which agrees well with the 4.24 eV difference between the corresponding spin states of the isolated  $\text{Cr}_2^+$  dimer. Another peculiarity is a remarkable agreement in the bond lengths of the isolated and encapsulated  $\text{Cr}_2^+$  dimers. In both high-spin structures the PBE0-optimized Cr-Cr bond lengths are 2.83 Å and 2.71 Å (compared to the 2.90 Å for isolated  $\text{Cr}_2^+$  with 11 unpaired electrons), while for low-spin state structures the corresponding distances are 1.65 Å and 1.60 Å (compared to 1.56 Å in an isolated doublet  $\text{Cr}_2^+$  dimer).

Stabilization of the high spin state of the encapsulated dimer in the  $\text{Cr}_2^+@Si_{24}H_{24}$  ground-state structure, and reasonable agreement in both relative energies and equilibrium distances between the dopants encapsulated in different cage-like isomers and the isolated  $\text{Cr}_2^+$  dimers, suggest that there should not be much interaction between the dopant dimer and the cage. On the other hand, a rather high binding energy (3.26 eV for structure I) and a notable difference between the two high-spin isomers (1.20 eV between the structure I and structure II) indicate the presence of some interaction that helps to stabilize the endohedral structure. In order to clarify this, we plot the spin density distribution within the  $\text{Cr}_2^+@Si_{24}H_{24}$  ground-state structure (see the inset in Fig. 8.5) and analyze the density of states (DOS) diagram (Fig. 8.5).

The 3D spin density distribution in the inset of the Fig. 8.5 clearly indicates that the

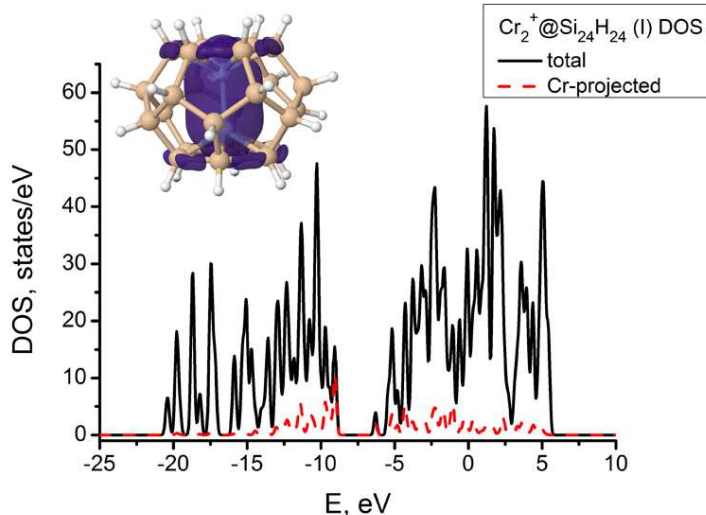


Figure 8.5: Total density of states (black solid line) and DOS projected on the metal dopant (red dashed line) for  $\text{Cr}_2^+@Si_{24}H_{24}$  (structure I, ground state) calculated at the hybrid PBE0 functional level. Highest occupied state lies at  $-9.04$  eV, lowest unoccupied state lies at  $-6.30$  eV; the vacuum level is used as reference. The inset shows the spin density distribution (isosurface at  $0.02 e^-/\text{\AA}$ ) within the cluster, which resides predominantly on two metal cores.

unpaired electrons are predominantly located on the Cr atoms of the encapsulated dimer. However, there are two protrusions of the spin density through two hexagonal facets of the cage, which indicate some spin density delocalization over the adjacent Si-Si bonds. Consistent with this explanation, the density of states (DOS) plot depicts that, despite the predominance of the Cr in the last peak in the occupied orbitals area (around  $-9$  eV), which agrees nicely with the position of the ten unpaired  $d$ -electrons in the isolated  $\text{Cr}_2^+$  dimer, there is a small fraction of cage Si atoms contributing to this peak.

The picture gets further support from the total density difference analysis (Fig. 8.6(a)). For this, we subtract the sum of the total densities of the empty  $Si_{24}H_{24}$  cage and the isolated  $\text{Cr}_2^+$  dimer from the total density of the  $\text{Cr}_2^+@Si_{24}H_{24}$  aggregate. The resulting total density (blue regions indicate more electronic density, *i.e.* more negative charge) shows that in the  $\text{Cr}_2^+@Si_{24}H_{24}$  aggregate there is more electronic density located at the edges of the structure (connecting Cr atoms with the hexagonal facets of the cage). At the same time the small red-colored areas at the Cr atoms indicate that there was slightly higher electron density on Cr atoms in the isolated dimer. This suggests that a fraction of the  $d$ -electrons, located at the Cr cores in the isolated dimer, are now partially re-distributed in the area between the outer sides of the dimer and the hexagonal facets of the cage, however still located mostly at the metal core. On the other hand, the one remaining unpaired  $s$ -electron, through which binding in the isolated  $\text{Cr}_2^+$  dimer was mediated, is intact, which is indicated by the zero total density difference between the Cr cores, and is also reflected by the conserved Cr-Cr equilibrium distance.

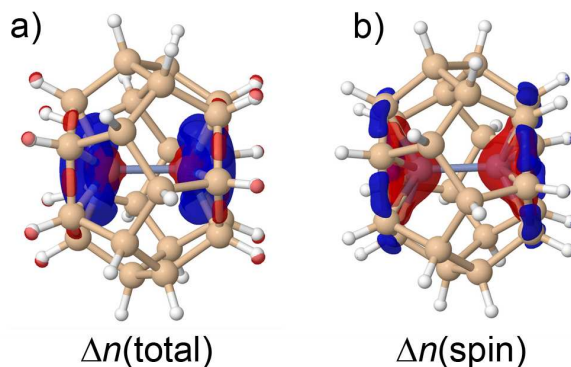


Figure 8.6: 3D distribution of the (a) total electron density difference  $\Delta n(\text{total}) = [n(\text{Cr}_2^+@Si_{24}H_{24}) - n(Si_{24}H_{24}) - n(\text{Cr}_2^+)]$  and (b) spin density difference  $\Delta n(\text{spin}) = [n(\text{Cr}_2^+@Si_{24}H_{24}) - n(\text{Cr}_2^+)]$  calculated at the hybrid PBE0 functional level; blue color depicts regions with more electron density. Note that here enlarged ( $0.015 \text{ e}^-/\text{\AA}$ ) isosurfaces are presented for clarity.

This is in line with the spin density difference between the  $\text{Cr}_2^+@Si_{24}H_{24}$  aggregate and the isolated  $\text{Cr}_2^+$  dimer, depicted in Fig. 8.6(b). Here one can see that in the resulting  $\text{Cr}_2^+@Si_{24}H_{24}$  aggregate, there is more spin density located at the outskirts of the cluster (Si-Si bonds within the two hexagonal facets) and less spin density at the Cr cores, compared to the isolated  $\text{Cr}_2^+$  dimer. However, the spin density between the cores stays the same, as indicated by the zero density difference in this area, and by the total spin density distribution within the cluster (inset in the Fig. 8.5). Thus one can conclude that, while the overall high spin state of the structure is conserved, the additional interaction *via* the adjacent hexagonal facets of the cage helps to stabilize the resulting aggregate, which is also reflected in large HOMO-LUMO gap value of 2.74 eV.

The higher total energy of the structure II (1.20 eV less stable than the global minimum) can be explained in the view of the dopant's location within the cluster. As can be seen in the Fig. 8.4(b), it features a shorter intermetallic distance (2.71 Å), which is 0.19 Å smaller than the equilibrium distance in the high-spin  $\text{Cr}_2^+$  dimer (see Table 8.2). Such unfavorable geometry is most likely caused by the orientation of adjacent pentagonal facets of the cage, which need to be used for additional partial spin density delocalization similar to the above described case of the ground-state structure I (compare Fig. 8.7 and Fig. 8.6(b)). Therefore, the more complicated character of the hybridization and consequently shortened intermetallic distance in the structure II of the  $\text{Cr}_2^+@Si_{24}H_{24}$  aggregate leads to the higher total energy, compared to the ground-state structure.

We have also run global geometry optimization and carried out subsequent electronic structure analysis of the identified ground-state structures for two other dopants ( $\text{Mn}_2^+$ ,  $\text{CrMn}^+$ ) encapsulated within the  $\text{Si}_{24}\text{H}_{24}$  cage and found quite similar results. Fig. 8.8 illustrates the obtained ground-state structures.

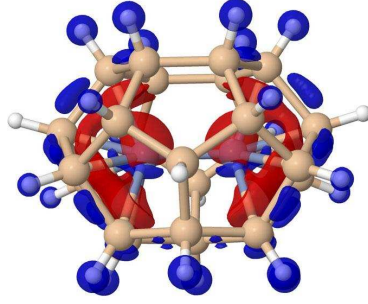


Figure 8.7: 3D distribution of the spin density difference for the  $\text{Cr}_2^+@Si_{24}H_{24}$  structure II:  $\Delta n(\text{spin}) = [n(\text{Cr}_2^+@Si_{24}H_{24}) - n(\text{Cr}_2^+)]$ .

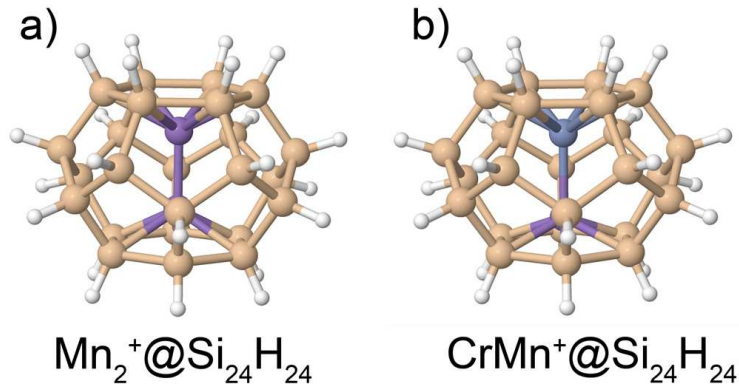


Figure 8.8: Ground-state structures of (a)  $Mn_2^+@Si_{24}H_{24}$  (9 unpaired  $e^-$ , 2.59 Å Mn-Mn distance, 1.89 eV to the next (distorted) isomer) and (b)  $CrMn^+@Si_{24}H_{24}$  (10 unpaired electrons, 2.80 Å Cr-Mn distance, 4.29 eV to the next isomer).

As expected,  $CrMn^+$  encapsulated within the  $Si_{24}H_{24}$  cage (see Fig. 8.8(b)) has an equilibrium distance close to the one observed for the isolated cluster (2.80 Å in both cases) and exhibits a high spin state of ten unpaired electrons. The analysis of the spin density distribution of  $CrMn^+@Si_{24}H_{24}$  (see inset in Fig. 8.9(a)) reveals that the ten unpaired electrons are predominantly located on the metal cores, with the Mn atom (on the right in the inset picture) showing more interaction with the adjacent hexagonal facet of the Si cage. The density of states depicts two distinct peaks for the  $d$ -electrons located at the Cr and Mn cores, with their separate positions (near  $-9$  eV and  $-13$  eV, respectively, which matches the positions of the corresponding electrons in the isolated  $CrMn^+$  dimer reasonably well) suggesting a localized character of  $d$ -electrons belonging to Cr and Mn metal cores. Overall, it shows a very similar stabilization mechanism as was discussed for  $Cr_2^+@Si_{24}H_{24}$  above, with some fraction of the Mn electrons partially delocalized over the adjacent hexagonal cage facet, and the Cr atom compensating for this by shifting some of its electronic density along the Cr-Mn bond towards Mn (see Fig. 8.10(a)). The lower degree of interaction between the encapsulated dopant and the surrounding cage compared to the  $Cr_2^+@Si_{24}H_{24}$  case (compare Fig. 8.9(a) and Fig.

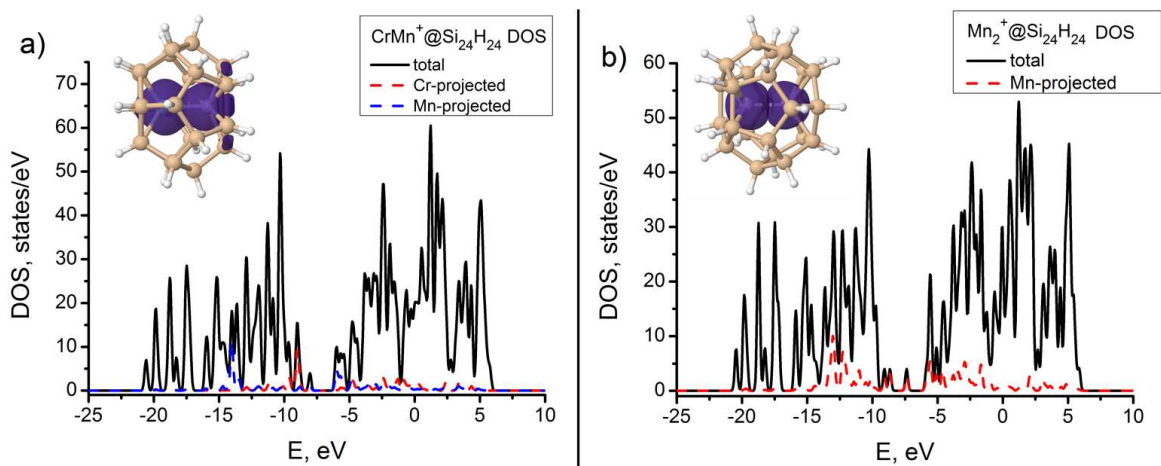


Figure 8.9: Total density of states and DOS projected on the metal dopants for (a)  $\text{CrMn}^+\text{@Si}_{24}\text{H}_{24}$  (HOMO lies at  $-8.04$  eV, LUMO at  $-6.02$  eV) and (b)  $\text{Mn}_2^+\text{@Si}_{24}\text{H}_{24}$  (HOMO lies at  $-7.38$  eV, LUMO at  $-5.85$  eV) aggregates. The insets show the spin density distribution within clusters.

8.5), is reflected in less delocalization of the spin density and sharper metal-projected DOS peaks. Besides, it is also supported by a smaller value of the binding energy ( $2.67$  eV for  $\text{CrMn}^+\text{@Si}_{24}\text{H}_{24}$  *vs.*  $3.26$  eV for  $\text{Cr}_2^+\text{@Si}_{24}\text{H}_{24}$ ).

The  $\text{Mn}_2^+\text{@Si}_{24}\text{H}_{24}$  aggregate shows slightly different behavior. Here also the unpaired electrons, as expected, are predominantly located on the two Mn metal cores (see inset in Fig. 8.9(b)). Two distinct peaks around  $-13$  eV in the DOS plot support this view. However, the total number of unpaired electrons is not eleven, as might be expected from the analogy with the  $\text{Cr}_2^+\text{@Si}_{24}\text{H}_{24}$  results, but only nine. To figure out where this additional electron pairing comes from, we take a look at the spin density difference between the  $\text{Mn}_2^+\text{@Si}_{24}\text{H}_{24}$  aggregate and the  $\text{Mn}_2^+$  dimer with nine unpaired electrons (Fig. 8.10(b)). Here the additional electron density between the metal cores (blue region) clearly indicates additional binding in the encapsulated dimer compared to the isolated one. This suggests that one additional *d*-electron can be used together with the three remaining *s*-electrons to additionally stabilize the bond within the encapsulated dimer. This is also reflected in the shortened Mn-Mn distance ( $2.59$  Å in  $\text{Mn}_2^+\text{@Si}_{24}\text{H}_{24}$  aggregate *vs.*  $2.93$  Å in  $\text{Mn}_2^+$  dimer). Additionally, the  $\text{Mn}_2^+\text{@Si}_{24}\text{H}_{24}$  structure exhibits the least interaction between the dopant and the cage among all three considered dopants (compare insets in Fig. 8.5 and Fig. 8.9), which is also reflected in the smallest binding energy value of  $1.77$  eV.

Thus the results presented above suggest that  $\text{Si}_{24}\text{H}_{24}$  cage is generally large enough to accommodate high-spin dimer dopants, such as  $\text{Cr}_2^+$ ,  $\text{Mn}_2^+$ , and  $\text{CrMn}^+$ . While the stabilization of the single-atom dopants is largely mediated through the *s*-electrons, which helps to stabilize the symmetrical position of such dopants in the middle of the cage, as it has been previously shown *e.g.* for the  $\text{CrSi}_{20}\text{H}_{20}$  aggregate [147], here in case of magnetic

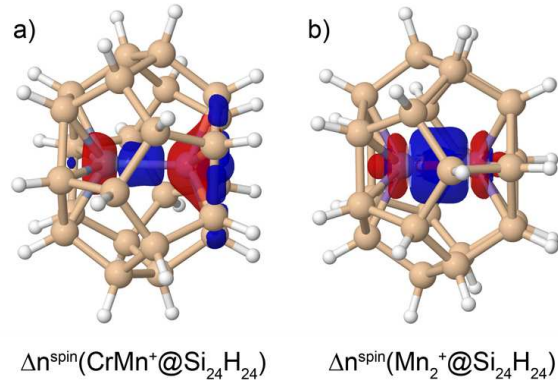


Figure 8.10: 3D distribution of the spin density difference for (a) the  $\text{CrMn}^+@_{\text{Si}_{24}\text{H}_{24}}$  aggregate:  $\Delta n(\text{spin}) = [n(\text{CrMn}^+@_{\text{Si}_{24}\text{H}_{24}}) - n(\text{CrMn}^+)]$ ; and (b) the  $\text{Mn}_2^+@_{\text{Si}_{24}\text{H}_{24}}$  aggregate:  $\Delta n(\text{spin}) = [n(\text{Mn}_2^+@_{\text{Si}_{24}\text{H}_{24}}) - n(\text{Mn}_2^+, 10\text{-tet})]$ .

dimers the interaction picture is more complicated. Owing to the naturally less symmetrical orientation of the dimer compared to the single atom, less space within the cage, and higher spin densities, the dimer aggregates structures are predominantly stabilized either through partial delocalization of the spin density over the adjacent (preferably hexagonal) facets of the cage ( $\text{Cr}_2^+@_{\text{Si}_{24}\text{H}_{24}}$ ,  $\text{CrMn}^+@_{\text{Si}_{24}\text{H}_{24}}$ ), or *via* increasing the binding between the metal cores ( $\text{Mn}_2^+@_{\text{Si}_{24}\text{H}_{24}}$ ). However, these subtle effects do not cause any distortion of the symmetrical cage structure or quenching of the total spin moment (except from the lowered spin state of the  $\text{Mn}_2^+@_{\text{Si}_{24}\text{H}_{24}}$ ), but nevertheless help to stabilize the structures. Therefore, despite the fact that the dimer encapsulated within the  $\text{Si}_{24}\text{H}_{24}$  cage might not be completely isolated, such  $M_2^+@_{\text{Si}_{24}\text{H}_{24}}$  aggregates allow stabilization of the high spin states of the magnetic dimer dopants. Especially interesting is the  $\text{CrMn}^+@_{\text{Si}_{24}\text{H}_{24}}$  aggregate, which exhibits an intriguing combination of conserving the original high spin state of the dimer (10 unpaired electrons) and keeping the dopant-cage interaction relatively low, thus suggesting a route to go beyond the single-atom dopant  $4s^1 3d^5$  septet limit, exceeding it by almost a factor of two.

## 8.4 $\text{Si}_{28}\text{H}_{28}$ Cage Doped with Two $\text{CrMn}^+$ Dimers

The next obvious question to consider is whether it is possible to further increase the total number of unpaired electrons in the system by encapsulating several of the highly magnetic dimers within a larger cage. If *e.g.* two dimers are only bound through the common *s*-electrons, it raises hopes for the possibility to double the total magnetic moment of such complex aggregate. To check this assumption, we run a global geometry optimization of the  $\text{Si}_{28}\text{H}_{28}$  cage accommodating two  $\text{CrMn}^+$  dopants, *i.e.*  $(\text{CrMn}^+)_2@_{\text{Si}_{28}\text{H}_{28}}$  aggregate cluster. The  $\text{CrMn}^+$  dopant dimer has been chosen based on the results of the [previous](#) section, as being able to both conserve the high spin moment and to keep the dopant-cage

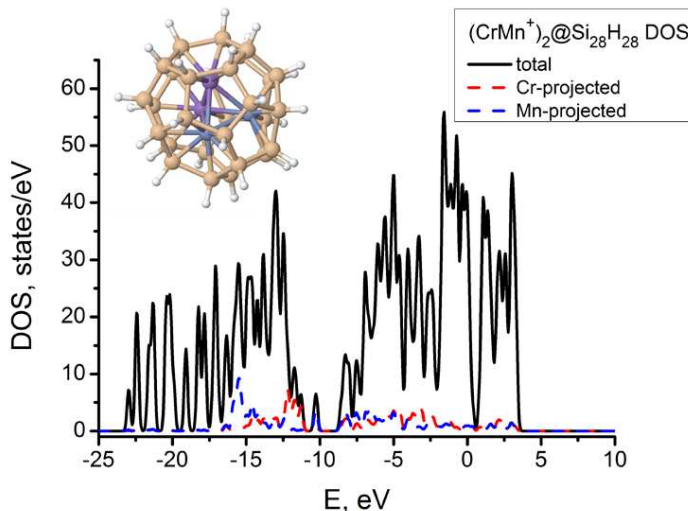


Figure 8.11: Total density of states and DOS projected on the metal dopants for  $(\text{CrMn}^+)_2@Si_{28}H_{28}$ . Highest occupied state lies at  $-10.22$  eV, lowest unoccupied state lies at  $-8.59$  eV. The inset shows the ground-state geometry of the clusters ( $4.76$  eV lower than the next isomer).

interaction low, when encapsulated within the silicon cage.

Indeed, our unbiased sampling revealed that the ground-state structure is a symmetrical  $C_{2v}$  cage (see inset in the Fig. 8.11) with the total number of 18 unpaired electrons (the structure with the fixed 21-tet configuration turned out to be  $0.50$  eV higher in energy). The spin density distribution indicates that all unpaired electrons are predominantly located at the four metal cores (see Fig. 8.12(a)).

A closer look at the DOS diagram reveals two distinct peaks corresponding to Cr-located and Mn-located unpaired electrons, confirming their localized character. An additional Mn peak at  $-10$  eV shows partial redistribution of the Cr electrons towards the Mn cores. This can also be seen in the spin density difference plot (Fig. 8.12(b)), depicting  $\Delta n(\text{spin}) = n[(\text{CrMn}^+)_2@Si_{28}H_{28}] - 2 \times n[\text{CrMn}^+]$ .

From Fig. 8.12(b) it is obvious that, first, there are less unpaired electrons in the final aggregate than there were in the two isolated dimer cations ( $18$  *vs.*  $20$ ), and, second, that there is some spin density redistribution towards the Mn along two Cr-Mn bonds, which is also reflected in the additional small peak in the DOS plot. The decreased total spin moment may be explained in view of the decreased bond length between Mn atoms. The observed Mn-Mn equilibrium distance in the  $(\text{CrMn}^+)_2@Si_{28}H_{28}$  aggregate is  $2.62$  Å, which is much closer to the one observed for  $Mn_2^+@Si_{24}H_{24}$  ( $2.59$  Å), than to that of the  $Mn_2^+$  dimer cation ( $2.93$  Å). Interestingly,  $Mn_2^+@Si_{24}H_{24}$  exhibits the same decrease of the spin moment (nine unpaired electrons *vs.* expected eleven). Therefore, the above mentioned additional partial redistribution of the spin density towards Mn might be explained as an attempt to compensate for this effect. Besides, such redistribution is also consistent with the results observed for  $\text{CrMn}^+@Si_{24}H_{24}$  structure (see Fig. 8.10(a)).

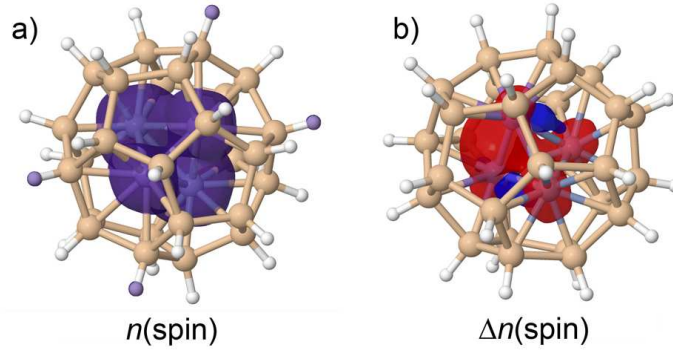


Figure 8.12: (a) 3D distribution of the spin density in the  $(\text{CrMn}^+)_2@Si_{28}H_{28}$  aggregate, and (b) spin density difference  $\Delta n(\text{spin}) = n[(\text{CrMn}^+)_2@Si_{28}H_{28}] - 2 \times n[\text{CrMn}^+]$ .

As can be seen from the DOS plot (Fig. 8.11) and the spin density analysis (Fig. 8.12), there is no large contributions of the cage into the binding. The only notable effect is the distribution of the density within the double dimer dopant itself leading to some intra-dopant charge rearrangement. In fact, the tetrahedral configuration adopted by the four metal cores in the  $(\text{CrMn}^+)_2@Si_{28}H_{28}$  aggregate does not in any case justify a discussion in terms of two adjacent  $\text{CrMn}^+$  dimers. This is supported by the decreased binding energy value of 1.71 eV, which is relatively low compared to the 3.26 eV for the  $\text{Cr}_2^+@Si_{24}H_{24}$  structure, and is very close to that of the  $\text{Mn}_2^+@Si_{24}H_{24}$  cluster (1.77 eV).

Thus, the  $(\text{CrMn}^+)_2@Si_{28}H_{28}$  cluster indeed illustrates the possibility of further increasing the magnetic moment of the endohedrally doped hydrogenated silicon fullerene-like clusters by combining suitable dopants with sufficiently large cages.

## 8.5 Conclusions to Chapter 8

In summary, we have systematically assessed the possibility of multi-doping of hydrogenated silicon clusters to obtain stable cage-like building blocks with high spin moments, suitable for constructing highly magnetic materials. Our unbiased first-principles global geometry optimizations showed that it is possible to conserve both the structural integrity of the host cage and the high spin state of the guest dimer dopants  $M_2^+ = \text{Cr}_2^+$ ,  $\text{Mn}_2^+$ , and  $\text{CrMn}^+$  already for a  $\text{Si}_{24}H_{24}$  fullerene. For instance, for the  $\text{CrMn}^+@Si_{24}H_{24}$  cluster the ground-state structure exhibits a total number of 10 unpaired electrons, which illustrates the possibility of going beyond the single-atom dopant  $4s^1 3d^5$  septet limit by exceeding it by almost a factor of two. The crucial influence of the silicon cage size is thereby illustrated by the distorted ground-state structure obtained for the doubly-doped hydrogenated  $\text{CrSi}_{18}H_{12}$  cluster, previously suggested as smallest cage size capable of encapsulating metal dimers [155]. On the other hand, choosing sufficiently large cages allows accommodating even larger aggregates, as demonstrated for the combination of two  $\text{CrMn}^+$  dimers inside a  $\text{Si}_{28}H_{28}$  fullerene. The corresponding  $(\text{CrMn}^+)_2@Si_{28}H_{28}$



ground-state structure exhibits a total number of 18 unpaired electrons, which is the highest magnetic moment of an endohedral cage reported so far.

This gives confirmation for the exciting perspective of tuning the magnetic moment by encapsulating a range of different dopants (starting from single atoms with different spin states, through highly magnetic dimers, and eventually up to more complex dopant aggregates) into a suitably sized hydrogenated silicon cage. Taking into account that  $N$ -atomic fullerene-like cages are possible with  $N$  taking any even integer value greater than or equal to 20 (except 22) [1], this suggests a path to tune the size of the hydrogenated Si cage to eventually accommodate dopants of virtually any size and complexity. Such highly magnetic doped clusters can then be used as building blocks for cluster-assembled materials, for example by constructing doubly Si-Si bound aggregates, as we have discussed in Chapter 7. Endohedral multi-doping of hydrogenated silicon fullerenes thus appears as a viable route to novel cluster-based materials for magneto-optic applications.

## 9 Towards Adsorption On Surfaces

Of course, the ultimate goal of the cluster studies would be to move from isolated, individual metal-doped Si clusters towards the properties of such clusters in a non-trivial environment, *i.e.* under the influence of other bonding partners, such as extended surfaces. Experimentally this can *e.g.* be realized through deposition of pre-formed cages [190] or through silicide formation on the surface [191, 192, 193]. The central question here is a balanced cage-surface interaction that is strong enough to lead to a desired fixation of the cage, but not too strong to jeopardize the geometric integrity of the cage. For this, obviously, we first need to develop methodology for future studies and to thoroughly benchmark it, preferentially against experimental data. This requires choosing the model surface and suitable adsorbates as a first step. Silicon surfaces attract much attention, due to the variety of possible surface structures and their semiconductor properties [194]. The study of adsorbates on such surfaces is an active area of research with high relevance to micro- and nanoelectronic technology [195]. Among possible adsorbates, Si clusters are widely studied [196].

The Si(111)-(7 × 7) surface is investigated in a large number of studies focused on self-assembled clusters, as this surface provides a structured template, characterized by diffusion barriers between its half unit cells [197]. For instance, it is possible to grow arrays of identical clusters with many metals as adsorbates [198, 199, 200, 201]. Appelfeller, Franz and Dähne [202] recently reported the growth of mixed Sb/Si ring-like nanostructures at submonolayer coverages on the Si(111)-(7 × 7) surface, investigated using scanning tunneling microscopy (STM) [203]. Based on the observed structural and electronic properties, a structure model for such adsorbed clusters has been suggested. However, due to the nature of the STM observations, no detailed atomically resolved geometry information has been obtained. We have chosen this system as a model to check if theoretical investigations can provide the necessary structural information.

### 9.1 Theoretical STM Simulations of the Si(111)-(7 × 7) Surface

The (7 × 7) reconstruction [204] of the Si(111) surface is modeled according to a dimer-atom-stacking-fault (DAS) model suggested by Takayanagi *et al.* in 1985 [205]. This model involves dimers, adsorbed atoms, and stacking faults. Extending through the five top layers of the surface, the unit cell of the reconstruction contains 12 adatoms as well as two triangular subunits, nine dimers and a deep corner hole that extends to the fourth and fifth layers (see Fig. 9.1). The detailed atomic structure of the unit cell containing 200 atoms was suggested by Tong *et al.* in 1988 [206]. The (7 × 7) reconstruction has been extensively studied both experimentally and theoretically in the 1990s (see the references within [204]). Among these studies the work of the J. D. Joannopoulos' group needs to be emphasized [207].

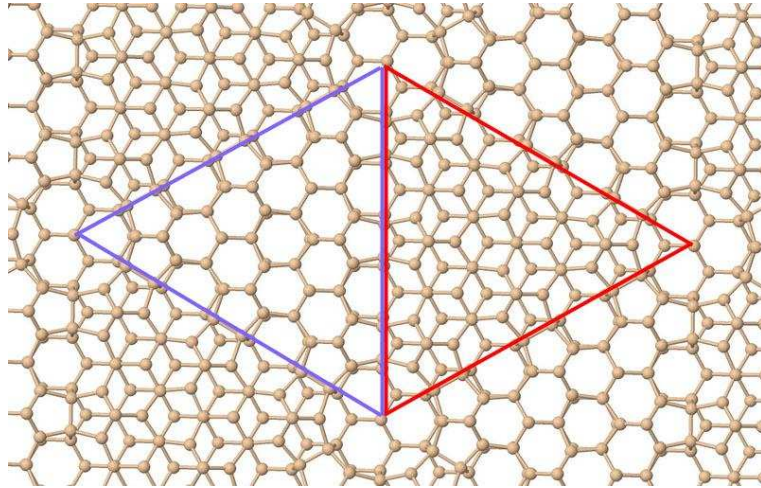


Figure 9.1: Si(111)-(7 × 7) DAS model. The faulted half of the unit cell (FHUC) is on the left, the unfaulted half of the unit cell (UHUC) is on the right.

In order to make sure that we are able to describe the surface properly, we first performed the optimization (PBE/tier2) of the periodic structure having 200 atoms in the unit cell with initial atomic positions taken from ref. [206] with the following lattice vectors:

$$\begin{pmatrix} 26.878 & 0.000 & 0.000 \\ 13.439 & 23.277 & 0.000 \\ 0.000 & 0.000 & 20.000 \end{pmatrix} \text{Å}.$$

After optimization, the surface looks like the one presented in Fig. 9.1.

The successful interpretation of the Si(111)-(7 × 7) surface reconstruction was first obtained based on STM measurements [205]. Scanning tunneling microscopy was developed in the early 1980s by Binnig and Rohrer [208] and has proven to be a powerful technique for the study of the electronic topography of surfaces and adsorbed layers [209, 210]. The principle and operation of STM is rather simple. A sharp metal tip, usually made of W or Pt-Ir alloy, is brought very close (5 – 10 Å) to the sample. At this distance the wave functions of the sample and the tip start to overlap. If a bias voltage is applied to the sample, an electron tunneling current flows between the sample and the tip. The direction of electron flow depends on the sign of the bias applied to the sample. For positive sample bias, electrons flow from occupied states of the tip to empty states of the sample. For negative sample bias the direction is reversed. The tip can be moved in three dimensions, and the tunneling current depends exponentially on the tip-surface distance. Typically, the scan is performed by keeping the tunneling current constant *via* dynamically adjusting the tip-surface distance (the so-called constant current mode).

The objective of our work was to simulate the experimentally observed STM pictures. A simple and prevalent approach to simulate STM images from electronic structure cal-

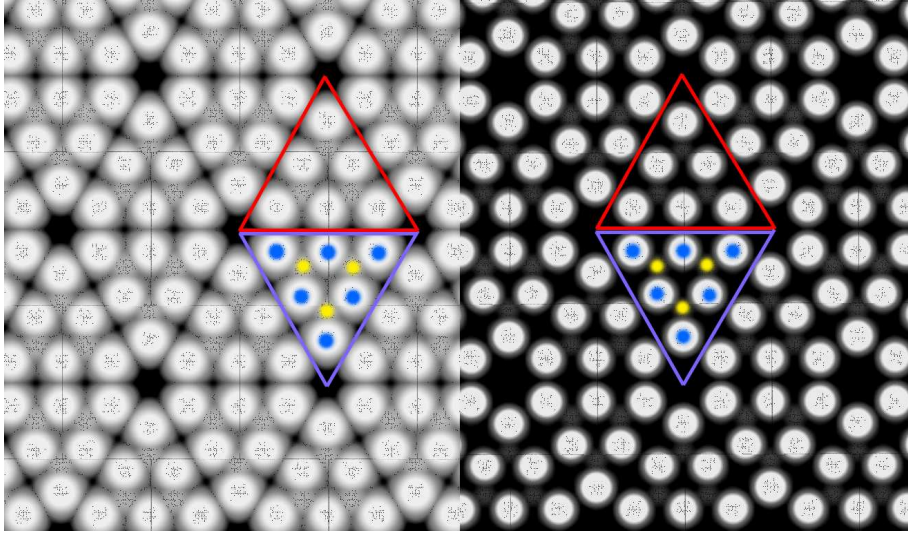


Figure 9.2: Simulated STM image at  $-2.5$  V (filled states, left) and  $+2.0$  V (empty states, right) bias voltage. The faulted half of the unit cell (FHUC) is framed in purple, and the unfaulted half of the unit cell (UHUC) is framed in red. Adatoms of the FHUC are highlighted in blue, and rest-atoms in yellow.

culations is due to Tersoff and Hamann [211], who proposed the following equation:

$$I_t = CV \sum_{n\vec{k}} |\psi_{n\vec{k}}(\vec{r})|^2, \quad (9.1)$$

where the sum is taken over all Kohn-Sham states that fall between  $\epsilon_F$  and  $\epsilon_F + V$ , where  $\epsilon_F$  is the Fermi energy,  $V$  is the potential (in volts) of the sample with respect to the tip,  $\vec{r}$  is the position of the tip's center of curvature (the tip is assumed to be spherical), and  $C$  is a prefactor that in principle depends on the density of states of the tip, surface work function, and radius of the tip. In general, it is simply assumed to be constant. The STM simulation within the Tersoff-Hamann approach then reduces to a calculation of the partial electron density at the position  $\vec{r}$  due to states within the energy window between  $\epsilon_F$  and  $\epsilon_F + V$ .

As one can see from the experimental STM images (see *e.g.* ref. [212] or [213]), the appearance of the clean  $(7 \times 7)$  surface depends strongly on the applied tunneling voltage. At negative sample voltage the filled substrate states contribute to the STM picture and the rest-atoms are observed additionally to the adatoms, while the faulted half unit cell (FHUC) appears a bit brighter. In contrast, at positive sample voltage empty substrate states are probed, only the adatoms are imaged and no height difference is observed. Fig. 9.2 depicts our simulated STM pictures for filled states ( $-2.5$  V, left) and empty states ( $+2.0$  V, right). As can be seen from the Fig. 9.2, these features are nicely reproduced by the calculation.

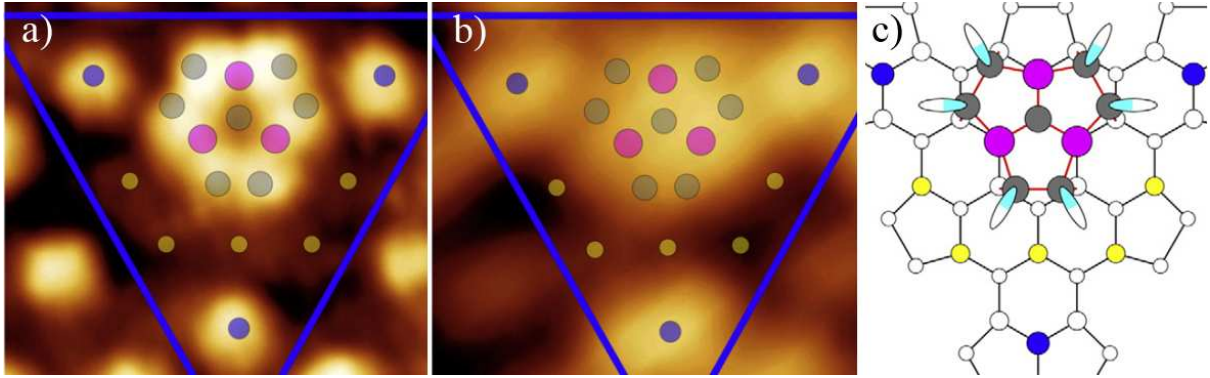


Figure 9.3: Experimental STM image of the empty (a) and filled (b) states of the ring-like clusters together with the suggested structural model (c). Adopted from [202].

## 9.2 Sb/Si Clusters Formation

By means of their STM measurements, Appelfeller, Franz and Dähne observed the formation of self-assembled Sb/Si clusters on the Si(111)-(7 × 7) surface [202]. They showed that with increasing Sb coverage in particular ring-like clusters are formed preferentially in the faulted half of the unit cell, exhibiting a central density depression at the empty states STM images (Fig. 9.3(a)). Based on a careful analysis of the obtained STM pictures, it was concluded that, first, Sb atoms show a high affinity to substitute Si adatoms of the Si(111)-(7 × 7) reconstruction. Second, the ring-like appearance is only observed in the empty states STM images, while filled states images reveal structureless appearances (Fig. 9.3(b)). The average Sb atom content has been estimated to be in the order of five atoms per cluster. On the basis of these data, the following structural model was suggested to explain the observed features: The cluster is assumed to consist of seven Si and three Sb atoms. One Si atom in the symmetry center bonds to three Sb atoms, which are surrounded by three Si dimers. Each of these dimers bonds to two of the Sb atoms. The four central atoms have fully saturated bonds and are in an  $sp^3$ -like bonding configuration, which is the energetically most favorable one (Fig. 9.3(c)).

This structure model can in principle nicely explain the STM images of the ring-like clusters: In empty state images, we mainly observe the partly filled dangling bonds of the outer dimers because they protrude far into the vacuum. In contrast, the empty states at the cluster center are characterized by antisymmetric orbitals of the Sb/Si bonds that are located near the bonding atoms. This leads to a depression in the STM image and therewith to a ring-like appearance. The dangling bonds of the dimers are also seen in filled state STM images, but here the high electron density at the completely filled dangling bonds of the three central Sb atoms leads to a protrusion at the cluster center and thus to a broad, less structured appearance.

To check if the suggested structural model indeed corresponds to the observed STM pictures we first ran global geometry optimization of the respective  $Si_7Sb_3$  cluster ad-

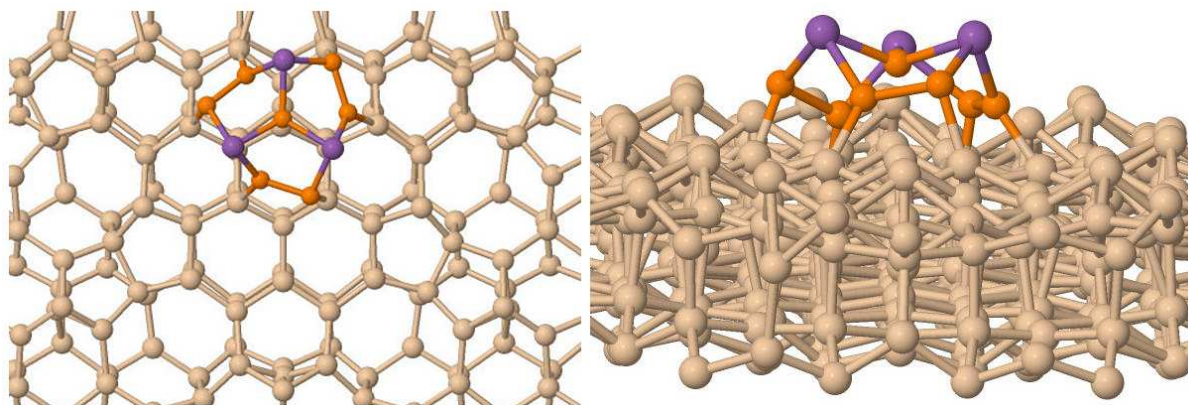


Figure 9.4: Identified ground-state structure of the  $\text{Si}_7\text{Sb}_3$  clusters on the FHUC: Si atoms of the cluster are highlighted in orange, Sb – in purple. Top view (left) and perpendicular view (right).

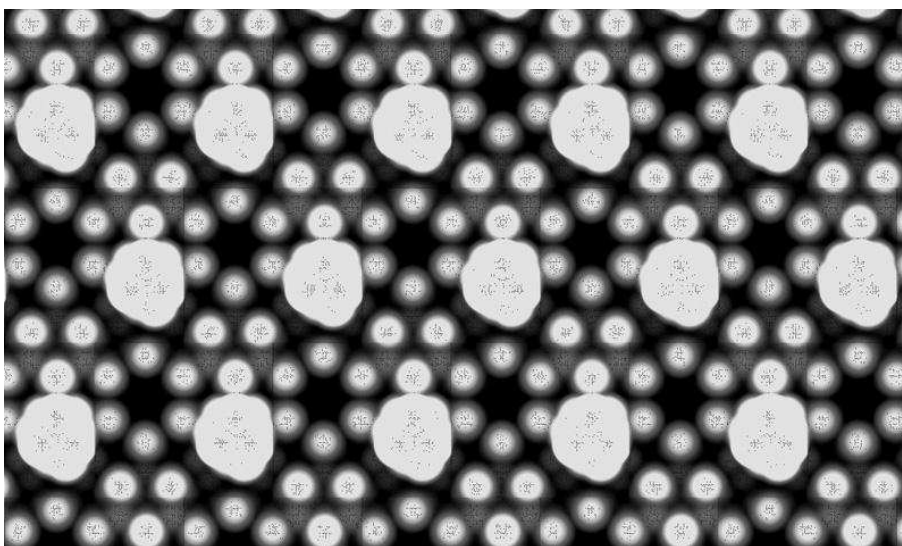


Figure 9.5: Simulated STM picture of the empty states (+1.5 V) of the  $\text{Si}_7\text{Sb}_3$  clusters.

sorbed on the faulted half of the unit cell. The identified ground-state structure is presented in Fig. 9.4.

Analysis of the identified structure shows that, due to the tetrahedral coordination of the fully saturated central Si atom, and due to the high overall number of atoms for the assumed cluster radius, Sb atoms have to be located rather high above the surface. This topographical feature would most likely lead to brighter appearance of these atoms even in the empty states image, thus making the ring-like appearance unlikely. This indeed can be clearly seen in the corresponding simulated STM image (Fig. 9.5).

Thus, additionally taking into account that the number of atoms of both species in the cluster is uncertain, other possible cluster structures have to be suggested. The structure needs to have a number of dangling bonds along the edge of the cluster to yield a bright “ring” in the empty states STM picture, and has to provide the possibility for

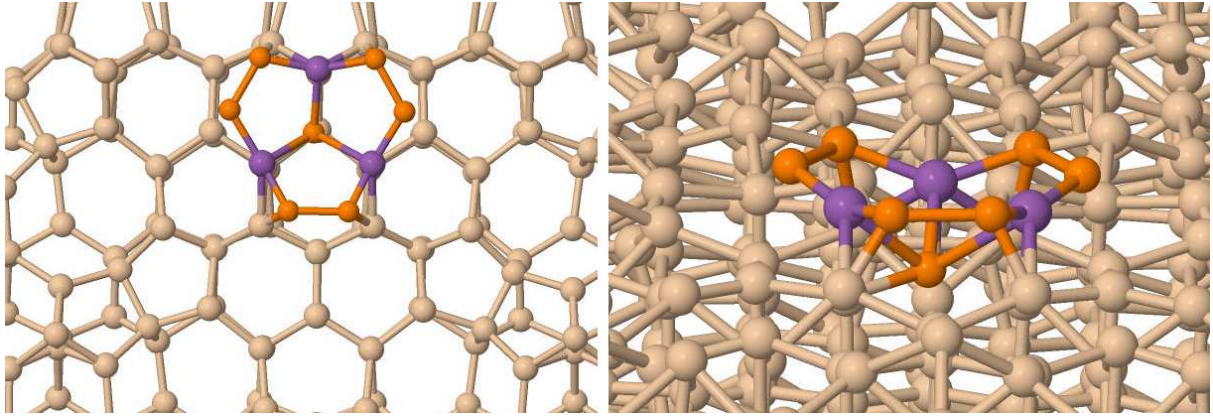


Figure 9.6: Locally optimized structure of the suggested  $\text{Si}_6\text{Sb}_3$  clusters on the FHUC: Si atoms of the cluster are highlighted in orange, Sb – in purple. Top view (left) and perpendicular view (right).

appearance of the density depression in the middle, *i.e.* all bonds of the central atom should be saturated. Additionally the atom should not be located much higher above the surface.

Keeping in mind these constraints, we suggested another structure, similar to the originally proposed one, but with the top central Si atom removed. In such a way, in order to saturate all bonds, Sb atoms have to form a connection with the lower-lying central Si atom. Therefore, Sb atoms should be located lower and somehow closer to the center. At the same time, the very center of the cluster stays “empty”, so the depression in electron density is more likely to be observed. The optimized structure of this newly suggested cluster geometry is presented in Fig. 9.6.

Within this structure, each Sb atom again forms two bonds to the neighboring Si atoms, and the third bond to the central Si atom of the lower layer, and is thus located closer to the surface compared to the originally proposed  $\text{Si}_7\text{Sb}_3$  cluster. This raises hopes for the possibility of a ring-like appearance in the empty states STM picture. Indeed, this time the simulated STM image looks much more like the experimental one. Here, in the empty states picture (Fig. 9.7, on the right) we can see the ring-like appearance similar to the one observed in the experiment. In contrast, in the filled-states image (Fig. 9.7, on the left) we again observe a “density blob”, likely caused by the rather high concentration of Sb electrons in this area.

Intriguingly, varying the number of Sb atoms in this structure (by substituting Si atoms in dimers with Sb one by one), we also managed to reproduce the different apparent heights of the ring-like clusters, observed in experimental STM images, which can be explained by the gradually decreasing number of the Si dangling bonds in the cluster, and the concomitant decrease of the empty states density, which is immediately reflected in the STM picture obtained at positive bias voltage.

The next obvious question is whether the suggested structure corresponds to the

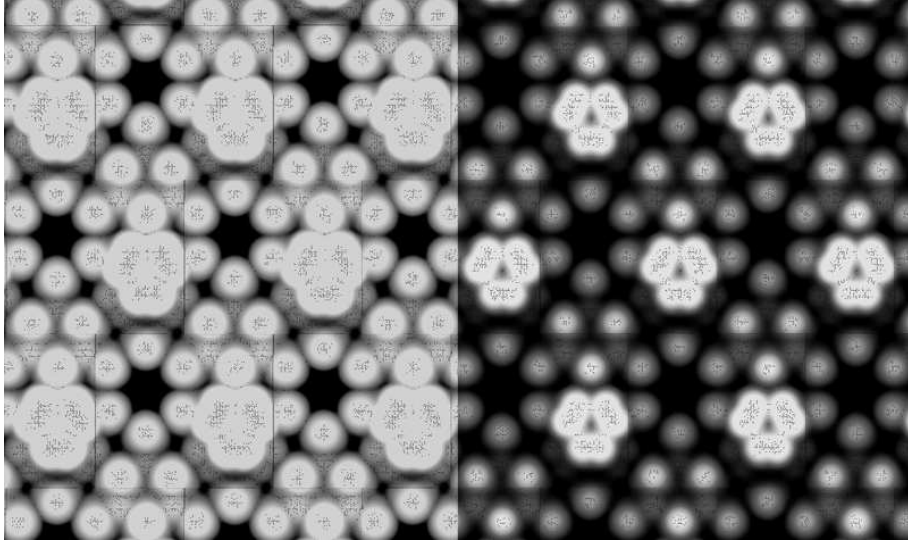


Figure 9.7: Simulated STM picture of the filled ( $-1.5$  V, on left) and empty ( $+1.5$  V, right) states of the  $\text{Si}_6\text{Sb}_3$  clusters.

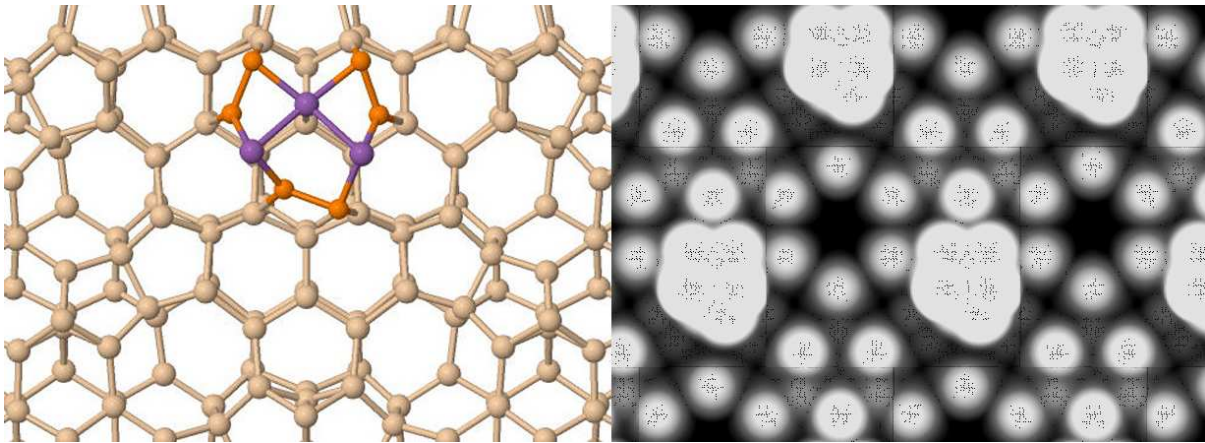


Figure 9.8: Ground state structure of  $\text{Si}_6\text{Sb}_3$  (left) and simulated STM picture of the empty ( $+1.5$  V) states (right).

global minimum or not. Our unbiased systematic sampling revealed that, indeed, for the  $\text{Si}_7\text{Sb}_3$  cluster, the originally suggested structure corresponds to the ground state geometry. However, for the  $\text{Si}_6\text{Sb}_3$  cluster, with the simulated STM image agreeing to the one observed in the experiment, this is not the case. For the latter case we found a less symmetrical structure having a Sb atom in the center to substitute the missing Si to be  $3.04$  eV lower in energy (Fig. 9.8, on the left). Furthermore, this structure has a typical tilting of Si dimers, also observed in the originally proposed structure, as well as for the simple Si(001) surface [216]. Unfortunately, this structure doesn't produce any ring-like appearance in the STM image (Fig. 9.8, on the right). Instead, the obtained simulated STM depicts a featureless high density area similar to the one observed for the originally proposed structure (see Fig. 9.5), due to the high electronic density in the middle of the cluster, and caused by the presence of the central atom in both cases.



### 9.3 Conclusions to Chapter 9

This brings us to a very important conclusion that, since the number of atoms in the cluster is only roughly estimated based on the average Sb coverage and the configuration of bonds within the cluster, even global optimization of the fixed cluster composition, to say nothing about the local geometry relaxation, is not enough for a reliable determination of the experimentally observed structure. Instead, a systematic way of sampling the grand-canonical ensemble of possible cluster compositions has to be suggested in order to efficiently predict the most probable structure. Obviously, a brute-force sampling of all possible Si/Sb combinations is computationally unfeasible, especially taking into account the large number of atoms in the Si(111)-(7 × 7) unit cell, which rises the cost of each geometry relaxation significantly. Instead, the ideas of *ab initio* thermodynamics [42] should be employed to compare the stabilities of clusters of different compositions based on their chemical potentials. Concomitantly, we will be able to sample the ground-state geometries for a wide range of compositions. These ideas are scrutinized within the [next Chapter](#).

# 10 Relative Cluster Stabilities and Beyond

## 10.1 Relative Stability Problem

Quantitative predictive-quality description of relative stabilities of clusters of different sizes and compositions is one of the fundamental challenges the cluster community is currently facing. In general, two approaches are being used to address this problem. The first approach is based on the evaluation of atomization energies with respect to different constituent parts of the system, or, alternatively, with respect to other systems of different sizes. The most widely used formulae were *e.g.* summarized in the paper by Torres *et al.* [143]. For example, to assess relative stabilities of  $MSi_n$  clusters of different sizes one may use the binding (atomization) energy per atom ( $E_b$ ):

$$E_b(MSi_n) = [n \times E(\text{Si}) + E(M) - E(MSi_n)] / (n + 1) . \quad (10.1)$$

Or the addition energy of the  $M$  impurity to a  $Si_n$  cluster ( $E_{\text{add}}^M$ ):

$$E_{\text{add}}^M(MSi_n) = E(Si_n) + E(M) - E(MSi_n) . \quad (10.2)$$

Or the addition energy of a Si atom to a  $MSi_{n-1}$  cluster ( $E_{\text{add}}^{\text{Si}}$ ):

$$E_{\text{add}}^{\text{Si}}(MSi_n) = E(Si_{n-1}) + E(\text{Si}) - E(MSi_n) . \quad (10.3)$$

Or, finally, the so-called “second difference of the cluster energy” ( $\Delta_2 E$ ), which computes the stability of the given cluster with respect to the clusters of adjacent sizes:

$$\Delta_2 E(MSi_n) = E(Si_{n+1}) + E(Si_{n-1}) - 2 \times E(MSi_n) . \quad (10.4)$$

To check if such an approach can be used to compare the relative stabilities of clusters, we have chosen  $\text{TiSi}_{16}$  as a “standard” stable closed-shell cluster, which is well known to exhibit high abundances in mass spectra [152]. Next, we ran global geometry optimizations for a range of Ti-doped clusters ( $\text{TiSi}_n$ ,  $n = 12 - 20$ ), as well as for  $MSi_{16}$  clusters doped with other dopants ( $M = \text{Sc}, \text{Ti}, \text{V}, \text{Cr}$ ). In such a way we can check how responsive the proposed equations are to both differences in size and the number of valence electrons of dopants, which influences the “magicity”, and therewith the stability of the cluster. The resulting total energies of the ground-state structures of the respective clusters were used to calculate their relative stabilities according to the equations above. Results are summarized in Table 10.1.

In a graphical form (for  $\text{TiSi}_n$  clusters) the relative binding energies are depicted in Fig. 10.1. As can be seen from Table 10.1 and Figure 10.1, all four binding energy maxima correspond to the most stable closed-shell  $\text{TiSi}_{16}$  cluster (here the most positive

| Cluster                  | Spin state     | $E_b$ , eV  | $E_{add}^M$ , eV | $E_{add}^{Si}$ , eV | $\Delta_2 E$ , eV |
|--------------------------|----------------|-------------|------------------|---------------------|-------------------|
| TiSi <sub>12</sub>       | singlet        | 3.91        | 5.67             | —                   | —                 |
| TiSi <sub>13</sub>       | singlet        | 3.93        | 6.65             | 4.30                | -0.28             |
| TiSi <sub>14</sub>       | singlet        | 3.98        | 6.53             | 4.57                | -0.38             |
| TiSi <sub>15</sub>       | singlet        | 4.04        | 7.03             | 4.96                | -0.20             |
| ScSi <sub>16</sub>       | doublet        | 3.93        | 5.66             | 5.03                | 1.44              |
| <b>TiSi<sub>16</sub></b> | <b>singlet</b> | <b>4.10</b> | <b>8.62</b>      | <b>5.15</b>         | <b>2.54</b>       |
| VSi <sub>16</sub>        | doublet        | 4.04        | 7.53             | 4.17                | 0.96              |
| CrSi <sub>16</sub>       | singlet        | 3.89        | 5.02             | 2.88                | -1.30             |
| TiSi <sub>17</sub>       | singlet        | 4.02        | 7.83             | 2.61                | -1.07             |
| TiSi <sub>18</sub>       | singlet        | 4.00        | 6.87             | 3.68                | 0.19              |
| TiSi <sub>19</sub>       | singlet        | 3.97        | 7.16             | 3.49                | -0.61             |
| TiSi <sub>20</sub>       | singlet        | 3.98        | 7.11             | 4.10                | —                 |

Table 10.1: Relative stabilities of TiSi<sub>*n*</sub> and MSi<sub>16</sub> clusters, calculated according to eq. (10.1) – (10.4).

energy corresponds to the largest gain in energy, and therefore maximum stability). The suggested values correspond to different properties: stability relative to atomization ( $E_b$ ), energy gained by adding a dopant atom ( $E_{add}^M$ ), energy gained by increasing cluster size ( $E_{add}^{Si}$ ), or relative stability with respect to adjacent smaller and larger cages ( $\Delta_2 E$ ). Nevertheless, they all indicate that TiSi<sub>16</sub> is the most stable cluster both relative to Ti-doped clusters of other sizes, and to MSi<sub>16</sub> clusters with other dopants.

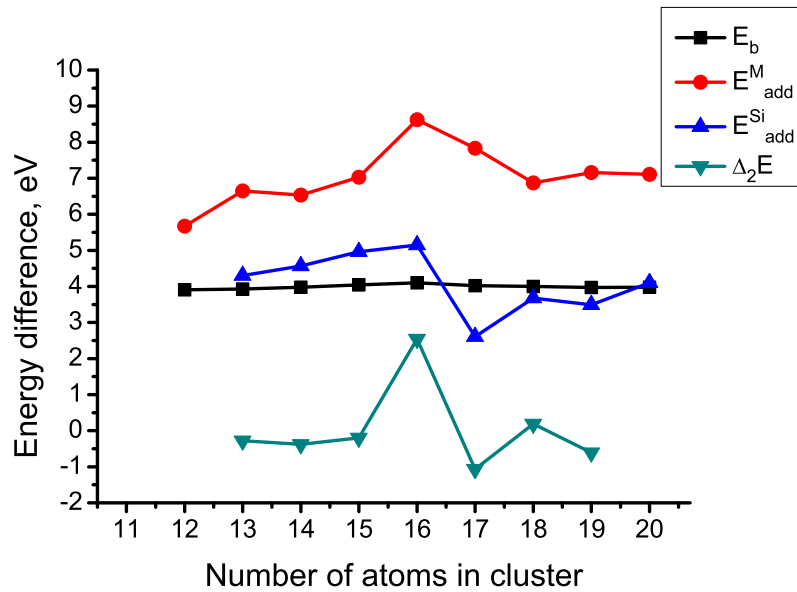


Figure 10.1: Relative stabilities of TiSi<sub>*n*</sub> clusters, calculated according to eq. (10.1) – (10.4).

However, such an approach has its obvious limitations. For example, it is impossible to deduce from these data whether certain cluster sizes are not preferable at all. It is also impossible to extrapolate these data to other cluster sizes and/or compositions. Thus the predictive capabilities of the binding energy idea is rather limited. To improve this, another possible approach to solve the relative stability problem needs to be applied, and we propose the *ab initio* thermodynamics framework.

## 10.2 *Ab initio* Thermodynamics Approach: Basic Idea

Within the *ab initio* thermodynamics idea [42, 124, 125, 214, 215] the central quantity is the Gibbs free energy per particle, which, in case of an infinite homogeneous system, is equivalent to the chemical potential  $\mu$ . If the homogeneous system is viewed as a reservoir, the chemical potential gives the cost at which this reservoir provides particles. For example, such a description is suitable for surface-gas interactions, where infinite homogeneous parts of the system (*i.e.* bulk and surrounding gas phase) can be represented as such reservoirs. In such a fashion, information on structure and energetics from standard DFT calculations can be used to calculate the thermodynamic potential functions, which thus provides a possibility to determine relative stabilities of different configurations by constructing corresponding phase diagrams [123].

This approach has been successfully used for the prediction of thermodynamically stable and metastable structures for bulk semiconductors [42, 125] and surface oxides [217, 218, 219]. Recently it has also been extended to gas-phase clusters in the environment of O<sub>2</sub> and CO [220, 221]. However, in the two latter works only the chemical potentials of the gas-phase O<sub>2</sub> and CO molecules has been taken into account. Thus, to the best of our knowledge, no attempt of translating the *ab initio* thermodynamics ideas to the composition of the cluster itself has been performed so far.

The simplest possible idea of how to assess the stability of a given cluster is to introduce the dependence of the Gibbs free energy of formation  $\Delta G^{\text{form}}$  of *e.g.* the  $MSi_n$  cluster on the chemical potential of its constituent Si atoms ( $\Delta\mu_{\text{Si}}$ ):

$$\Delta G^{\text{form}} = E(MSi_n) - E(M) - n \times E(\text{Si}) - n \times \Delta\mu_{\text{Si}} , \quad (10.5)$$

where  $\Delta\mu_{\text{Si}}$  is an unknown variable chemical potential difference between the Si atom in the formed cluster and in the Si atoms source. Here, we get a linear dependence of  $\Delta G^{\text{form}}$  on  $\Delta\mu_{\text{Si}}$ , and we can analyze the differences in the steepness of the lines corresponding to different cluster sizes: lines that fall lowest in the graph over a range of  $\Delta\mu_{\text{Si}}$  correspond to thermodynamically preferred sizes for this range of  $\Delta\mu_{\text{Si}}$ . As a suitable chemical potential reference point,  $-4.57$  eV can be chosen, which corresponds to the energy difference between the Si atom in Si bulk and an individual Si atom:  $E(\text{Si bulk, per atom}) - E(\text{Si atom})$ , *i.e.* the energy cost of removing one Si atom from

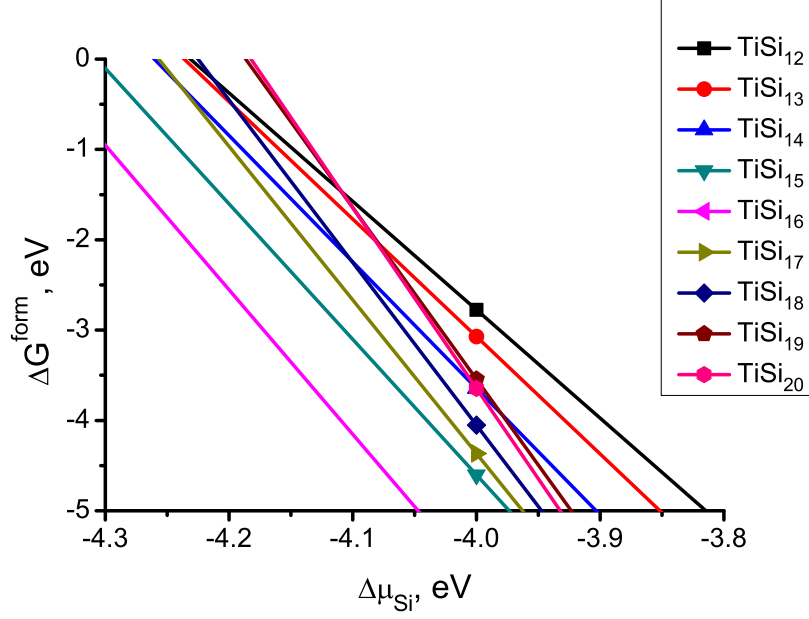


Figure 10.2: Relative stabilities of  $\text{TiSi}_n$  clusters, calculated within the *ab initio* thermodynamics framework according to eq. (10.5).

the bulk. Such choice of reference point can be justified by taking into account that the prevalent experimental method of producing clusters is laser vaporization from the Si surface [222].

Let's plot the lines for  $\text{TiSi}_n$  ( $n = 12 - 20$ ). Here, according to eq. (10.5), a more negative  $\Delta G$  indicates a more stable state of the system. From Fig. 10.2 one can see that, in full agreement with the experimental abundances [152],  $\text{TiSi}_{16}$  is indeed thermodynamically preferred within the range of  $\Delta\mu_{\text{Si}}$  around  $-4$  eV.  $\text{TiSi}_{15}$  is identified as the second most stable cluster size in the relevant range of Si chemical potentials, which also agrees well with experimental data [25].

Analysis of the vibrational contribution to the free energy shows that including the vibrational term to the chemical potential doesn't change the overall picture drastically. We calculate the vibrational contribution as follows:

$$\mu^{\text{ZPE}} = E^{\text{ZPE}} + \mu^{\text{vibr}} = \sum_i \left\{ N_A \frac{\hbar\nu_i}{2} + RT \ln \left[ 1 - \exp \left( \frac{-\hbar\nu_i}{k_B T} \right) \right] \right\}, \quad (10.6)$$

where  $\nu_i$  are vibrational modes,  $N_A$  is Avogadro's constant, and  $R$  is a universal gas constant. The first term ( $E^{\text{ZPE}}$ ) arises from the zero-point vibrations (giving a contribution of the order of  $+0.6$  eV at 298 K for  $\text{TiSi}_n$  clusters) and the second term corresponds to the free energy contributions of all vibrational modes ( $\sim -0.4$  eV, 298 K). In total this gives an average of  $\sim +0.2$  eV, which shifts all lines in the spectrum more or less systematically to less negative  $\Delta G$  (due to larger positive ZPE term). Obviously, the relative positions of the lines do not change. For higher temperatures, the contribution of

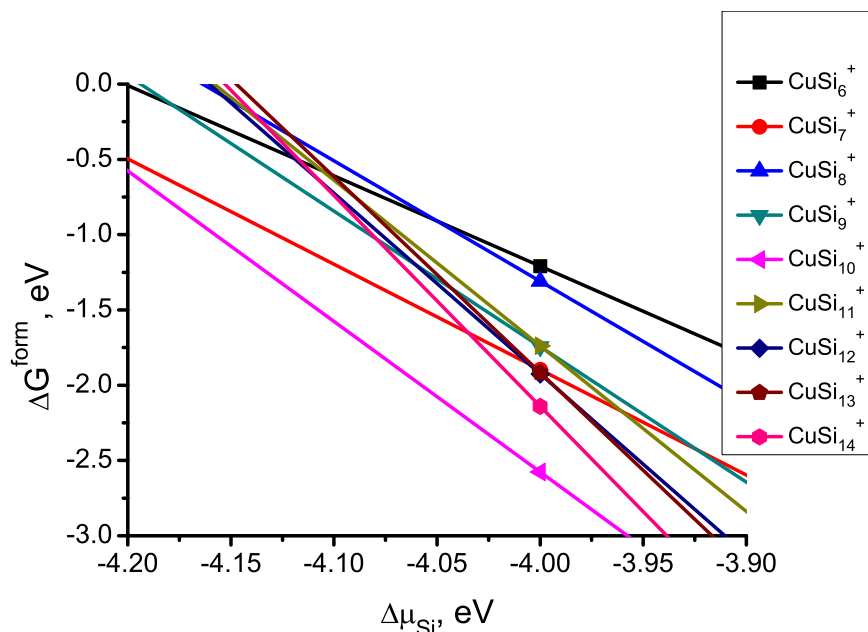


Figure 10.3: Relative stabilities of  $\text{CuSi}_n^+$  clusters, calculated within the *ab initio* thermodynamics framework according to eq. (10.5).

the second term should increase, giving an overall shift of the graph to the other direction (to more negative  $\Delta G$ ).

Very similar agreement between the experimental mass-spectrometry data [23] and our calculated results (*cf.* Fig. 10.3) is also observed for cationic  $\text{CuSi}_n^+$  clusters. As observed in the experiment [23],  $\text{CuSi}_{10}^+$  is the preferred cluster size. Both  $\text{CuSi}_7^+$  and  $\text{CuSi}_9^+$  appear as second and third most stable structures, respectively, within a certain range of chemical potentials (around  $-4.10$  eV). These results confirm that the method works for both neutral and cationic clusters, and is valid for clusters with different dopants.

### 10.3 Towards the True Thermodynamics

The above described method thus illustrates the fundamental possibility of employing the concept of chemical potential of constituent atoms for the assessment of relative stabilities of clusters. The main problem of the method, however, is the fact that the chemical potential is not computed explicitly, which leaves the precise range of relevant  $\Delta\mu_{\text{Si}}$  to understand a given experiment unknown. The total free energy of the given cluster is composed of electronic, vibrational (see eq. (4.24)), translational (eq. (4.13)) and rotational (eq. (4.20)) free energy contributions (there are no internal rotations in

the clusters under consideration):

$$G(T, p) = G(\text{electr.}) + \sum_i \left\{ N_A \frac{\hbar \nu_i}{2} + RT \ln \left[ 1 - \exp \left( \frac{-\hbar \nu_i}{k_B T} \right) \right] \right\} - RT \ln \left( \frac{(2\pi k_B T m)^{3/2}}{h^3} \cdot \frac{k_B T}{p} \right) - RT \ln \left[ \frac{8\pi^2}{\sigma} \left( \frac{2\pi k_B T}{h^2} \right)^{3/2} \cdot (I_A I_B I_C)^{1/2} \right], \quad (10.7)$$

with the first term of the vibrational free energy accounting for zero-point vibrations.

The translational, rotational and vibrational contributions are easily calculated from the structural data (globally optimized ground-state geometry of the cluster) and the calculated vibrational spectrum according to eq. (10.7). The  $G(\text{electr.})$  term is then equal to the calculated total energy of the cluster. From this, the chemical potential of the Si atom in the given cluster can be calculated by definition as the “cost” of the particle, *i.e.* as the increment of the free energy over the increment of the number of particles:

$$\mu_{\text{Si}} = \frac{\partial G}{\partial n_{\text{Si}}} \approx \frac{G(M\text{Si}_n) - G(M\text{Si}_{n-1})}{1} \quad (10.8)$$

where  $M\text{Si}_n$  is a given cluster size. Let’s calculate these values for a set of  $\text{TiSi}_n$  ( $n = 12 - 20$ ) clusters (for  $T = 298$  K,  $p = 1$  atm) and compare them to the energies of an individual Si atom and Si atom in Si bulk (see Table 10.2).

| Cluster                  | G(el.),<br>10 <sup>5</sup> eV | G(tr.),<br>eV | G(rot.),<br>eV | G(vibr.),<br>eV | $\mu_{\text{Si}}$ , eV | $\Delta\mu_{\text{atom}}$ ,<br>eV | $\Delta\mu_{\text{bulk}}$ ,<br>eV |
|--------------------------|-------------------------------|---------------|----------------|-----------------|------------------------|-----------------------------------|-----------------------------------|
| TiSi <sub>12</sub>       | -1.1793                       | -0.5011       | -0.3673        | 0.2315          | —                      | —                                 | —                                 |
| TiSi <sub>13</sub>       | -1.2582                       | -0.5038       | -0.3671        | 0.2100          | -7891.9037             | 4.32                              | -0.25                             |
| TiSi <sub>14</sub>       | -1.3371                       | -0.5064       | -0.3705        | 0.2442          | -7892.1273             | 4.55                              | -0.02                             |
| TiSi <sub>15</sub>       | -1.4161                       | -0.5087       | -0.3735        | 0.2441          | -7892.5422             | 4.96                              | 0.39                              |
| <b>TiSi<sub>16</sub></b> | -1.4950                       | -0.5110       | -0.3761        | 0.1881          | -7892.7931             | <b>5.21</b>                       | <b>0.64</b>                       |
| TiSi <sub>17</sub>       | -1.5739                       | -0.5131       | -0.3825        | 0.2243          | -7890.1676             | 2.59                              | -1.98                             |
| TiSi <sub>18</sub>       | -1.6528                       | -0.5151       | -0.3875        | 0.2246          | -7891.2730             | 3.69                              | -0.88                             |
| TiSi <sub>19</sub>       | -1.7317                       | -0.5170       | -0.3923        | 0.2558          | -7891.0513             | 3.47                              | -1.10                             |
| TiSi <sub>20</sub>       | -1.8106                       | -0.5188       | -0.3966        | 0.3215          | -7891.6231             | 4.04                              | -0.53                             |

Table 10.2: Calculated chemical potentials of Si atoms in  $\text{TiSi}_n$  clusters.

As can be seen from Table 10.2, Si atoms in  $\text{TiSi}_{16}$  indeed have the most negative chemical potential, which indicates stability of the cluster. The difference between the chemical potentials of a Si atom in the cluster and an individual Si atom (see the  $\Delta\mu_{\text{atom}}$  column in the Table 10.2) are very close to values of the addition energy of Si atom to a  $M\text{Si}_{n-1}$  obtained through the eq. (10.3). The comparison with the bulk atoms

is, however, more interesting. While similarly indicating that the  $\text{TiSi}_{16}$  cluster is the most stable one, the  $\Delta\mu_{\text{bulk}}$  column of Table 10.2 clearly shows that only  $\text{TiSi}_{16}$  and  $\text{TiSi}_{15}$  should be stable at all with respect to the bulk Si, which agrees very well with experimental mass-spectra [25, 152].

Similar results have also been obtained for  $\text{CuSi}_n^+$  ( $n = 6 - 14$ ) clusters (see Table 10.3).

| Cluster                                | G(el.),<br>$10^5$ eV | G(tr.),<br>eV | G(rot.),<br>eV | G(vibr.),<br>eV | $\mu_{\text{Si}}$ , eV | $\Delta\mu_{\text{atom}}$ ,<br>eV | $\Delta\mu_{\text{bulk}}$ ,<br>eV |
|--|----------------------|---------------|----------------|-----------------|------------------------|-----------------------------------|-----------------------------------|
| $\text{CuSi}_6^+$                      | -0.9237              | -0.5089       | -0.3567        | 0.0288          | —                      | —                                 | —                                 |
| $\text{CuSi}_7^+$                      | -1.0026              | -0.5133       | -0.3694        | 0.1179          | -7892.1970             | 4.62                              | 0.05                              |
| $\text{CuSi}_8^+$                      | -1.0816              | -0.5173       | -0.3728        | 0.1093          | -7891.0104             | 3.43                              | -1.14                             |
| $\text{CuSi}_9^+$                      | -1.1605              | -0.5209       | -0.3785        | 0.1143          | -7892.0195             | 4.44                              | -0.13                             |
| <b><math>\text{CuSi}_{10}^+</math></b> | -1.2394              | -0.5242       | -0.3863        | 0.1115          | -7892.4281             | <b>4.85</b>                       | <b>0.28</b>                       |
| $\text{CuSi}_{11}^+$                   | -1.3183              | -0.5272       | -0.3912        | 0.1504          | -7890.7122             | 3.13                              | -1.44                             |
| $\text{CuSi}_{12}^+$                   | -1.3972              | -0.5300       | -0.3980        | 0.1406          | -7891.7884             | 4.21                              | -0.36                             |
| $\text{CuSi}_{13}^+$                   | -1.4761              | -0.5326       | -0.4001        | 0.1621          | -7891.5548             | 3.97                              | -0.60                             |
| $\text{CuSi}_{14}^+$                   | -1.5551              | -0.5351       | -0.4049        | 0.2295          | -7891.7458             | 4.14                              | -0.41                             |

Table 10.3: Calculated chemical potentials of Si atoms in  $\text{CuSi}_n^+$  clusters.

As can be seen from the Table 10.3,  $\text{CuSi}_{10}^+$  is the most stable cluster, which agrees well with the experimental results [23]. At the same time, only in case of  $\text{CuSi}_7^+$  and  $\text{CuSi}_9^+$  clusters Si atoms come close in energy to a Si atom in Si bulk, which also agrees nicely with experimental mass-spectra depicting three major peaks indicating the highest abundances for  $\text{CuSi}_{10}^+$ ,  $\text{CuSi}_7^+$  and  $\text{CuSi}_9^+$ , respectively [23].

## 10.4 Conclusions to Chapter 10

First results indicate that a thermodynamics-based approach allows to reproduce mass-spectra abundances of clusters of different sizes rather well. However, there are still several challenging questions left to be answered. First of all, the mixture of clusters produced in the laser vaporization source might be in a non-equilibrium state. Second, there is still no way to extrapolate the results to clusters of other sizes, due to a non-linear dependence of  $\mu_{\text{Si}}$  on the cluster size. Since these questions go beyond the scope of this thesis, we emphasize the importance and potential applicability of an *ab initio* thermodynamics approach to assess the cluster stabilities, and outline this as an perspective outlook, with the goal of pursuing these investigations in our future work.



## 11 General Conclusions and Outlook

The results obtained within this work clearly indicate the unique position of silicon clusters among the family of potential building block candidates to be used for novel engineered nano-scale material design. Despite the common belief in simple electron counting rules [27, 143, 152] and a formal charge transfer picture [16, 140, 141, 142], endohedrally doped Si cage-like clusters are shown to be stabilized through complex dopant-cage interaction, mediated *via* hybridized metal-Si states (Chapter 5). This, on the one hand, offers more flexibility in obtaining stable endohedrally doped systems, not only limited to the ones with “magic” number of electrons, while, on the other hand, simultaneously suggesting the possibility of conserving the atomic character of the dopant by minimizing the dopant-cage interaction. For instance, such minimization can be achieved by hydrogen termination of the  $sp^3$ -caused dangling bonds of the cage Si atoms [155, 156]. In this line of thinking, Chapter 6 illustrated the possibility of conserving the high spin states of individual transition metal dopant atoms, with stabilization of the structure achieved by delocalization of dopant 4s electrons, instead of hybridization of its unpaired valence  $d$ -electrons. Intriguingly, this method not only protects the cluster from the reactive environment, but already suggests a route to polymerization of such hydrogenated clusters by varying the number of non-terminated Si dangling bonds, thus transforming the individual gas-phase clusters into appealing building blocks for novel cluster-assembled materials [9]. Chapter 7 reveals that, in contrast to the known clathrate-type facet sharing, such hydrogenated Si cage building blocks show a predisposition to aggregation through double Si-Si bridge bonds. This yields a toolbox of monomers with different number of double “docking sites”, which allows building thermodynamically stable network architectures of any morphology. These properties differentiate Si cage-like clusters from their “conventional” carbon fullerene counterparts, for which, due to preferable  $sp^2$  hybridization, the controlled formation of a given number of bonding sites appears to be improbable. Moreover, such Si-based building blocks for cluster-assembled materials may possess unique magnetic properties, as was illustrated in Chapter 8, confirming the exciting perspective of tuning the total number of unpaired electrons in the system by encapsulating a range of different dopants (starting from single atoms with different spin states, through highly magnetic dimers, and eventually up to more complex dopant aggregates) into a suitably sized hydrogenated silicon cage.

In conclusion, the work thus systematically assessed the possibility of using Si clusters in the growing field of nano-material science by carefully investigating the nature of chemical bonding within the building blocks and suggesting novel ways of building aggregates with engineered properties. On a conceptual level this work underscores the necessity of basing nanoscale materials design through predictive-quality theory on a systematic unbiased exploration of the vast configurational space with global optimization meth-

ods such as basin-hopping [36], as opposed to simple comparisons of chemically intuitive candidate structures.

However, as is true for any extensive scientific investigation, here we also raise new questions to be answered in future projects. The central problem of any cluster investigation is to move from the study of isolated, individual metal-doped Si clusters towards the properties of such clusters in a non-trivial environment, *i.e.* under the influence of other bonding partners (clusters, extended surfaces). Specifically targeted within this theme is the formation of aggregates as first step towards bulk cluster-assembled materials on the one hand, and the stabilization of doped Si cages at Si or/and graphene surfaces on the other hand.

With our work we have already taken a first step towards aggregates formed of several endohedral Si cages. At the concomitantly increased system sizes and complexity extensive configurational sampling becomes ever the more important to arrive at reliable conclusions concerning the preferred geometric structures adopted. However, in its classic formulation global geometry optimization samples for a fixed number of species, *i.e.* it only identifies the optimum structure for a defined composition. One avenue to overcome this limitation is to extend the configurational sampling to a grand-canonical ensemble within the *ab initio* thermodynamics [123] framework, the idea of which was already touched upon in Chapter 10. In addition to the regular trial moves that merely change the geometric position of atoms, this would allow for particle insertion or deletion moves, or even “alchemical” moves changing the chemical species. The target function to minimize would then no longer be the total energy, but instead the Gibbs free energy as evaluated within *ab initio* thermodynamics. For given chemical potentials such simulations would then ideally converge automatically towards the optimal cluster size/composition.

Another important question here that is of big relevance for real-life synthetic prospects of cluster-assembled materials is how stable the building blocks, intermediates and the final aggregates themselves are in reaction solution. Suitable solvents might include those used for synthesis of organosilicon clusters [223, 224], such as toluene or tetrahydrofuran. For this, simulation of the environment *e.g.* within an implicit solvation model [225, 226, 227] is needed.

As an obvious alternative route to make the intriguing materials properties of metal-doped Si clusters available in applications, investigation of their stabilization at extended surfaces is furthermore necessary. Experimentally this can be realized through deposition of pre-formed cages or through silicide formation at the surface, which was outlined in Chapter 9. The central question here is a balanced cage-surface interaction that is strong enough to lead to a desired fixation of the cage, but not too strong to jeopardize its geometric integrity. Obviously, this also calls in a first step for a dedicated exploration of the configurational space to identify which structures result as most stable. The additional computational challenge here is the increased cost of global geometry optimizations

incurred by the necessity to explicitly model the extended surface. Therefore, the possibility of pre-screenings at lower levels of theory should be taken into account. This comprises, for instance, the detailed validation of the reliability of tight-binding DFT [47, 48] and of semi-empirical potentials [228, 229].

Another potentially interesting question for future investigations is how the interplay between adsorption of simple gas-phase molecules and doping may be employed to fine-tune the function of silicon clusters. The main objective here is to use the obtained detailed geometric, energetic and electronic structure data to establish a trend understanding of stable adsorbate/dopant combinations with interesting materials properties.

Ultimately, despite the wealth of newly arising questions, the here presented approaches for novel material construction can be applied to a broad range of systems, not limited to silicon clusters. This, for instance, includes systematic unbiased configurational sampling of the system composition, careful study of the chemical bonding within the structure, with a specific focus on the dopant-host interaction, which can be tuned and configured to meet the needs of the material design, and a comprehensive description of the ways to obtain unique magnetic and optical properties of the constructed material. This work thus provides important insights into theoretical material design, and, hopefully, will stimulate further investigations in the field.



# Appendix

## A Basis Sets used in FHI-aims

|         | H   | Si   | Cr  | Sb  |
|---------|---|--|---|---|
| minimal | $1s^1$  | $[Ne] + 3s^23p^2$  | $[Ar] + 4s^23d^4$   | $[Kr] + 5s^24d^{10}5p^3$  |
| tier 1  | H(2 <i>s</i> , 2.1)<br>H(2 <i>p</i> , 3.5)  | H(3 <i>d</i> , 4.2)<br>H(2 <i>p</i> , 1.4)<br>H(4 <i>f</i> , 6.2)<br>Si <sup>2+</sup> (3 <i>s</i> )                        | H(4 <i>f</i> , 9.6)<br>H(3 <i>d</i> , 3.1)<br>Cr <sup>2+</sup> (4 <i>p</i> )<br>H(5 <i>g</i> , 13.6)<br>Cr <sup>2+</sup> (4 <i>s</i> )  | H(3 <i>d</i> , 3.5)<br>Sb <sup>2+</sup> (5 <i>p</i> )<br>H(4 <i>f</i> , 6.8)<br>Sb <sup>2+</sup> (5 <i>s</i> )  |
| tier 2  | H(1 <i>s</i> , 0.85)<br>H(2 <i>p</i> , 3.7)<br>H(2 <i>s</i> , 1.2)<br>H(3 <i>d</i> , 7.0) | H(3 <i>d</i> , 9.0)<br>H(5 <i>g</i> , 9.4)<br>H(4 <i>p</i> , 4.0)<br>H(1 <i>s</i> , 0.65)                                  | H(4 <i>f</i> , 6.8)<br>H(4 <i>d</i> , 14.4)<br>H(6 <i>h</i> , 19.2)<br>Cr <sup>2+</sup> (3 <i>d</i> )<br>H(4 <i>f</i> , 14.8)<br>H(5 <i>g</i> , 10.4)<br>H(1 <i>s</i> , 0.6)<br>H(3 <i>p</i> , 3.5) | H(5 <i>g</i> , 9.8)<br>H(4 <i>f</i> , 19.2)<br>H(6 <i>h</i> , 13.6)<br>H(4 <i>d</i> , 4.5)<br>H(4 <i>f</i> , 4.6)<br>H(5 <i>p</i> , 7.0)<br>H(3 <i>s</i> , 2.7) |
| tier 3  | H(4 <i>f</i> , 11.2)<br>H(3 <i>p</i> , 4.8)<br>H(4 <i>d</i> , 9.0)<br>H(3 <i>s</i> , 3.2) | Si <sup>2+</sup> (3 <i>d</i> )<br>H(3 <i>s</i> , 2.6)<br>H(4 <i>f</i> , 8.4)<br>H(3 <i>d</i> , 3.4)<br>H(3 <i>p</i> , 7.8) | H(6 <i>h</i> , 15.6)<br>H(3 <i>d</i> , 7.4)<br>H(4 <i>p</i> , 18.4)<br>H(5 <i>g</i> , 16.4)<br>H(4 <i>s</i> , 3.9)<br>H(4 <i>f</i> , 28.8)  | H(6 <i>p</i> , 7.8)<br>H(5 <i>g</i> , 8.6)<br>H(6 <i>h</i> , 11.6)<br>H(5 <i>f</i> , 16.4)<br>H(5 <i>d</i> , 8.4)<br>H(1 <i>s</i> , 0.7)                        |
|         | ...   | ...  | ...   | ...   |

Table A.1: Radial basis functions used in FHI-aims for several example atoms (H as *s*-element, Si as *p*-element, Cr as *d*-metal, and Sb as *p*-metal).  $H(nl, z)$  denotes a hydrogen-like basis function for the bare Coulomb potential  $z/r$ , including its radial and angular momentum quantum numbers  $n$  and  $l$ .  $X^{2+}$  denotes a radial function of a doubly positive free ion of species  $X$ .

## B Low-lying Isomers of Selected Clusters

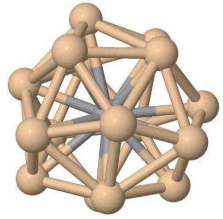
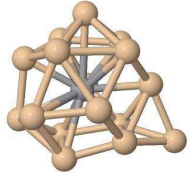
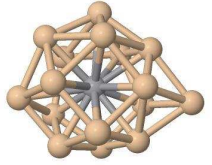
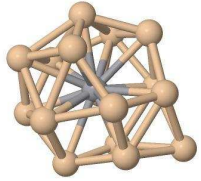
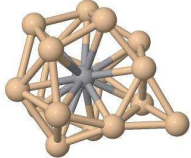
| VSi <sub>16</sub> <sup>+</sup> |            |                     |   |
|--------------------------------|------------|---------------------|---|
| Isomer number                  | Spin state | Relative energy, eV | Picture   |
| 1                              | singlet    | 0.00                |    |
| 2                              | singlet    | 1.00                |    |
| 3                              | singlet    | 1.05                |   |
| 4                              | singlet    | 1.11                |  |
| 5                              | singlet    | 1.15                |  |

Table B.1: VSi<sub>16</sub><sup>+</sup> low-lying isomers.

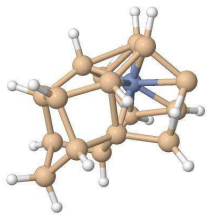
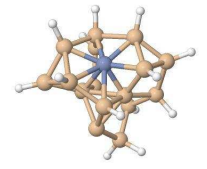
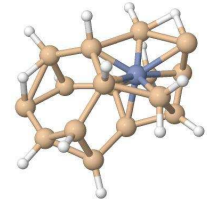
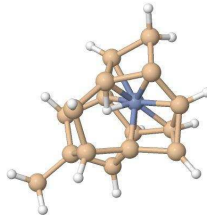
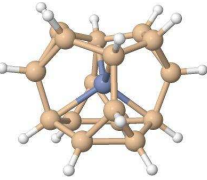
| CrSi <sub>16</sub> H <sub>16</sub> |            |                     |   |
|------------------------------------|------------|---------------------|---|
| Isomer number                      | Spin state | Relative energy, eV | Picture   |
| 1                                  | singlet    | 0.00                |    |
| 2                                  | singlet    | 1.50                |    |
| 3                                  | singlet    | 1.55                |  |
| 4                                  | singlet    | 1.66                |  |
| cage                               | septet     | 2.14                |  |

Table B.2: CrSi<sub>16</sub>H<sub>16</sub> low-lying isomers.



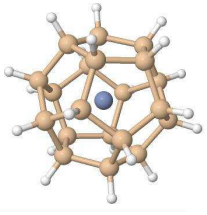
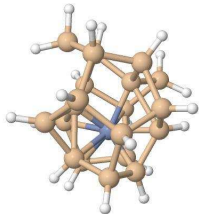
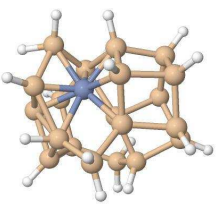
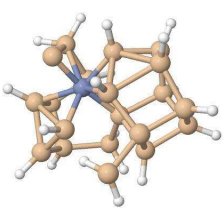
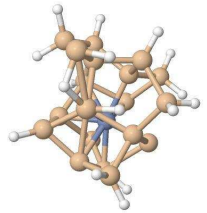
| CrSi <sub>20</sub> H <sub>20</sub> |            |                     |   |
|------------------------------------|------------|---------------------|---|
| Isomer number                      | Spin state | Relative energy, eV | Picture   |
| 1                                  | septet     | 0.00                |    |
| 2                                  | singlet    | 2.05                |    |
| 3                                  | singlet    | 2.69                |  |
| 4                                  | singlet    | 4.81                |  |
| 5                                  | singlet    | 5.16                |  |

Table B.3: CrSi<sub>20</sub>H<sub>20</sub> low-lying isomers.

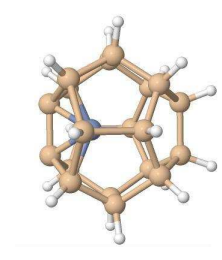
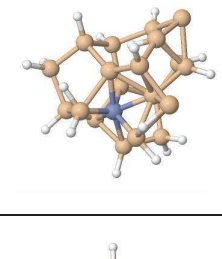
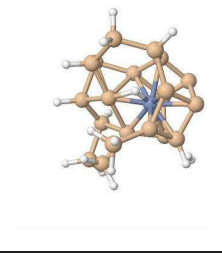
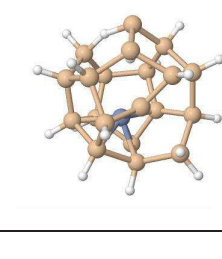
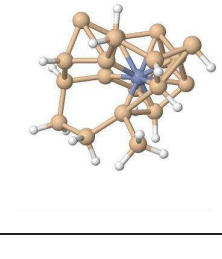
| CrSi <sub>20</sub> H <sub>18</sub> |            |                     |   |
|------------------------------------|------------|---------------------|---|
| Isomer number                      | Spin state | Relative energy, eV | Picture   |
| 1                                  | singlet    | 0.00                |    |
| 2                                  | singlet    | 1.95                |   |
| 3                                  | singlet    | 2.00                |  |
| 4                                  | singlet    | 2.14                |  |
| 5                                  | singlet    | 2.23                |  |

Table B.4: CrSi<sub>20</sub>H<sub>18</sub> monomer low-lying isomers.

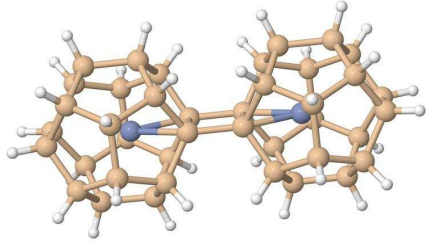
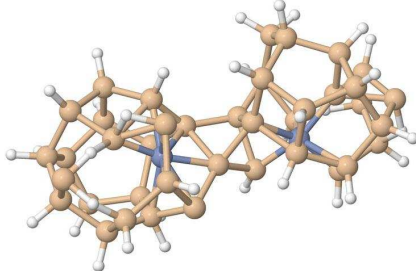
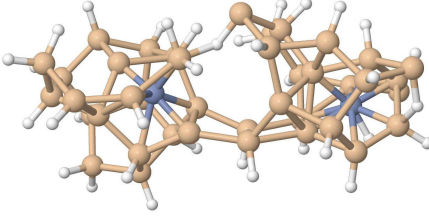
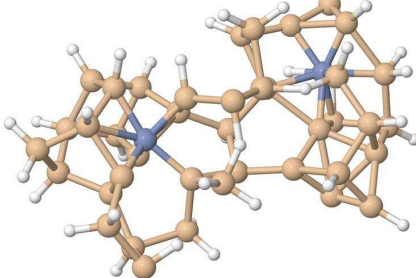
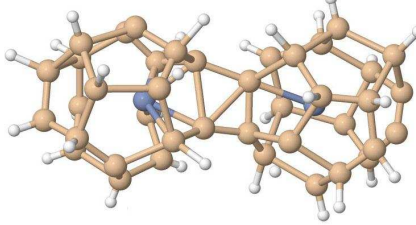
| $(\text{CrSi}_{20}\text{H}_{18})_2$ |            |                     |  |
|-------------------------------------|------------|---------------------|--|
| Isomer number                       | Spin state | Relative energy, eV | Picture  |
| 1                                   | singlet    | 0.00                |    |
| 2                                   | singlet    | 6.63                |    |
| 3                                   | singlet    | 6.95                |  |
| 4                                   | singlet    | 9.15                |  |
| 5                                   | singlet    | 10.23               |  |

Table B.5:  $(\text{CrSi}_{20}\text{H}_{18})_2$  dimer low-lying isomers.

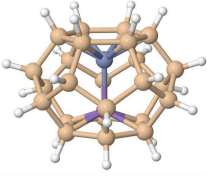
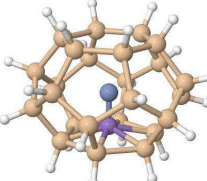
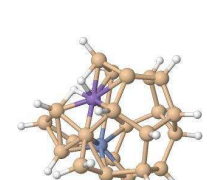
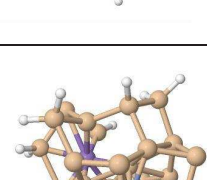
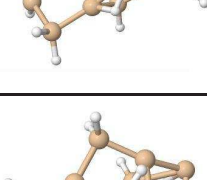
| CrMn <sup>+</sup> @CrSi <sub>24</sub> H <sub>24</sub> |            |                     |   |
|---|------------|---------------------|---|
| Isomer number   | Spin state | Relative energy, eV | Picture   |
| 1   | 11-tet     | 0.00                |    |
| 2   | singlet    | 0.80                |    |
| 3   | singlet    | 4.29                |   |
| 4   | singlet    | 4.54                |  |
| 5   | singlet    | 4.82                |  |

Table B.6: CrMn<sup>+</sup>@CrSi<sub>24</sub>H<sub>24</sub> low-lying isomers.

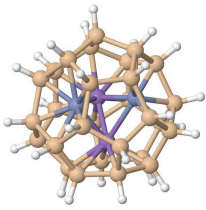
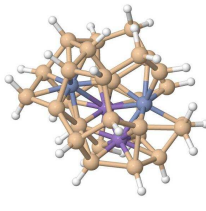
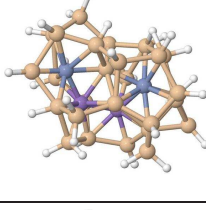
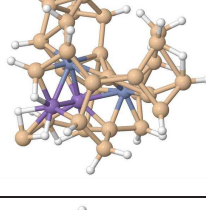
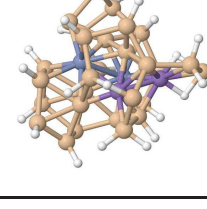
| $(\text{CrMn}^+)_2@ \text{CrSi}_{28}\text{H}_{28}$ |            |                     |   |
|--|------------|---------------------|---|
| Isomer number                                      | Spin state | Relative energy, eV | Picture   |
| 1  | 19-tet     | 0.00                |    |
| 2  | singlet    | 0.75                |   |
| 3  | singlet    | 1.11                |  |
| 4  | singlet    | 4.00                |  |
| 5  | singlet    | 4.42                |  |

Table B.7:  $(\text{CrMn}^+)_2@ \text{CrSi}_{28}\text{H}_{28}$  low-lying isomers.



## References

- [1] R. L. Johnston, “*Atomic and Molecular Clusters*”, Taylor & Francis, London, 2002, ISBN: [0-748-40930-0](#), (cit. on p. [1](#), [77](#)).
- [2] H. H. Anderson (Ed.), “*Small Particles and Inorganic Clusters*”, Springer, New York, 1997, ISBN: [3-540-63157-7](#), (cit. on p. [1](#)).
- [3] S. N. Khanna, A. W. Castleman, Jr. (Eds.), “*Quantum Phenomena in Clusters and Nanostructures*”, Springer, New York, 2003, ISBN: [3-540-00015-1](#), (cit. on p. [1](#)).
- [4] K. Sattler (Ed.), “*Cluster Assembled Materials*”, Trans Tech Publications, Zurich, 1996, ISBN: [0-878-49747-1](#), (cit. on p. [1](#)).
- [5] P. Braunstein, L. A. Oro, P. R. Raithby (Eds.), “*Metal Clusters in Chemistry*”, Wiley-VCH, Weinheim, 1999, ISBN: [3-527-29549-6](#), (cit. on p. [1](#)).
- [6] A. Perez, P. Melinon, V. Dupuis, P. Jensen, B. Prevel, J. Tuaille, L. Bardotti, C. Martet, M. Treilleux, M. Broyer, M. Pellarin, J. L. Vaille, B. Palpant, J. Lerme, “*Cluster Assembled Materials: A Novel Class of Nanostructured Solids with Original Structures and Properties*”, J. Phys. D: Appl. Phys. **30**, 709 (1997), DOI: [10.1088/0022-3727/30/5/003](#), (cit. on p. [1](#)).
- [7] P. Jena, S. N. Khanna, B. K. Rao (Eds.), “*Clusters and Nano-Assemblies*”, World Scientific, New York, 2005, ISBN: [9-812-56331-8](#), (cit. on p. [1](#)).
- [8] A. W. Castleman, S. N. Khanna, “*Clusters, Superatoms, and Building Blocks of New Materials*”, J. Phys. Chem. C **113**, 2664 (2009), DOI: [10.1021/jp806850h](#), (cit. on p. [1](#)).
- [9] S. A. Claridge, A. W. Castleman, Jr., S. N. Khanna, C. B. Murray, A. Sen, P. S. Weiss, “*Cluster-Assembled Materials*”, ACS Nano **3**, 244 (2009), DOI: [10.1021/nm800820e](#), (cit. on p. [1](#), [93](#)).
- [10] C. M. Lieber, C.-C. Chen, “*Preparation of Fullerenes and Fullerene-Based Materials*”, Solid State Physics **48**, 109 (1994), DOI: [10.1016/S0081-1947\(08\)60578-0](#), (cit. on p. [1](#)).
- [11] L. Forró, L. Mihály, “*Electronic Properties of Doped Fullerenes*”, Rep. Prog. Phys. **64**, 649 (2001), DOI: [10.1088/0034-4885/64/5/202](#), (cit. on p. [1](#)).
- [12] M. Qian, S. V. Ong, S. N. Khanna, M. B. Knickelbein, “*Magnetic Endohedral Metallofullerenes with Floppy Interiors*”, Phys. Rev. B **75**, 104424 (2007), DOI: [10.1103/PhysRevB.75.104424](#), (cit. on p. [1](#)).
- [13] K. Sato, M. Kako, M. Suzuki, N. Mizorogi, T. Tsuchiya, M. M. Olmstead, A. L. Balch, T. Akasaka, S. Nagase, “*Synthesis of Silylene-Bridged Endohedral Metallofullerene  $Lu_3N@I_h-C_{80}$* ”, J. Am. Chem. Soc. **134**, 16033 (2012), DOI: [10.1021/ja3073929](#), (cit. on p. [1](#), [30](#), [62](#)).
- [14] E. Wiberg, N. Wiberg, A. Holleman, “*Inorganic Chemistry*”, Academic Press, San Diego, 2001, ISBN: [0-123-52651-5](#), (cit. on p. [1](#)).

## References

- [15] Q. Sun, Q. Wang, T. M. Briere, V. Kumar, Y. Kawazoe and P. Jena, “*First-principles calculations of metal stabilized  $Si_{20}$  cages*”, Phys. Rev. B. **65**, 235417 (2002), DOI: [10.1103/PhysRevB.65.235417](https://doi.org/10.1103/PhysRevB.65.235417), (cit. on p. 1, 30).
- [16] K. Jackson and B. Nellermoe, “*Zr@Si<sub>20</sub>: a Strongly Bound Si Endohedral System*”, Chem. Phys. Lett. **254**, 249 (1996), DOI: [10.1016/0009-2614\(96\)00315-6](https://doi.org/10.1016/0009-2614(96)00315-6), (cit. on p. 2, 30, 31, 34, 93).
- [17] H. Hiura, T. Miyazaki, T. Kanayama, “*Formation of Metal-Encapsulating Si Cage Clusters*”, Phys. Rev. Lett. **86**, 1733 (2001), DOI: [10.1103/PhysRevLett.86.1733](https://doi.org/10.1103/PhysRevLett.86.1733), (cit. on p. 2, 30).
- [18] V. Kumar, Y. Kawazoe, “*Metal-Encapsulated Fullerenelike and Cubic Caged Clusters of Silicon*”, Phys. Rev. Lett. **87**, 045503 (2001), DOI: [10.1103/PhysRevLett.87.045503](https://doi.org/10.1103/PhysRevLett.87.045503), (cit. on p. 2, 30, 62).
- [19] V. Kumar, A. K. Singh, Y. Kawazoe, “*Smallest Magic Caged Clusters of Si, Ge, Sn, and Pb by Encapsulation of Transition Metal Atom*”, Nano Lett. **4**, 677 (2004), DOI: [10.1021/nl0498076](https://doi.org/10.1021/nl0498076), (cit. on p. 2).
- [20] M. B. Torres, E. M. Fernández, L. C. Balbás, “*Study of the Structural and Electronic Properties of  $[Ti@Si_{16}]_n$ ,  $[Sc@Si_{16}K]_n$ , and  $[V@Si_{16}F]_n$  ( $n = 9$ ) Aggregates from First Principles*”, J. Phys. Chem. C **115**, 335 (2011), DOI: [10.1021/jp1066742](https://doi.org/10.1021/jp1066742), (cit. on p. 2, 49, 59, 62).
- [21] T. Iwasa, A. Nakajima, “*Geometric, Electronic, and Optical Properties of a Superatomic Heterodimer and Trimer:  $Sc@Si_{16}-V@Si_{16}$  and  $Sc@Si_{16}-Ti@Si_{16}-V@Si_{16}$* ”, J. Phys. Chem. C **116**, 14071 (2012), DOI: [10.1021/jp302752g](https://doi.org/10.1021/jp302752g), (cit. on p. 2, 49, 53, 57, 59, 62).
- [22] S. M. Beck, “*Studies of Silicon Cluster-Metal Atom Compound Formation in a Supersonic Molecular Beam*”, J. Chem. Phys. **87**, 4233 (1987), DOI: [10.1063/1.452877](https://doi.org/10.1063/1.452877), (cit. on p. 2).
- [23] S. M. Beck, “*Mixed Metal-Silicon Clusters Formed by Chemical Reaction in a Supersonic Molecular Beam: Implications for Reactions at the Metal/Silicon Interface*”, J. Chem. Phys. **90**, 6306 (1989), DOI: [10.1063/1.456684](https://doi.org/10.1063/1.456684), (cit. on p. 2, 90, 92).
- [24] M. Ohara, K. Miyajima, A. Pramann, A. Nakajima, K. Kaya, “*Geometric and Electronic Structures of Terbium Silicon Mixed Clusters ( $TbSi_n$ ;  $6 \leq n \leq 16$ )*”, J. Phys. Chem. A **106**, 3702 (2002), DOI: [10.1021/jp012952c](https://doi.org/10.1021/jp012952c), (cit. on p. 2).
- [25] M. Ohara, K. Koyasu, A. Nakajima, K. Kaya, “*Geometric and Electronic Structures of M-doped Silicon Clusters ( $M = Ti, Hf, Mo$  and  $W$ )*”, Chem. Phys. Lett. **371**, 490 (2003), DOI: [10.1016/S0009-2614\(03\)00299-9](https://doi.org/10.1016/S0009-2614(03)00299-9), (cit. on p. 2, 89, 92).
- [26] A. Negishi, N. Kariya, K. Sugawara, I. Arai, H. Hiura, T. Kanayama, “*Size-Selective Formation of Tungsten Cluster-Containing Silicon Cages by the Reactions of  $W_n^+$  ( $n = 1-5$ ) with  $SiH_4$* ”, Chem. Phys. Lett. **388**, 463 (2004), DOI: [10.1016/j.cplett.2004.03.036](https://doi.org/10.1016/j.cplett.2004.03.036), (cit. on p. 2).



- [27] K. Koyasu, J. Atobe, M. Akutsu, M. Mitsui, A. Nakajima, “*Electronic and Geometric Stabilities of Clusters with Transition Metal Encapsulated by Silicon*”, J. Phys. Chem. A **111**, 42 (2007), DOI: [10.1021/jp066757f](https://doi.org/10.1021/jp066757f), (cit. on p. 2, 31, 93).
- [28] J. B. Jaeger, T. D. Jaeger, M. A. Duncan, “*Photodissociation of Metal-Silicon Clusters: Encapsulated versus Surface-Bound Metal*”, J. Phys. Chem. A **110**, 9310 (2006), DOI: [10.1021/jp0629947](https://doi.org/10.1021/jp0629947), (cit. on p. 2).
- [29] E. Janssens, P. Gruene, G. Meijer, L. Wöste, P. Lievens, A. Fielicke, “*Argon Physisorption as Structural Probe for Endohedrally Doped Silicon Clusters*”, Phys. Rev. Lett. **99**, 063401 (2007), DOI: [10.1103/PhysRevLett.99.063401](https://doi.org/10.1103/PhysRevLett.99.063401), (cit. on p. 2, 62, 65).
- [30] J. T. Lau, K. Hirsch, Ph. Klar, A. Langenberg, F. Lofink, R. Richter, J. Rittmann, M. Vogel, V. Zamudio-Bayer, T. Möller, “*X-Ray Spectroscopy Reveals High Symmetry and Electronic Structure of Transition-Metal-Doped Silicon Clusters*”, Phys. Rev. A **79**, 053201 (2009), DOI: [10.1103/PhysRevA.79.053201](https://doi.org/10.1103/PhysRevA.79.053201), (cit. on p. 2, 31, 39).
- [31] V. E. Matulis, O. A. Ivashkevich, V. S. Gurin, “*DFT Study of Electronic Structure and Geometry of Neutral and Anionic Silver Clusters*”, J. Mol. Struct. (Theochem) **664**, 291 (2003), DOI: [10.1016/j.theochem.2003.10.003](https://doi.org/10.1016/j.theochem.2003.10.003), (cit. on p. 2).
- [32] A. Fielicke, C. Ratsch, G. von Helden, G. Meijer, “*The Far-Infrared Spectra of Neutral and Cationic Niobium Clusters: Nb<sub>5</sub><sup>0/+</sup> to Nb<sub>9</sub><sup>0/+</sup>*”, J. Chem. Phys. **127**, 234306 (2007), DOI: [10.1063/1.2806176](https://doi.org/10.1063/1.2806176), (cit. on p. 2).
- [33] P. Gruene, A. Fielicke, G. Meijer, “*Experimental Vibrational Spectra of Gas-Phase Tantalum Cluster Cations*”, J. Chem. Phys. **127**, 234307 (2007), DOI: [10.1063/1.2806177](https://doi.org/10.1063/1.2806177), (cit. on p. 2).
- [34] R. Gehrke, P. Gruene, A. Fielicke, G. Meijer, K. Reuter, “*Nature of Ar Bonding to Small Co<sub>n</sub><sup>+</sup> Clusters and its Effect on the Structure Determination by Far-Infrared Absorption Spectroscopy*”, J. Chem. Phys. **130**, 034306 (2009), DOI: [10.1063/1.3058637](https://doi.org/10.1063/1.3058637), (cit. on p. 2).
- [35] U. Heiz, U. Landmann (Eds.), “*Nanocatalysis*”, Springer, Berlin, 2007, ISBN: [3-540-32646-4](https://doi.org/10.1007/9780470141748.ch1), (cit. on p. 2).
- [36] D. J. Wales, J. P. K. Doye, M. A. Miller, P. N. Mortenson, T. R. Walsh, “*Energy Landscapes: From Clusters to Biomolecules*”, Adv. Chem. Phys. **115**, 1 (2000), DOI: [10.1002/9780470141748.ch1](https://doi.org/10.1002/9780470141748.ch1), (cit. on p. 2, 32, 94).
- [37] D. J. Wales, M. A. Miller, T. R. Walsh, “*Archetypal Energy Landscapes*”, Nature **394**, 758 (1998), DOI: [10.1038/29487](https://doi.org/10.1038/29487), (cit. on p. 2).
- [38] S. Kirkpatrick, C. D. Gelatt, Jr., M. P. Vecchi, “*Optimization by Simulated Annealing*”, Science **220**, 671 (1983), DOI: [10.1126/science.220.4598.671](https://doi.org/10.1126/science.220.4598.671), (cit. on p. 3, 20).
- [39] D. M. Deaven, K. M. Ho, “*Molecular Geometry Optimization with a Genetic Algorithm*”, Phys. Rev. Lett. **75**, 288 (1995), DOI: [10.1103/PhysRevLett.75.288](https://doi.org/10.1103/PhysRevLett.75.288), (cit. on p. 3, 22).

## References

- [40] D. J. Wales, J. P. K. Doye, “*Global Optimization by Basin-Hopping and the Lowest Energy Structures of Lennard-Jones Clusters Containing up to 110 Atoms*”, J. Phys. Chem. A **101**, 5111 (1997), DOI: [10.1021/jp970984n](https://doi.org/10.1021/jp970984n), (cit. on p. [3](#), [21](#), [32](#)).
- [41] R. Gehrke, K. Reuter, “*Assessing the Efficiency of First-Principles Basin-Hopping Sampling*”, Phys. Rev. B **79**, 085412 (2009), DOI: [10.1103/PhysRevB.79.085412](https://doi.org/10.1103/PhysRevB.79.085412), (cit. on p. [3](#), [21](#), [22](#), [32](#)).
- [42] C. M. Weinert, M. Scheffler, “*Chalcogen and Vacancy Pairs in Silicon: Electronic Structure and Stabilities*”, Mat. Sci. Forum **10**, 25 (1986), DOI: [10.4028/www.scientific.net/MSF.10-12.25](https://doi.org/10.4028/www.scientific.net/MSF.10-12.25), (cit. on p. [3](#), [23](#), [85](#), [88](#)).
- [43] P. Hohenberg, W. Kohn, “*Inhomogeneous Electron Gas*”, Phys. Rev. **136**, B864 (1964), DOI: [10.1103/PhysRev.136.B864](https://doi.org/10.1103/PhysRev.136.B864), (cit. on p. [3](#), [9](#), [15](#)).
- [44] W. Kohn, L. J. Sham, “*Self-Consistent Equations Including Exchange and Correlation Effects*”, Phys. Rev. **140**, A1133 (1965), DOI: [10.1103/PhysRev.140.A1133](https://doi.org/10.1103/PhysRev.140.A1133), (cit. on p. [3](#), [9](#)).
- [45] E. Runge, E. K. U. Gross, “*Density-Functional Theory for Time-Dependent Systems*”, Phys. Rev. Lett. **52**, 997 (1984), DOI: [10.1103/PhysRevLett.52.997](https://doi.org/10.1103/PhysRevLett.52.997), (cit. on p. [3](#), [15](#), [46](#)).
- [46] R. E. Stratmann, G. E. Scuseria, M. J. Frisch, “*An Efficient Implementation of Time-Dependent Density-Functional Theory for the Calculation of Excitation Energies of Large Molecules*”, J. Chem. Phys. **109**, 8218 (1998), DOI: [10.1063/1.477483](https://doi.org/10.1063/1.477483), (cit. on p. [3](#), [16](#), [46](#)).
- [47] D. Porezag, T. Frauenheim, T. Köhler, G. Seifert, R. Kaschner, “*Construction of Tight-Binding-Like Potentials on the Basis of Density-Functional Theory: Application to Carbon*”, Phys. Rev. B **51**, 12947 (1995), DOI: [10.1103/PhysRevB.51.12947](https://doi.org/10.1103/PhysRevB.51.12947), (cit. on p. [3](#), [17](#), [95](#)).
- [48] G. Seifert, D. Porezag, T. Frauenheim, “*Calculations of Molecules, Clusters, and Solids with a Simplified LCAO-DFT-LDA Scheme*”, Int. J. Quant. Chem. **58**, 185 (1996), DOI: [10.1002/\(SICI\)1097-461X\(1996\)58:2<185::AID-QUA7>3.0.CO;2-U](https://doi.org/10.1002/(SICI)1097-461X(1996)58:2<185::AID-QUA7>3.0.CO;2-U), (cit. on p. [3](#), [16](#), [95](#)).
- [49] E. Schrödinger, “*An Undulatory Theory of the Mechanics of Atoms and Molecules*”, Phys. Rev. **28**, 1049 (1926), DOI: [10.1103/PhysRev.28.1049](https://doi.org/10.1103/PhysRev.28.1049), (cit. on p. [6](#)).
- [50] M. Born, R. Oppenheimer, “*Zur Quantentheorie der Molekeln*”, Annalen der Physik **389**, 457 (1927), DOI: [10.1002/andp.19273892002](https://doi.org/10.1002/andp.19273892002), (cit. on p. [6](#), [25](#)).
- [51] A. Szabo, N. S. Ostlund, “*Modern Quantum Chemistry*”, Mineola, New York, 1996, ISBN: [0-486-69186-1](https://www.isbn-international.org/product/0-486-69186-1), (cit. on p. [7](#)).
- [52] W. Pauli, “*Über den Einfluß der Geschwindigkeitsabhängigkeit der Elektronenmasse auf den Zeemaneffekt*”, Z. Physik **31**, 373 (1925), DOI: [10.1007/BF02980592](https://doi.org/10.1007/BF02980592), (cit. on p. [7](#)).
- [53] J. C. Slater, “*The Theory of Complex Spectra*”, Phys. Rev. **34**, 1293 (1929), DOI: [10.1103/PhysRev.34.1293](https://doi.org/10.1103/PhysRev.34.1293), (cit. on p. [7](#)).

- [54] D. R. Hartree, “*The Wave Mechanics of an Atom with a Non-Coulomb Central Field*”, Math. Proc. Cambridge Phil. Soc. **24**, 89 (1928), DOI: [10.1017/S0305004100011919](https://doi.org/10.1017/S0305004100011919), (cit. on p. 7).
- [55] V. Fock, “*Näherungsmethode zur Lösung des quantenmechanischen Mehrkörperproblems*”, Z. Physik **61**, 126 (1930), DOI: [10.1007/BF01340294](https://doi.org/10.1007/BF01340294), (cit. on p. 7).
- [56] C. C. J. Roothaan, “*New Developments in Molecular Orbital Theory*”, Rev. Mod. Phys. **23**, 69 (1951), DOI: [10.1103/RevModPhys.23.69](https://doi.org/10.1103/RevModPhys.23.69), (cit. on p. 9).
- [57] W. Koch, M. C. Holthausen, “*A Chemist’s Guide to Density Functional Theory*”, Wiley-VCH, Weinheim, 2001, ISBN: [3-527-30372-3](https://www.wiley.com/9783527303723), (cit. on p. 9, 12, 15).
- [58] R. G. Parr, W. Yang, “*Density-Functional Theory of Atoms and Molecules*”, Oxford University Press, Oxford, 1989, ISBN: [0-195-04279-4](https://www.oup.com/9780195042794), (cit. on p. 9).
- [59] G. E. Scuseria, V. N. Staroverov, “*Progress in the Development of Exchange-Correlation Functionals*”. In *Theory and Applications of Computational Chemistry: The First Forty Years*, ed. by C. E. Dykstra, G. Frenking, K. S. Kim, and G. E. Scuseria, pp. 669–724, Elsevier, Amsterdam, 2005, ISBN: [0-44451-719-7](https://www.elsevier.com/9780444517197), (cit. on p. 11).
- [60] F. Bloch, “*Bemerkung zur Elektronentheorie des Ferromagnetismus und der elektrischen Leitfähigkeit*”, Z. Physik **57**, 545 (1929), DOI: [10.1007/BF01340281](https://doi.org/10.1007/BF01340281), (cit. on p. 11).
- [61] P. A. M. Dirac, “*Note on Exchange Phenomena in the Thomas Atom*”, Math. Proc. Cambridge Phil. Soc. **26**, 376 (1930), DOI: [10.1017/S0305004100016108](https://doi.org/10.1017/S0305004100016108), (cit. on p. 11).
- [62] S. H. Vosko, L. Wilk, M. Nusair, “*Accurate Spin-Dependent Electron Liquid Correlation Energies For Local Spin Density Calculations: A Critical Analysis*”, Can. J. Phys. **58**, 1200 (1980), DOI: [10.1139/p80-159](https://doi.org/10.1139/p80-159), (cit. on p. 11).
- [63] J. P. Perdew, A. Zunger, “*Self-Interaction Correction to Density-Functional Approximations for Many-Electron Systems*”, Phys. Rev. B **23**, 5048 (1981), DOI: [10.1103/PhysRevB.23.5048](https://doi.org/10.1103/PhysRevB.23.5048), (cit. on p. 11).
- [64] L. A. Cole, J. P. Perdew, “*Calculated Electron Affinities of the Elements*”, Phys. Rev. A **25**, 1265 (1982), DOI: [10.1103/PhysRevA.25.1265](https://doi.org/10.1103/PhysRevA.25.1265), (cit. on p. 11).
- [65] J. P. Perdew, Y. Wang, “*Accurate and Simple Analytic Representation of the Electron-Gas Correlation Energy*”, Phys. Rev. B **45**, 13244 (1992), DOI: [10.1103/PhysRevB.45.13244](https://doi.org/10.1103/PhysRevB.45.13244), (cit. on p. 11).
- [66] J. P. Perdew, J. A. Chevary, S. H. Vosko, K. A. Jackson, M. R. Pederson, D. J. Singh, and C. Fiolhais, “*Atoms, Molecules, Solids, and Surfaces: Applications of the Generalized Gradient Approximation for Exchange and Correlation*”, Phys. Rev. B **46**, 6671 (1992), DOI: [10.1103/PhysRevB.46.6671](https://doi.org/10.1103/PhysRevB.46.6671), (cit. on p. 11).
- [67] G. J. Laming, V. Termath, N. C. Handy, “*A General Purpose Exchange-Correlation Energy Functional*”, J. Chem. Phys. **99**, 8765 (1992), DOI: [10.1063/1.465598](https://doi.org/10.1063/1.465598), (cit. on p. 11).

## References

- [68] M. Filatov, W. Thiel, “*A New Gradient-Corrected Exchange-Correlation Density Functional*”, *Mol. Phys.* **91**, 847 (1997), DOI: [10.1080/002689797170950](https://doi.org/10.1080/002689797170950), (cit. on p. 11).
- [69] J. P. Perdew, K. Burke, and M. Ernzerhof, “*Generalized Gradient Approximation Made Simple*”, *Phys. Rev. Lett.* **77**, 3865 (1996), DOI: [10.1103/PhysRevLett.77.3865](https://doi.org/10.1103/PhysRevLett.77.3865), (cit. on p. 11, 31).
- [70] A. D. Becke, “*A New Mixing of Hartree-Fock and Local Density-Functional Theories*”, *J. Chem. Phys.* **98**, 1372 (1993), DOI: [10.1063/1.464304](https://doi.org/10.1063/1.464304), (cit. on p. 12).
- [71] P. J. Stephens, F. J. Devlin, C. F. Chabalowski, M. J. Frisch, “*Ab Initio Calculation of Vibrational Absorption and Circular Dichroism Spectra Using Density Functional Force Fields*”, *J. Phys. Chem.* **98**, 11623 (1994), DOI: [10.1021/j100096a001](https://doi.org/10.1021/j100096a001), (cit. on p. 12, 31).
- [72] C. Adamo, V. Barone, “*Toward Reliable Density Functional Methods Without Adjustable Parameters: The PBE0 Model*”, *J. Chem. Phys.* **110**, 6158 (1999), DOI: [10.1063/1.478522](https://doi.org/10.1063/1.478522), (cit. on p. 12, 31, 42, 46, 66).
- [73] G. Frenking, I. Antes, M. Böhme, S. Dapprich, A. W. Ehlers, V. Jonas, A. Neuhaus, M. Otto, R. Stegmann, A. Veldkamp, S. F. Vyboishchikov, “*Pseudopotential Calculations of Transition Metal Compounds: Scope and Limitations*”, *Rev. Comp. Chem.* **8**, 63 (1996), DOI: [10.1002/9780470125854.ch2](https://doi.org/10.1002/9780470125854.ch2), (cit. on p. 12).
- [74] T. R. Cundari, M. T. Benson, M. L. Lutz, S. O. Sommerer, “*Effective Core Potential Approaches to the Chemistry of the Heavier Elements*”, *Rev. Comp. Chem.* **8**, 145 (1996), DOI: [10.1002/9780470125854.ch3](https://doi.org/10.1002/9780470125854.ch3), (cit. on p. 12).
- [75] C. S. Garoufalis, A. D. Zdetsis, S. Grimme, “*High Level Ab Initio Calculations of the Optical Gap of Small Silicon Quantum Dots*”, *Phys. Rev. Lett.* **87**, 276402 (2001), DOI: [10.1103/PhysRevLett.87.276402](https://doi.org/10.1103/PhysRevLett.87.276402), (cit. on p. 12).
- [76] C. J. Cramer, D. G. Truhlar, “*Density Functional Theory for Transition Metals and Transition Metal Chemistry*”, *Phys. Chem. Chem. Phys.* **11**, 10757 (2009), DOI: [10.1039/b907148b](https://doi.org/10.1039/b907148b), (cit. on p. 12, 66).
- [77] J. C. Slater, “*Atomic Shielding Constants*”, *Phys. Rev.* **36**, 57 (1930), DOI: [10.1103/PhysRev.36.57](https://doi.org/10.1103/PhysRev.36.57), (cit. on p. 12, 17).
- [78] S. F. Boys, “*Electronic Wave Functions. I. A General Method of Calculation for the Stationary States of Any Molecular System*”, *Proc. R. Soc. London Ser. A* **200**, 542 (1950), DOI: [10.1098/rspa.1950.0036](https://doi.org/10.1098/rspa.1950.0036), (cit. on p. 12).
- [79] V. Blum, R. Gehrke, F. Hanke, P. Havu, V. Havu, X. Ren, K. Reuter, M. Scheffler, “*Ab initio Simulations with Numeric Atom-Centered Orbitals*”, *Comp. Phys. Comm.* **180**, 2175 (2009), DOI: [10.1016/j.cpc.2009.06.022](https://doi.org/10.1016/j.cpc.2009.06.022), (cit. on p. 12, 13, 14, 31).
- [80] X. Ren, P. Rinke, V. Blum, J. Wieferink, A. Tkatchenko, A. Sanfilippo, K. Reuter, M. Scheffler, “*Resolution-of-Identity Approach to Hartree-Fock, Hybrid Density*

- Functionals, RPA, MP2 and GW with Numeric Atom-Centered Orbital Basis Functions*”, New. J. Phys. **14**, 053020 (2012), DOI: [10.1088/1367-2630/14/5/053020](https://doi.org/10.1088/1367-2630/14/5/053020), (cit. on p. [12](#), [31](#)).
- [81] S. F. Boys, F. Bernardi, “*The Calculation of Small Molecular Interactions by the Differences of Separate Total Energies. Some procedures With Reduced Errors*”, Mol. Phys. **19**, 533 (1970), DOI: [10.1080/00268977000101561](https://doi.org/10.1080/00268977000101561), (cit. on p. [13](#)).
- [82] B. Delley, “*An All-Electron Numerical Method For Solving The Local Density Functional For Polyatomic Molecules*”, J. Chem. Phys. **92**, 508 (1990), DOI: [10.1063/1.458452](https://doi.org/10.1063/1.458452), (cit. on p. [13](#)).
- [83] G. B. Arfken, H. J. Weber, “*Mathematical Methods for Physicists*”, Elsevier, Amsterdam, 2005, ISBN: [0-120-59876-0](https://www.isbn-international.org/product/0-120-59876-0), (cit. on p. [13](#)).
- [84] E. van Lenthe, E. J. Baerends, J. G. Snijders, “*Relativistic Regular Two-Component Hamiltonians*”, J. Chem. Phys. **99**, 4597 (1993), DOI: [10.1063/1.466059](https://doi.org/10.1063/1.466059), (cit. on p. [14](#)).
- [85] E. van Lenthe, E. J. Baerends, J. G. Snijders, “*Relativistic Total Energy Using Regular Approximations*”, J. Chem. Phys. **101**, 9783 (1994), DOI: [10.1063/1.467943](https://doi.org/10.1063/1.467943), (cit. on p. [14](#)).
- [86] O. Gunnarsson, B. I. Lundqvist, “*Exchange and Correlation in Atoms, Molecules, and Solids by the Spin-Density-Functional Formalism*”, Phys. Rev. B **13**, 4274 (1976), DOI: [10.1103/PhysRevB.13.4274](https://doi.org/10.1103/PhysRevB.13.4274), (cit. on p. [15](#)).
- [87] S. Grimme, “*Density Functional Calculations with Configuration Interaction for the Excited States of Molecules*”, Chem. Phys. Lett. **259**, 128 (1996), DOI: [10.1016/0009-2614\(96\)00722-1](https://doi.org/10.1016/0009-2614(96)00722-1), (cit. on p. [15](#)).
- [88] M. J. Frisch, I. N. Ragazos, M. A. Robb, and H. B. Schlegel, “*An Evaluation of 3 Direct MC-SCF Procedures*”, Chem. Phys. Lett. **189**, 524 (1992), DOI: [10.1016/0009-2614\(92\)85244-5](https://doi.org/10.1016/0009-2614(92)85244-5), (cit. on p. [15](#)).
- [89] M. A. L. Marques, C. A. Ullrich, F. Nogueira, A. Rubio, K. Burke, and E. K. U. Gross (Eds.), “*Time-Dependent Density Functional Theory*”, Springer, Berlin, 2006, ISBN: [3-540-35422-0](https://www.isbn-international.org/product/3-540-35422-0), (cit. on p. [15](#), [16](#)).
- [90] R. Kubo, “*Statistical Mechanical Theory of Irreversible Processes I. General Theory and Simple Applications to Magnetic and Conduction Problems*”, J. Phys. Soc. Jpn. **12**, 570 (1957), DOI: [10.1143/JPSJ.12.570](https://doi.org/10.1143/JPSJ.12.570), (cit. on p. [16](#)).
- [91] R. Zwanzig, “*Nonequilibrium Statistical Mechanics*”, Oxford University Press, Oxford, 2001, ISBN: [0-195-14018-4](https://www.isbn-international.org/product/0-195-14018-4), (cit. on p. [16](#)).
- [92] [Gaussian 03](#), Rev. D.01, M. J. Frisch *et al.*, Gaussian, Inc., Wallingford CT, 2004, (cit. on p. [16](#), [46](#)).
- [93] J. B. Foresman, Æ. Frisch, “*Exploring Chemistry With Electronic Structure Methods*”, Gaussian, Inc., Pittsburgh, 1996, ISBN: [0-963-67693-8](https://www.isbn-international.org/product/0-963-67693-8), (cit. on p. [16](#)).

## References

- [94] C. M. Goringe, D. R. Bowler, E. Hernández, “*Tight-Binding Modelling of Materials*”, Rep. Prog. Phys. **60**, 1447 (1997), DOI: [10.1088/0034-4885/60/12/001](https://doi.org/10.1088/0034-4885/60/12/001), (cit. on p. 16).
- [95] J. C. Slater, G. F. Koster, “*Simplified LCAO Method for the Periodic Potential Problem*”, Phys. Rev. **94**, 1498 (1954), DOI: [10.1103/PhysRev.94.1498](https://doi.org/10.1103/PhysRev.94.1498), (cit. on p. 17).
- [96] B. Aradi, B. Hourahine, T. Frauenheim, “*DFTB+, a Sparse Matrix-Based Implementation of the DFTB Method*”, J. Phys. Chem. A **111**, 5678 (2007), DOI: [10.1021/jp070186p](https://doi.org/10.1021/jp070186p), (cit. on p. 17).
- [97] F. Jensen, “*Introduction to Computational Chemistry*”, John Wiley & Sons, Chichester, 2007, ISBN: 0-470-01186-6, (cit. on p. 18, 19, 21, 22).
- [98] J. A. Snyman, “*Practical Mathematical Optimization: an Introduction to Basic Optimization Theory and Classical and New Gradient-Based Algorithms*”, Springer, New York, 2005, ISBN: 0-387-24348-8, (cit. on p. 18).
- [99] M. J. D. Powell, “*Nonconvex Minimization Calculations and the Conjugate Gradient Method*”, Lecture Notes in Mathematics **1066**, 122 (1984), DOI: [10.1007/BFb0099521](https://doi.org/10.1007/BFb0099521), (cit. on p. 18).
- [100] R. Fletcher, C. M. Reeves, “*Function Minimization by Conjugate Gradients*”, Comp. J. **7**, 149 (1964), DOI: [10.1093/comjnl/7.2.149](https://doi.org/10.1093/comjnl/7.2.149), (cit. on p. 19).
- [101] M. R. Hestenes, E. L. Stiefel, “*Methods of Conjugate Gradients for Solving Linear Systems*”, J. Res. Nat. Bur. Stand. **49**, 409 (1952), ISSN: 0091-0635, (cit. on p. 19).
- [102] T. J. Ypma, “*Historical Development of the Newton-Raphson Method*”, SIAM Review **37**, 531 (1995), DOI: [10.1137/1037125](https://doi.org/10.1137/1037125), (cit. on p. 19).
- [103] J. Nocedal, S. J. Wright, “*Numerical Optimization*”, Springer, New York, 2006, ISBN: 0-387-30303-0, (cit. on p. 19, 32).
- [104] W. K. Press, S. A. Teukolsky, W. T. Vetterlin, B. T. Flannery, “*Numerical Recipes: the Art of Scientific Computing*”, Cambridge University Press, Cambridge, 2007, ISBN: 0-521-88068-8, (cit. on p. 19, 32).
- [105] L. T. Biegler, I. E. Grossmann, “*Retrospective on Optimization*”, Comput. Chem. Eng. **28**, 1169 (2004), DOI: [10.1016/j.compchemeng.2003.11.003](https://doi.org/10.1016/j.compchemeng.2003.11.003), (cit. on p. 20).
- [106] I. E. Grossmann, L. T. Biegler, “*Future Perspective on Optimization*”, Comput. Chem. Eng. **28**, 1193 (2004), DOI: [10.1016/j.compchemeng.2003.11.006](https://doi.org/10.1016/j.compchemeng.2003.11.006), (cit. on p. 20).
- [107] A. Neumaier, “*Complete Search in Continuous Global Optimization and Constraint Satisfaction*”, Acta Numerica **13**, 271 (2004), DOI: [10.1017/S0962492904000194](https://doi.org/10.1017/S0962492904000194), (cit. on p. 20).
- [108] B. Hartke, “*Global Optimization*”, WIREs Comput. Mol. Sci. **1**, 879 (2011), DOI: [10.1002/wcms.70](https://doi.org/10.1002/wcms.70), (cit. on p. 20).

- [109] C. A. Floudas, C. E. Gounaris, “A Review of Recent Advances in Global Optimization”, J. Glob. Optim. **45**, 3 (2009), DOI: [10.1007/s10898-008-9332-8](https://doi.org/10.1007/s10898-008-9332-8), (cit. on p. 20).
- [110] S. Yoo, X. C. Zeng, “Global Geometry Optimization of Silicon Clusters Described by Three Empirical Potentials”, J. Chem. Phys. **119**, 1442 (2003), DOI: [10.1063/1.1581849](https://doi.org/10.1063/1.1581849), (cit. on p. 20).
- [111] B. J. Alder, T. E. Wainwright, “Studies in Molecular Dynamics. I. General Method”, J. Chem. Phys. **31**, 459 (1959), DOI: [10.1063/1.1730376](https://doi.org/10.1063/1.1730376), (cit. on p. 20).
- [112] N. Metropolis, A. W. Rosenbluth, M. N. Rosenbluth, A. H. Teller, E. Teller, “Equation of State Calculations by Fast Computing Machines”, J. Chem. Phys. **21**, 1087 (1953), DOI: [10.1063/1.1699114](https://doi.org/10.1063/1.1699114), (cit. on p. 20, 22, 33).
- [113] D. J. Wales, H. A. Scheraga, “Global Optimization of Clusters, Crystals, and Biomolecules”, Science **285**, 1368 (1999), DOI: [10.1126/science.285.5432.1368](https://doi.org/10.1126/science.285.5432.1368), (cit. on p. 21).
- [114] L. Zhan, B. Piwowar, W.-K. Liu, P. J. Hsu, S. K. Lai, J. Z. Y. Chen “Multicanonical Basin Hopping: A New Global Optimization Method for Complex Systems”, J. Chem. Phys. **120**, 5536 (2004), DOI: [10.1063/1.1649728](https://doi.org/10.1063/1.1649728), (cit. on p. 21).
- [115] D. M. Deaven, N. Tit, J. R. Morris, K. M. Ho, “Structural Optimization of Lennard-Jones Clusters by a Genetic Algorithm”, Chem. Phys. Lett. **256**, 195 (1996), DOI: [10.1016/0009-2614\(96\)00406-X](https://doi.org/10.1016/0009-2614(96)00406-X), (cit. on p. 22).
- [116] R. L. Johnston, “Evolving Better Nanoparticles: Genetic Algorithms for Optimising Cluster Geometries”, Dalton Trans. **22**, 4193 (2003), DOI: [10.1039/B305686D](https://doi.org/10.1039/B305686D), (cit. on p. 22).
- [117] J. Kostrowicki, H. A. Scheraga, “Application of the Diffusion Equation Method for Global Optimization to Oligopeptides”, J. Phys. Chem. **96**, 7442 (1992), DOI: [10.1021/j100197a057](https://doi.org/10.1021/j100197a057), (cit. on p. 22).
- [118] J. M. Blaney, J. S. Dixon, “Distance Geometry in Molecular Modeling”, Rev. Comp. Chem. **5**, 299 (1994), DOI: [10.1002/9780470125823.ch6](https://doi.org/10.1002/9780470125823.ch6), (cit. on p. 22).
- [119] S. Goedecker, “Minima Hopping: An Efficient Search Method for the Global Minimum of the Potential Energy Surface of Complex Molecular Systems”, J. Chem. Phys. **120**, 9911 (2004), DOI: [10.1063/1.1724816](https://doi.org/10.1063/1.1724816), (cit. on p. 22).
- [120] S. Goedecker, W. Hellmann, T. Lenosky, “Global Minimum Determination of the Born-Oppenheimer Surface within Density Functional Theory”, Phys. Rev. Lett. **95**, 055501 (2005), DOI: [10.1103/PhysRevLett.95.055501](https://doi.org/10.1103/PhysRevLett.95.055501), (cit. on p. 22).
- [121] U. H. E. Hansmann, L. T. Wille, “Global Optimization by Energy Landscape Paving”, Phys. Rev. Lett. **88**, 068105 (2002), DOI: [10.1103/PhysRevLett.88.068105](https://doi.org/10.1103/PhysRevLett.88.068105), (cit. on p. 22).
- [122] R. Gehrke, “First-Principles Basin-Hopping for the Structure Determination of Atomic Clusters”, Ph.D. Thesis, Freie Universität Berlin, Germany, 2009, available from [www.diss.fu-berlin.de](http://www.diss.fu-berlin.de), (cit. on p. 22).

## References

- [123] J. Rogal, K. Reuter, “*Ab initio Atomistic Thermodynamics for Surfaces: A Primer*”. In *Experiment, Modeling and Simulation of Gas-Surface Interactions for Reactive Flows in Supersonic Flights* (pp. 2-1 – 2-18). Educational Notes RTO-EN-AVT-142, Paper 2. Neuilly-sur-Seine, France: RTO. Available from: <http://www.cso.nato.int/>, (cit. on p. 23, 88, 94).
- [124] E. Kaxiras, Y. Bar-Yam, J. D. Joannopoulos, K. C. Pandey, “*Ab initio Theory of Polar Semiconductor Surfaces. I. Methodology and the (2×2) Reconstructions of GaAs(111)*”, Phys. Rev. B **35**, 9625 (1987), DOI: [10.1103/PhysRevB.35.9625](https://doi.org/10.1103/PhysRevB.35.9625), (cit. on p. 23, 88).
- [125] M. Scheffler, J. Dabrowski, “*Parameter-free Calculations of Total Energies, Interatomic Forces and Vibrational Entropies of Defects in Semiconductors*”, Phil. Mag. A **58**, 107 (1988), DOI: [10.1080/01418618808205178](https://doi.org/10.1080/01418618808205178), (cit. on p. 23, 88).
- [126] G.-X. Qian, R. M. Martin, D. J. Chadi, “*First-principles Study of the Atomic Reconstructions and Energies of Ga- and As-stabilized GaAs(100) Surfaces*”, Phys. Rev. B **38**, 7649 (1988), DOI: [10.1103/PhysRevB.38.7649](https://doi.org/10.1103/PhysRevB.38.7649), (cit. on p. 23).
- [127] H. B. Callen, “*Thermodynamics and an Introduction to Thermostatistics*”, John Wiley & Sons, New York, 1985, ISBN: [0-471-86256-8](https://www.wiley.com/9780471862568), (cit. on p. 23).
- [128] D. A. McQuarrie, J. D. Simon, “*Physical Chemistry: a Molecular Approach*”, University Science Books, Sausalito, Calif., 1997, ISBN: [0-935-70299-7](https://www.uscibooks.com/9780935702997), (cit. on p. 23).
- [129] D. A. McQuarrie, “*Statistical Mechanics*”, Harper & Row, New York, 1976, ISBN: [0-060-44366-9](https://www.harpercollins.com/9780060443669), (cit. on p. 23).
- [130] L. D. Landau, E. M. Lifshitz, “*Statistical Physics. Part 1*”. In *Course of Theoretical Physics, Volume 5*, Pergamon Press, Oxford, 1980, ISBN: [0-080-23039-3](https://www.pergamon.com/9780080230393), (cit. on p. 23).
- [131] L. D. Landau, E. M. Lifshitz, “*Statistical Physics. Part 2. Theory of the Condensed State*”. In *Course of Theoretical Physics, Volume 9*, Pergamon Press, Oxford, 1981, ISBN: [0-080-23073-3](https://www.pergamon.com/9780080230733), (cit. on p. 23).
- [132] A. Isihara, “*Statistical Physics*”, Academic Press, New York, 1971, ISBN: [0-123-74650-7](https://www.academicpress.com/9780123746507), (cit. on p. 24).
- [133] I. N. Godnev, “*Calculation of Thermodynamic Functions from Molecular Data*”, U.S. Atomic Energy Commission, Technical Information Service, Oak Ridge, 1959, OCLC Number: [8404787](https://www.worldcat.org/oclc/8404787), (cit. on p. 25).
- [134] T. L. Hill, “*An Introduction to Statistical Thermodynamics*”, Dover Publications, New York, 1986, ISBN: [0-486-65242-4](https://www.dover.com/9780486652424), (cit. on p. 25).
- [135] V. Kumar, Y. Kawazoe, “*Magic Behavior of Si<sub>15</sub>M and Si<sub>16</sub>M (M = Cr, Mo, and W) Clusters*”, Phys. Rev. B **65**, 073404 (2002), DOI: [10.1103/PhysRevB.65.073404](https://doi.org/10.1103/PhysRevB.65.073404), (cit. on p. 30).
- [136] M. F. Jarrold, E. C. Honea, “*Dissociation of Large Silicon Clusters: The Approach to Bulk Behavior*”, J. Phys. Chem. **95**, 9181 (1991), DOI: [10.1021/j100176a028](https://doi.org/10.1021/j100176a028), (cit. on p. 30).



- [137] K.-M. Ho, A. A. Shvartsburg, B. Pan, Z.-Y. Lu, C.-Z. Wang, J. G. Wacker, J. L. Fye, M. F. Jarrold, “*Structures of Medium-Sized Silicon Clusters*”, *Nature* **392**, 582 (1998), DOI: [10.1038/33369](https://doi.org/10.1038/33369), (cit. on p. 30).
- [138] K. A. Jackson, M. Horoi, I. Chaudhuri, T. Frauenheim, A. A. Shvartsburg, “*Unraveling the Shape Transformation in Silicon Clusters*”, *Phys. Rev. Lett.* **93**, 013401 (2004), DOI: [10.1103/PhysRevLett.93.013401](https://doi.org/10.1103/PhysRevLett.93.013401), (cit. on p. 30).
- [139] J. Bai, L.-F. Cui, J. Wang, S. Yoo, X. Li, J. Jellinek, C. Koehler, T. Frauenheim, L.-S. Wang, and X. Zeng, “*Structural Evolution of Anionic Silicon Clusters  $Si_n$  ( $20 \leq n \leq 45$ )*”, *Phys. Rev. Lett.* **93**, 013401 (2004), DOI: [10.1021/jp055874s](https://doi.org/10.1021/jp055874s), (cit. on p. 30).
- [140] V. Kumar, “*Alchemy at the Nanoscale: Magic Heteroatom Clusters and Assemblies*”, *Comput. Mater. Sci.* **36**, 1 (2006), DOI: [10.1016/j.commatsci.2005.06.004](https://doi.org/10.1016/j.commatsci.2005.06.004), (cit. on p. 30, 34, 93).
- [141] J. Ulises Reveles, S. N. Khanna, “*Nearly-Free-Electron Gas in a Silicon Cage*”, *Phys. Rev. B* **72**, 165413 (2005), DOI: [10.1103/PhysRevB.72.165413](https://doi.org/10.1103/PhysRevB.72.165413), (cit. on p. 30, 31, 34, 93).
- [142] J. Ulises Reveles, S. N. Khanna, “*Electronic Counting Rules for the Stability of Metal-Silicon Clusters*”, *Phys. Rev. B* **74**, 035435 (2006), DOI: [10.1103/PhysRevB.74.035435](https://doi.org/10.1103/PhysRevB.74.035435), (cit. on p. 30, 31, 34, 93).
- [143] M. B. Torres, E. M. Fernández, L. C. Balbás, “*Theoretical Study of Isoelectronic  $Si_nM$  clusters ( $M = Sc^-, Ti, V^+; n = 14-18$ )*”, *Phys. Rev. B* **75**, 205425 (2007), DOI: [10.1103/PhysRevB.75.205425](https://doi.org/10.1103/PhysRevB.75.205425), (cit. on p. 30, 31, 34, 63, 86, 93).
- [144] T. Rachi, K. Tanigaki, R. Kumashiro, J. Winter, H. Kuzmany, “*Preparation and Electronic States of  $Na_{16}Ba_8Si_{136}$  Clathrate*”, *Chem. Phys. Lett.* **409**, 48 (2005), DOI: [10.1016/j.cplett.2005.04.076](https://doi.org/10.1016/j.cplett.2005.04.076), (cit. on p. 30).
- [145] P. Claes, E. Janssens, V. T. Ngan, P. Gruene, J. T. Lyon, D. J. Harding, A. Fielicke, M. T. Nguyen, P. Lievens, “*Structural Identification of Caged Vanadium Doped Silicon Clusters*”, *Phys. Rev. Lett.* **107**, 173401 (2011), DOI: [10.1103/PhysRevLett.107.173401](https://doi.org/10.1103/PhysRevLett.107.173401), (cit. on p. 30).
- [146] D. Palagin, M. Gramzow, K. Reuter, “*On the Stability of “Non-Magic” Endohedrally Doped Si Clusters: A First-Principles Sampling Study of  $MSi_{16}^+$  ( $M = Ti, V, Cr$ )*”, *J. Chem. Phys.* **134**, 244705 (2011), DOI: [10.1063/1.3604565](https://doi.org/10.1063/1.3604565), (cit. on p. 30, 33, 41, 49, 63, 64).
- [147] D. Palagin, K. Reuter, “*Evaluation of Endohedral Doping of Hydrogenated Si Fullerenes as a Route to Magnetic Si Building Blocks*”, *Phys. Rev. B* **86**, 045416 (2012), DOI: [10.1103/PhysRevB.86.045416](https://doi.org/10.1103/PhysRevB.86.045416), (cit. on p. 30, 42, 49, 50, 57, 58, 62, 64, 65, 68, 73).
- [148] D. Palagin, K. Reuter, “ *$MSi_{20}H_{20}$  Aggregates: From Simple Building Blocks to Highly Magnetic Functionalized Materials*”, *ACS Nano* **7**, 1763 (2013), DOI: [10.1021/nm3058888](https://doi.org/10.1021/nm3058888), (cit. on p. 30, 62, 64).

## References

- [149] K. A. Jackson, E. Kaxiras, M. R. Pederson, “*Bonding of Endohedral Atoms in Small Carbon Fullerenes*”, *J. Phys. Chem.* **98**, 7805 (1994), DOI: [10.1021/j100083a010](https://doi.org/10.1021/j100083a010), (cit. on p. [31](#), [34](#), [63](#)).
- [150] F. C. Frank, J. S. Kasper, “*Complex Alloy Structures Regarded as Sphere Packings. I. Definitions and Basic Principles*”, *Acta Crystallogr.* **11**, 184 (1958), DOI: [10.1107/S0365110X58000487](https://doi.org/10.1107/S0365110X58000487), (cit. on p. [31](#)).
- [151] F. C. Frank, J. S. Kasper, “*Complex Alloy Structures Regarded as Sphere Packings. I. Analysis and Classification of Representative Structures*”, *Acta Crystallogr.* **12**, 483 (1959), DOI: [10.1107/S0365110X59001499](https://doi.org/10.1107/S0365110X59001499), (cit. on p. [31](#)).
- [152] K. Koyasu, M. Akutsu, M. Mitsui, A. Nakajima, “*Selective Formation of  $MSi_{16}$  ( $M = Sc, Ti, \text{ and } V$ )*”, *J. Am. Chem. Soc.* **127**, 4998 (2005), DOI: [10.1021/ja045380t](https://doi.org/10.1021/ja045380t), (cit. on p. [31](#), [86](#), [89](#), [92](#), [93](#)).
- [153] J. J. Thomson, “*On the Structure of the Atom: an Investigation of the Stability and Periods of Oscillation of a Number of Corpuscles Arranged at Equal Intervals Around the Circumference of a Circle; with Application of the Results to the Theory of Atomic Structure*”, *Philos. Mag.* **6**, 237 (1904), DOI: [10.1080/14786440409463107](https://doi.org/10.1080/14786440409463107), (cit. on p. [33](#)).
- [154] A. Willand, M. Gramzow, S. Alireza Ghasemi, L. Genovese, T. Deutsch, K. Reuter, S. Goedecker, “*Structural Metastability of Endohedral Silicon Fullerenes*”, *Phys. Rev. B* **81**, 201405 (2010), DOI: [10.1103/PhysRevB.81.201405](https://doi.org/10.1103/PhysRevB.81.201405), (cit. on p. [33](#), [44](#), [49](#)).
- [155] V. Kumar, Y. Kawazoe, “*Hydrogenated Silicon Fullerenes: Effects of H on the Stability of Metal-Encapsulated Silicon Clusters*”, *Phys. Rev. Lett.* **90**, 055502 (2003), DOI: [10.1103/PhysRevLett.90.055502](https://doi.org/10.1103/PhysRevLett.90.055502), (cit. on p. [41](#), [49](#), [62](#), [63](#), [76](#), [93](#)).
- [156] V. Kumar, Y. Kawazoe, “*Hydrogenated Caged Clusters of Si, Ge, and Sn and Their Endohedral Doping with Atoms: ab initio Calculations*”, *Phys. Rev. B* **75**, 155425 (2007), DOI: [10.1103/PhysRevB.75.155425](https://doi.org/10.1103/PhysRevB.75.155425), (cit. on p. [41](#), [62](#), [93](#)).
- [157] M. S. Bahramy, V. Kumar, Y. Kawazoe, “*First-Principles Calculations of Hyperfine Structure in M-doped  $Si_{16}H_{16}$  Fullerene Cages ( $M = Cr, Mn, \text{ and } Fe$ )*”, *Phys. Rev. B* **79**, 235443 (2009), DOI: [10.1103/PhysRevB.79.235443](https://doi.org/10.1103/PhysRevB.79.235443), (cit. on p. [41](#), [62](#)).
- [158] P. J. Hay, W. R. Wadt, “*Ab initio Effective Core Potentials for Molecular Calculations. Potentials for K to Au Including the Outermost Core Orbitals*”, *J. Chem. Phys.* **82**, 299 (1985), DOI: [10.1063/1.448975](https://doi.org/10.1063/1.448975), (cit. on p. [46](#)).
- [159] A.-H. Lu, E. L. Salabas, F. Schüth, “*Magnetic Nanoparticles: Synthesis, Protection, Functionalization, and Application*”, *Angew. Chem. Int. Ed.* **46**, 1222 (2007), DOI: [10.1002/anie.200602866](https://doi.org/10.1002/anie.200602866), (cit. on p. [49](#)).
- [160] V. T. Ngan, E. Janssens, P. Claes, J. T. Lyon, A. Fielicke, M. T. Nguyen, P. Lievens, “*High Magnetic Moments in Manganese-Doped Silicon Clusters*”, *Chem. Eur. J.* **18**, 15788 (2012), DOI: [10.1002/chem.201201839](https://doi.org/10.1002/chem.201201839), (cit. on p. [49](#)).

- [161] R. Robles, S. N. Khanna, “*Magnetism in Assembled and Supported Silicon Endohedral Cages: First-principles Electronic Structure Calculations*”, Phys. Rev. B **80**, 115414 (2009), DOI: [10.1103/PhysRevB.80.115414](https://doi.org/10.1103/PhysRevB.80.115414), (cit. on p. 49).
- [162] G. K. Ramachandran, J. Dong, J. Diefenbacher, J. Gryko, R. F. Marzke, O. F. Sankey, P. F. McMillan, “*Synthesis and X-Ray Characterization of Silicon Clathrates*”, J. Solid State Chem. **145**, 716 (1999), DOI: [10.1006/jssc.1999.8295](https://doi.org/10.1006/jssc.1999.8295), (cit. on p. 57).
- [163] A. San-Miguel, P. Kéghélian, X. Blase, P. Mélinon, A. Perez, J. P. Itié, A. Polian, E. Reny, C. Cros, M. Pouchard, “*High Pressure Behavior of Silicon Clathrates: A New Class of Low Compressibility Materials*”, Phys. Rev. Lett. **83**, 5290 (1999), DOI: [10.1103/PhysRevLett.83.5290](https://doi.org/10.1103/PhysRevLett.83.5290), (cit. on p. 57).
- [164] K. A. Kovnir, A. V. Shevelkov, “*Semiconducting Clathrates: Synthesis, Structure and Properties*”, Russ. Chem. Rev. **73**, 923 (2004), DOI: [10.1070/RC2004v073n09ABEH000916](https://doi.org/10.1070/RC2004v073n09ABEH000916), (cit. on p. 57).
- [165] A. J. Karttunen, T. F. Fässler, M. Linnolahti, T. A. Pakkanen, “*Structural Principles of Semiconducting Group 14 Clathrate Frameworks*”, Inorg. Chem. **50**, 1733 (2011), DOI: [10.1021/ic102178d](https://doi.org/10.1021/ic102178d), (cit. on p. 57).
- [166] R. Westerström, J. Dreiser, C. Piamonteze, M. Muntwiler, S. Weyeneth, H. Brune, S. Rusponi, F. Nolting, A. Popov, S. Yang, L. Dunsch, T. Greber, “*An Endohedral Single-Molecule Magnet with Long Relaxation Times: DySc<sub>2</sub>N@C<sub>80</sub>*”, J. Am. Chem. Soc. **134**, 9840 (2012), DOI: [10.1021/ja301044p](https://doi.org/10.1021/ja301044p), (cit. on p. 62).
- [167] M. A. Reed, C. Zhou, C. J. Muller, T. P. Burgin, J. M. Tour, “*Conductance of a Molecular Junction*”, Science **278**, 252 (1997), DOI: [10.1126/science.278.5336.252](https://doi.org/10.1126/science.278.5336.252), (cit. on p. 62).
- [168] E. Nakamura, H. Isobe, “*Functionalized Fullerenes in Water. The First 10 Years of Their Chemistry, Biology, and Nanoscience*”, Acc. Chem. Res. **36**, 807 (2003), DOI: [10.1021/ar030027y](https://doi.org/10.1021/ar030027y), (cit. on p. 62).
- [169] H. Imahori, S. Fukuzumi, “*Porphyrin- and Fullerene-Based Molecular Photovoltaic Devices*”, Adv. Funct. Mater. **14**, 525 (2004), DOI: [10.1002/adfm.200305172](https://doi.org/10.1002/adfm.200305172), (cit. on p. 62).
- [170] C. Deibel, V. Dyakonov, “*Polymer-Fullerene Bulk Heterojunction Solar Cells*”, Rep. Prog. Phys. **73**, 096401 (2010), DOI: [10.1088/0034-4885/73/9/096401](https://doi.org/10.1088/0034-4885/73/9/096401), (cit. on p. 62).
- [171] S. M. Sze, K. K. Ng, “*Physics of Semiconductor Devices*”, Wiley-Interscience, Hoboken, New Jersey, 2007, ISBN: [0-471-14323-5](https://doi.org/10.1002/qua.22750), (cit. on p. 62).
- [172] M. B. Torres, E. M. Fernández, L. C. Balbás, “*Theoretical Study of the Structural and Electronic Properties of Aggregates, Wires, and Bulk Phases Formed from M@Si<sub>16</sub> superatoms (M = Sc<sup>-</sup>, Ti, V<sup>+</sup>)*”, Int. J. Quantum Chem. **111**, 444 (2011), DOI: [10.1002/qua.22750](https://doi.org/10.1002/qua.22750), (cit. on p. 62).

## References

- [173] H. Cantera-López, L. C. Balbás, G. Borstel, “*First-principles Calculations of Structural and Electronic Properties of Ta-doped Si Clusters, Wires, and Bulk Systems*”, Phys. Rev. B **83**, 075434 (2011), DOI: [10.1103/PhysRevB.83.075434](https://doi.org/10.1103/PhysRevB.83.075434), (cit. on p. 62).
- [174] M. Menon, A. N. Andriotis, G. Froudakis, “*Structure and Stability of Ni-Encapsulated Si Nanotube*”, Nano Lett. **2**, 301 (2002), DOI: [10.1021/nl015695w](https://doi.org/10.1021/nl015695w), (cit. on p. 62).
- [175] A. K. Singh, V. Kumar, T. M. Briere, Y. Kawazoe, “*Cluster Assembled Metal Encapsulated Thin Nanotubes of Silicon*”, Nano Lett. **2**, 1243 (2002), DOI: [10.1021/nl025789l](https://doi.org/10.1021/nl025789l), (cit. on p. 62).
- [176] A. N. Andriotis, G. Mpourmpakis, G. E. Froudakis, M. Menon, “*Stabilization of Si-based Cage Clusters and Nanotubes by Encapsulation of Transition Metal Atoms*”, New J. Phys. **4**, 78 (2002), DOI: [10.1088/1367-2630/4/1/378](https://doi.org/10.1088/1367-2630/4/1/378), (cit. on p. 62).
- [177] Z. Ge, J. C. Duchamp, T. Cai, H. W. Gibson, H. C. Dorn, “*Purification of Endohedral Trimetallic Nitride Fullerenes in a Single, Facile Step*”, J. Am. Chem. Soc. **127**, 16292 (2005), DOI: [10.1021/ja055089t](https://doi.org/10.1021/ja055089t), (cit. on p. 62).
- [178] M. Yamada, T. Nakahodo, T. Wakahara, T. Tsuchiya, Y. Maeda, T. Akasaka, M. Kako, K. Yoza, E. Horn, N. Mizorogi, K. Kobayashi, S. Nagase, “*Positional Control of Encapsulated Atoms Inside a Fullerene Cage by Exohedral Addition*”, J. Am. Chem. Soc. **127**, 14570 (2005), DOI: [10.1021/ja054346r](https://doi.org/10.1021/ja054346r), (cit. on p. 62).
- [179] K. Kurotobi, Y. Murata, “*A Single Molecule of Water Encapsulated in Fullerene C<sub>60</sub>*”, Science **333**, 613 (2011), DOI: [10.1126/science.1206376](https://doi.org/10.1126/science.1206376), (cit. on p. 62).
- [180] D. S. Sabirov, “*From Endohedral Complexes to Endohedral Fullerene Covalent Derivatives: A Density Functional Theory Prognosis of Chemical Transformation of Water Endofullerene H<sub>2</sub>O@C<sub>60</sub> upon Its Compression*”, J. Phys. Chem. C **117**, 1178 (2013), DOI: [10.1021/jp310673j](https://doi.org/10.1021/jp310673j), (cit. on p. 62).
- [181] W. Ji, C. Luo, “*Structures, Magnetic Properties, and Electronic Counting Rule of Metals-Encapsulated Cage-like M<sub>2</sub>Si<sub>18</sub> (M = Ti-Zn) clusters*”, Int. J. Quantum Chem. **112**, 2525 (2012), DOI: [10.1002/qua.23245](https://doi.org/10.1002/qua.23245), (cit. on p. 62, 63).
- [182] J. T. Lau, K. Hirsch, A. Langenberg, J. Probst, R. Richter, J. Rittmann, M. Vogel, V. Zamudio-Bayer, T. Möller, B. von Issendorff, “*Localized High Spin States in Transition-Metal Dimers: X-ray Absorption Spectroscopy Study*”, Phys. Rev. B **79**, 241102 (2009), DOI: [10.1103/PhysRevB.79.241102](https://doi.org/10.1103/PhysRevB.79.241102), (cit. on p. 63, 66, 67).
- [183] F. Hagelberg, C. Xiao, and W. A. Lester, Jr., “*Cagelike Si<sub>12</sub> Clusters with Endohedral Cu, Mo, and W Metal Atom Impurities*”, Phys. Rev. B **67**, 035426 (2003), DOI: [10.1103/PhysRevB.67.035426](https://doi.org/10.1103/PhysRevB.67.035426), (cit. on p. 63).
- [184] H. Kawamura, V. Kumar, Y. Kawazoe, “*Growth, Magic Behavior, and Electronic and Vibrational Properties of Cr-doped Si Clusters*”, Phys. Rev. B **70**, 245433 (2004), DOI: [10.1103/PhysRevB.70.245433](https://doi.org/10.1103/PhysRevB.70.245433), (cit. on p. 63).

- [185] C.-X. Su, D. A. Hales, P. B. Armentrout, “*The Bond Energies of  $Cr_2$  and  $Cr_2^+$* ”, Chem. Phys. Lett. **201**, 199 (1993), DOI: [10.1016/0009-2614\(93\)85056-T](https://doi.org/10.1016/0009-2614(93)85056-T), (cit. on p. 66).
- [186] M. F. Jarrold, A. J. Illies, M. T. Bowers, “*Photodissociation of the Dimanganese Ion:  $Mn_2^+$ : a Route to the Energetics of Metal Clusters*”, J. Am. Chem. Soc. **107**, 7339 (1985), DOI: [10.1021/ja00311a021](https://doi.org/10.1021/ja00311a021), (cit. on p. 66).
- [187] V. E. Bondybey, J. H. English, “*Electronic Structure and Vibrational Frequency of  $Cr_2$* ”, Chem. Phys. Lett. **94**, 443 (1983), DOI: [10.1016/0009-2614\(83\)85029-5](https://doi.org/10.1016/0009-2614(83)85029-5), (cit. on p. 67).
- [188] B. Simard, M.-A. Lebeault-Dorget, A. Marijnissen, J. J. ter Meulen, “*Photoionization Spectroscopy of Dichromium and Dimolybdenum: Ionization Potentials and Bond Energies*”, J. Chem. Phys. **108**, 9668 (1998), DOI: [10.1063/1.476442](https://doi.org/10.1063/1.476442), (cit. on p. 67).
- [189] M. Cheeseman, R. J. Van Zee, H. L. Flanagan, W. Weltner, “*Transition-Metal Diatomics:  $Mn_2$ ,  $Mn_2^+$ ,  $CrMn$* ”, J. Chem. Phys. **92**, 1553 (1990), DOI: [10.1063/1.458086](https://doi.org/10.1063/1.458086), (cit. on p. 67).
- [190] W. Harbich, “*Collision of Clusters with Surfaces: Deposition, Surface Modification and Scattering*”. In *Metal Clusters at Surfaces*, ed. by K.-H. Meiwes-Broer, pp. 107-145, Springer, Berlin, 2000, ISBN: 3-540-66562-5, (cit. on p. 78).
- [191] E. Kampshoff, N. Wälchli, K. Kern, “*Silicide Formation at Palladium Surfaces. Part I: Crystalline and Amorphous Silicide Growth at the Pd(110) Surface*”, Surf. Sci. **406**, 103 (1998), DOI: [10.1016/S0039-6028\(98\)00104-6](https://doi.org/10.1016/S0039-6028(98)00104-6), (cit. on p. 78).
- [192] E. Kampshoff, N. Wälchli, K. Kern, “*Silicide Formation at Palladium Surfaces. Part II: Amorphous Silicide Growth at the Pd(100) Surface*”, Surf. Sci. **406**, 117 (1998), DOI: [10.1016/S0039-6028\(98\)00100-9](https://doi.org/10.1016/S0039-6028(98)00100-9), (cit. on p. 78).
- [193] Y. L. Wang, A. A. Saranin, A. V. Zotov, M. Y. Lai, H. H. Chang, “*Random and Ordered Arrays of Surface Magic Clusters*”, Int. Rev. Phys. Chem. **27**, 317 (2008), DOI: [10.1080/01442350801943708](https://doi.org/10.1080/01442350801943708), (cit. on p. 78).
- [194] J. Dąbrowski, H.-J. Müssig “*Silicon Surfaces and Formation of Interfaces: Basic Science in the Industrial World*”, World Scientific, Singapore, 2000, ISBN: 9-810-23286-1, (cit. on p. 78).
- [195] R. A. Wolkow, “*Controlled Molecular Adsorption on Silicon: Laying a Foundation for Molecular Devices*”, Annu. Rev. Phys. Chem. **50**, 413 (1999), DOI: [10.1146/annurev.physchem.50.1.413](https://doi.org/10.1146/annurev.physchem.50.1.413), (cit. on p. 78).
- [196] J. H. Wu, F. Hagelberg, K. Sattler, “*First-Principles Calculations of Small Silicon Clusters Adsorbed on a Graphite Surface*”, Phys. Rev. B **72**, 085441 (2005), DOI: [10.1103/PhysRevB.72.085441](https://doi.org/10.1103/PhysRevB.72.085441), (cit. on p. 78).
- [197] R. E. Schlier, H. E. Farnsworth, “*Structure and Adsorption Characteristics of Clean Surfaces of Germanium and Silicon*”, J. Chem. Phys. **30**, 917 (1959), DOI: [10.1063/1.1730126](https://doi.org/10.1063/1.1730126), (cit. on p. 78).

## References

- [198] L. Vitali, M. G. Ramsey, F. P. Netzer, “*Nanodot Formation on the Si(111)-(7 × 7) Surface by Adatom Trapping*”, Phys. Rev. Lett. **83**, 316 (1999), DOI: [10.1103/PhysRevLett.83.316](https://doi.org/10.1103/PhysRevLett.83.316), (cit. on p. 78).
- [199] J.-F. Jia, X. Liu, J.-Z. Wang, J.-L. Li, X. S. Wang, Q.-K. Xue, Z.-Q. Li, Z. Zhang, S. B. Zhang, “*Fabrication and Structural Analysis of Al, Ga, and In Nanocluster Crystals*”, Phys. Rev. B **66**, 165412 (2002), DOI: [10.1103/PhysRevB.66.165412](https://doi.org/10.1103/PhysRevB.66.165412), (cit. on p. 78).
- [200] Y.-P. Chiu, C.-M. Wei, C.-S. Chang, “*Density Functional Study of Surface-Supported Planar Magic Ag Nanoclusters*”, Phys. Rev. B **78**, 115402 (2008), DOI: [10.1103/PhysRevB.78.115402](https://doi.org/10.1103/PhysRevB.78.115402), (cit. on p. 78).
- [201] J.-Z. Wang, J.-F. Jia, Z.-H. Xiong, Q.-K. Xue, “*Spontaneous Formation of Mn Nanocluster Arrays on a Si(111)-7 × 7 Surface Observed with STM*”, Phys. Rev. B **78**, 045424 (2008), DOI: [10.1103/PhysRevB.78.045424](https://doi.org/10.1103/PhysRevB.78.045424), (cit. on p. 78).
- [202] S. Appelfeller, M. Franz, M. Dähne, “*Antimony Induced Cluster Formation on the Si(111)7 × 7 Surface*”, Surf. Sci. **608**, 109 (2013), DOI: [10.1016/j.susc.2012.09.021](https://doi.org/10.1016/j.susc.2012.09.021), (cit. on p. 78, 81).
- [203] C. Bai, “*Scanning Tunneling Microscopy and Its Applications*”, Springer, Berlin, 2000, ISBN: [3-540-65715-0](https://www.isbn-international.org/product/3-540-65715-0), (cit. on p. 78).
- [204] S. D. Solares, S. Dasgupta, P. A. Schultz, Y.-H. Kim, C. B. Musgrave, W. A. Goddard III, “*Density Functional Theory Study of the Geometry, Energetics, and Reconstruction Process of Si(111) Surface*”, Langmuir **21**, 12404 (2005), DOI: [10.1021/la052029s](https://doi.org/10.1021/la052029s), (cit. on p. 78).
- [205] K. Takayanagi, Y. Tanishiro, S. Takahashi, M. Takahashi, “*Structure Analysis of Si(111)-7 × 7 Reconstructed Surface by Transmission Electron Diffraction*”, Surf. Sci. **164**, 367 (1985), DOI: [10.1016/0039-6028\(85\)90753-8](https://doi.org/10.1016/0039-6028(85)90753-8), (cit. on p. 78, 79).
- [206] S. Y. Tong, H. Huang, C. M. Wei, W. E. Packard, F. K. Men, G. Glander, M. B. Webb, “*Low-Energy Electron Diffraction Analysis of the Si(111)7 × 7 Structure*”, J. Vac. Sci. Technol. A **6**, 615 (1988), DOI: [10.1116/1.575179](https://doi.org/10.1116/1.575179), (cit. on p. 78, 79).
- [207] K. D. Brommer, M. Needels, B. Larson, J. D. Joannopoulos, “*Ab initio Theory of the Si(111)-(7 × 7) Surface Reconstruction: A Challenge for Massively Parallel Computation*”, Phys. Rev. Lett. **68**, 1355 (1992), DOI: [10.1103/PhysRevLett.68.1355](https://doi.org/10.1103/PhysRevLett.68.1355), (cit. on p. 78).
- [208] G. Binnig, H. Rohrer, C. Gerber, E. Weibel, “*Surface Studies by Scanning Tunneling Microscopy*”, Phys. Rev. Lett. **49**, 57 (1982), DOI: [10.1103/PhysRevLett.49.57](https://doi.org/10.1103/PhysRevLett.49.57), (cit. on p. 79).
- [209] P. Avouris, “*Atom-Resolved Surface Chemistry Using the Scanning Tunneling Microscope*”, J. Phys. Chem. **94**, 2246 (1990), DOI: [10.1021/j100369a011](https://doi.org/10.1021/j100369a011), (cit. on p. 79).
- [210] J. C. Rivière, S. Myhra (eds.), “*Handbook of Surface and Interface Analysis*”, Marcel Dekker, New York, 1998, ISBN: [0-585-11013-1](https://www.isbn-international.org/product/0-585-11013-1), (cit. on p. 79).

- [211] J. Tersoff, D. R. Hamann, “*Theory of the Scanning Tunneling Microscope*”, Phys. Rev. B **31**, 805 (1985), DOI: [10.1103/PhysRevB.31.805](https://doi.org/10.1103/PhysRevB.31.805), (cit. on p. 80).
- [212] Ó. Paz, J. M. Soler, “*Efficient and Reliable Method for the Simulation of Scanning Tunneling Images and Spectra with Local Basis Sets*”, Phys. Stat. Sol. (b) **243**, 1080 (2006), DOI: [10.1002/pssb.200541453](https://doi.org/10.1002/pssb.200541453), (cit. on p. 80).
- [213] M. A. K. Zilani, Y. Y. Sun, H. Xu, Lei Liu, Y. P. Feng, X.-S. Wang, A. T. S. Wee, “*Reactive Co Magic Cluster Formation on Si(111)-(7 × 7)*”, Phys. Rev. B **72**, 193402 (2005), DOI: [10.1103/PhysRevB.72.193402](https://doi.org/10.1103/PhysRevB.72.193402), (cit. on p. 80).
- [214] M. Scheffler, “*Thermodynamic Aspects of Bulk and Surface Defects – First-Principles Calculations*”. In *Physics of Solid Surfaces*, ed. by J. Koukal, pp. [115–122](#), Elsevier, Amsterdam, 1988, ISBN: [0-444-42972-7](#), (cit. on p. 88).
- [215] R. M. Martin, “*Electronic Structure. Basic Theory and Practical Methods*”. Cambridge University Press, Cambridge, 2004, ISBN: [0-521-78285-6](#), (cit. on p. 88).
- [216] A. A. Baski, S. C. Erwin, L. J. Whitman, “*The Structure of Silicon Surfaces from (001) to (111)*”, Surf. Sci. **392**, 69 (1997), DOI: [10.1016/S0039-6028\(97\)00499-8](https://doi.org/10.1016/S0039-6028(97)00499-8), (cit. on p. 84).
- [217] K. Reuter, M. Scheffler, “*Composition, Structure, and Stability of RuO<sub>2</sub>(110) as a Function of Oxygen Pressure*”, Phys. Rev. B **65**, 035406 (2001), DOI: [10.1103/PhysRevB.65.035406](https://doi.org/10.1103/PhysRevB.65.035406), (cit. on p. 88).
- [218] K. Reuter, M. Scheffler, “*Composition and Structure of the RuO<sub>2</sub>(110) surface in an O<sub>2</sub> and CO Environment: Implications for the Catalytic Formation of CO<sub>2</sub>*”, Phys. Rev. B **68**, 045407 (2003), DOI: [10.1103/PhysRevB.68.045407](https://doi.org/10.1103/PhysRevB.68.045407), (cit. on p. 88).
- [219] J. Rogal, K. Reuter, M. Scheffler, “*CO Oxidation at Pd(100): A First-Principles Constrained Thermodynamics Study*”, Phys. Rev. B **75**, 205433 (2007), DOI: [10.1103/PhysRevB.75.205433](https://doi.org/10.1103/PhysRevB.75.205433), (cit. on p. 88).
- [220] E. C. Beret, L. M. Ghiringhelli, M. Scheffler, “*Free Gold Clusters: Beyond the Static, Monostructure Description*”, Faraday Discuss. **152**, 153 (2011), DOI: [10.1039/C1FD00027F](https://doi.org/10.1039/C1FD00027F), (cit. on p. 88).
- [221] S. Bhattacharya, S. V. Levchenko, L. M. Ghiringhelli, M. Scheffler, “*Stability and Metastability of Clusters in a Reactive Atmosphere: Theoretical Evidence for Unexpected Stoichiometries of Mg<sub>M</sub>O<sub>x</sub>*”, Phys. Rev. Lett. **111**, 135501 (2013), DOI: [10.1103/PhysRevLett.111.135501](https://doi.org/10.1103/PhysRevLett.111.135501), (cit. on p. 88).
- [222] W. Bouwen, P. Thoen, F. Vanhoutte, S. Bouckaert, F. Despa, H. Weidele, R. E. Silverans, P. Lievens, “*Production of Bimetallic Clusters by a Dual-Target Dual-Laser Vaporization Source*”, Rev. Sci. Instr. **71**, 54 (2000), DOI: [10.1063/1.1150159](https://doi.org/10.1063/1.1150159), (cit. on p. 89).
- [223] D. Nied, R. Köppe, W. Klopper, H. Schnöckel, F. Breher, “*Synthesis of a Pentasilapropellane. Exploring the Nature of a Stretched Silicon-Silicon Bond in a Nonclassical Molecule*”, J. Am. Chem. Soc. **132**, 10264 (2010), DOI: [10.1021/ja104810u](https://doi.org/10.1021/ja104810u), (cit. on p. 94).

## References

- [224] S. Ishida, K. Otsuka, Y. Toma, S. Kyushin, “*An Organosilicon Cluster with an Octasilacuneane Core: A Missing Silicon Cage Motif*”, *Angew. Chem. Int. Ed.* **52**, 2507 (2013), DOI: [10.1002/anie.201208506](https://doi.org/10.1002/anie.201208506), (cit. on p. 94).
- [225] J. Tomasi, B. Mennucci, R. Cammi, “*Quantum Mechanical Continuum Solvation Models*”, *Chem. Rev.* **105**, 2999 (2005), DOI: [10.1021/cr9904009](https://doi.org/10.1021/cr9904009), (cit. on p. 94).
- [226] S. Miertuš, E. Scrocco, J. Tomasi, “*Electrostatic Interaction of a Solute with a Continuum. A Direct Utilization of ab initio Molecular Potentials for the Prevision of Solvent Effects*”, *Chem. Phys.* **55**, 117 (1981), DOI: [10.1016/0301-0104\(81\)85090-2](https://doi.org/10.1016/0301-0104(81)85090-2), (cit. on p. 94).
- [227] J. B. Foresman, T. A. Keith, K. B. Wiberg, J. Snoonian, M. J. Frisch, “*Solvent Effects 5. The Influence of Cavity Shape, Truncation of Electrostatics, and Electron Correlation on ab initio Reaction Field Calculations*”, *J. Phys. Chem.* **100**, 16098 (1996), DOI: [10.1021/jp960488j](https://doi.org/10.1021/jp960488j), (cit. on p. 94).
- [228] A. K. Rappe, C. J. Casewit, K. S. Colwell, W. A. Goddard III, W. M. Skiff, “*Universal Force Field, a Full Periodic Table Force Field for Molecular Mechanics and Molecular Dynamics Simulations*”, *J. Am. Chem. Soc.* **114**, 10024 (1992), DOI: [10.1021/ja00051a040](https://doi.org/10.1021/ja00051a040), (cit. on p. 95).
- [229] Y. Duan, C. Wu, S. Chowdhury, M. C. Lee, G. Xiong, W. Zhang, R. Yang, P. Cieplak, R. Luo, T. Lee, J. Caldwell, J. Wang, P. Kollman, “*A Point-Charge Force Field for Molecular Mechanics Simulations of Proteins Based on Condensed-Phase Quantum Mechanical Calculations*”, *J. Comp. Chem.* **24**, 1999 (2003), DOI: [10.1002/jcc.10349](https://doi.org/10.1002/jcc.10349), (cit. on p. 95).



## Publications<sup>5</sup>

Publications that are directly related to this thesis:

8. D. Palagin, T. Teufl, and K. Reuter, “*Multi-Doping of Si Cages: High Spin States Beyond the Single-Atom Dopant Septet Limit*”, J. Phys. Chem. C **117**, 16182 (2013), DOI: [10.1021/jp4057863](https://doi.org/10.1021/jp4057863).
7. D. Palagin, and K. Reuter, “*MSi<sub>20</sub>H<sub>20</sub> Aggregates: From Simple Building Blocks to Highly Magnetic Functionalized Materials*”, ACS Nano **7**, 1763 (2013), DOI: [10.1021/nm3058888](https://doi.org/10.1021/nm3058888).
6. D. Palagin, and K. Reuter, “*Evaluation of Endohedral Doping of Hydrogenated Si Fullerenes as a Route to Magnetic Si Building Blocks*”, Phys. Rev. B **86**, 045416 (2012), DOI: [10.1103/PhysRevB.86.045416](https://doi.org/10.1103/PhysRevB.86.045416).
5. D. Palagin, M. Gramzow, and K. Reuter, “*On the Stability of “Non-Magic” Endohedrally Doped Si Clusters: A First-Principles Sampling Study of MSi<sub>16</sub><sup>+</sup> (M = Ti, V, Cr)*”, J. Chem. Phys. **134**, 244705 (2011), DOI: [10.1063/1.3604565](https://doi.org/10.1063/1.3604565).

Other publications:

4. V. E. Matulis, D. Palagin, A. S. Mazheika, and O. A. Ivashkevich, “*Theoretical Study of NO Adsorption on Neutral, Anionic and Cationic Ag<sub>8</sub> Clusters*”, Comp. Theor. Chem. **963**, 422 (2011), DOI: [10.1016/j.comptc.2010.11.008](https://doi.org/10.1016/j.comptc.2010.11.008).
3. S. Rath, S. Nozaki, D. Palagin, V. Matulis, O. Ivashkevich, and S. Maki, “*Aqueous-Based Synthesis of Atomic Gold Clusters: Geometry and Optical Properties*”, Appl. Phys. Lett. **97**, 053103 (2010), DOI: [10.1063/1.3467261](https://doi.org/10.1063/1.3467261).
2. V. E. Matulis, D. Palagin, and O. A. Ivashkevich, “*Theoretical Investigation of Gold Clusters Optical Properties*”, Russ. J. Gen. Chem. **80**, 1078 (2010), DOI: [10.1134/S1070363210060071](https://doi.org/10.1134/S1070363210060071).
1. V. E. Matulis, D. Palagin, A. S. Mazheika, and O. A. Ivashkevich, “*DFT Study of Electronic Structure and Geometry of Anionic Copper Clusters Cu<sub>n</sub><sup>-</sup> (n = 11, 12, 13)*”, J. Mol. Struct. (Theochem) **857**, 66 (2008), DOI: [10.1016/j.theochem.2008.02.005](https://doi.org/10.1016/j.theochem.2008.02.005).

---

<sup>5</sup>For the full up-to-date publication list please refer to my [Google Scholar](#) profile.

## Acknowledgements

This research work has been carried out at the chair of [Theoretical Chemistry](#) of the [Technical University Munich](#) under the supervision of [Prof. Dr. Karsten Reuter](#). I would like to thank my supervisor for constant support and guidance, inspiration, and inexhaustible supply of ideas, without which this thesis would have been impossible.

[Prof. Dr. Ulrich Heiz](#) and [Prof. Dr. Mathias Nest](#) I am very grateful for taking their time to act as second referee and examination chairman, respectively, and thus helping me through the graduation process.

[Dr. Tobias Lau](#) and [Dr. André Fielicke](#) I would like to thank for their stimulating and very impressive experimental research on gas-phase silicon clusters, as well as numerous insightful discussions in Berlin, Leuven and Davos. And, of course, visiting [BESSY II](#) synchrotron facility was a truly unforgettable experience.

Martin Franz, Stephan Appelfeller and [Prof. Mario Dähne](#) I would like to thank for a fruitful collaboration and a warm reception in Berlin. Playing around with an actual experimental STM setup was a great fun.

I would also like to thank all my colleagues within the [FOR1282](#) research unit for being excellent scientists and making me feel not alone within scientific community.

My predecessors in the project Ralf Gehrke and Matthias Gramzow I would like to thank for their help at the beginning of my work.

[Dr. Saskia Stegmaier](#) I would like to thank for fruitful discussions concerning clusters and clathrate structures.

I would also like to thank all members of our large theoretical group (three theoretical groups, in fact, led by [Prof. Domcke](#), [Prof. Reuter](#), and [Prof. Nest](#), respectively) in Garching for creating an extremely friendly environment for both working and having fun, and for making me feel at home every day during the last three years.

A very big and special thank goes to my family for their constant support and encouragement, and infinite patience.

Last, but not least, funding within the DFG Research Unit FOR1282 and support of the TUM Faculty Graduate Center Chemistry is gratefully acknowledged.